

DYNAMICS, FORMATION AND STATISTICS OF EXOPLANETARY SYSTEMS

by

Ari Silburt

A thesis submitted in conformity with the requirements  
for the degree of Doctor of Philosophy  
Graduate Department of Astronomy & Astrophysics  
University of Toronto

Copyright © 2017 by Ari Silburt

# **Abstract**

Dynamics, Formation and Statistics of Exoplanetary Systems

Ari Silburt

Doctor of Philosophy

Graduate Department of Astronomy & Astrophysics

University of Toronto

2017

MY ABSTRACT GOES HERE.

“At the end of the day people won’t remember what you said or did, they will remember how you made them feel.”

*-Maya Angelou*

# Acknowledgements

My Acknowledgements go here.

# Contents

<b>1</b>	<b>Introduction</b>	<b>1</b>
1.1	Exoplanet Observations . . . . .	1
1.1.1	Detection Methods . . . . .	1
1.1.2	Statistics of Kepler Planets . . . . .	3
1.2	Planet Formation . . . . .	5
1.2.1	Minimum Mass Solar Nebula and Snowline . . . . .	5
1.2.2	Planetesimal Formation . . . . .	6
1.2.3	Formation of Protoplanets . . . . .	7
1.3	Planetary Dynamics . . . . .	8
1.3.1	Mean Motion Resonance . . . . .	8
1.3.2	Migration . . . . .	11
1.3.3	Stability . . . . .	13
1.4	Numerical Integration . . . . .	15
1.4.1	Hamiltonian Dynamics . . . . .	15
1.4.2	Coordinate Systems . . . . .	16
1.4.3	Integrator Types . . . . .	19
1.5	This Work . . . . .	20

<b>2</b>	<b>Statistical Reconstruction of Kepler Planets</b>	<b>22</b>
2.1	Chapter Overview . . . . .	22
2.2	Introduction . . . . .	23
2.3	Methods . . . . .	28
2.3.1	Catalogs of Stars and Planets . . . . .	28
2.3.2	Simulated Planet Detections . . . . .	29
2.3.3	Uncertainties in Planet Radii . . . . .	32
2.3.4	Monte Carlo Markov Chain . . . . .	34
2.3.5	Iterative Simulation (IS) . . . . .	35
2.3.6	Calculation of Occurrence . . . . .	36
2.4	The Primordial Population of Kepler Planets . . . . .	38
2.4.1	Completeness . . . . .	38
2.4.2	Period Distribution . . . . .	40
2.4.3	Radius Distribution . . . . .	41
2.4.4	Total Occurrence of Small Planets . . . . .	44
2.5	Comparison with PHM13 . . . . .	46
2.6	Discussion . . . . .	51
2.6.1	Sensitivities and Systematics . . . . .	51
2.6.2	Astrophysical and Astrobiological Implications . . . . .	53
2.6.3	Improvements in Occurrence will Happen . . . . .	55
2.7	Conclusions . . . . .	56
2.8	Summary . . . . .	57
<b>3</b>	<b>Tides Alone Cannot Explain Kepler Planets Close to 2:1 MMR</b>	<b>58</b>
3.1	Chapter Overview . . . . .	58
3.2	Introduction . . . . .	59
3.3	Methods . . . . .	61
3.3.1	Theory . . . . .	61

3.3.2	Experimental Setup . . . . .	63
3.4	Results . . . . .	65
3.4.1	Theory vs. Numerics . . . . .	65
3.4.2	Resonant Tugging . . . . .	66
3.4.3	Minimum Eccentricity to Explain $\Delta_{obs}$ . . . . .	69
3.5	Discussion . . . . .	71
3.6	Conclusion . . . . .	74
3.7	Summary . . . . .	75
<b>4</b>	<b>HERMES: A hybrid integrator</b>	<b>76</b>
4.1	Chapter Overview . . . . .	76
4.2	Introduction . . . . .	77
4.3	Methods . . . . .	80
4.3.1	Particle Classification . . . . .	80
4.3.2	Heliocentric version of WHFAST . . . . .	80
4.3.3	Algorithm . . . . .	81
4.3.4	Perturbative Forces in the Mini Simulation . . . . .	84
4.3.5	Adaptive $f_H$ Algorithm . . . . .	85
4.4	Error . . . . .	87
4.5	Examples . . . . .	94
4.5.1	Massive Outer Solar System . . . . .	95
4.5.2	Migration of a Planet in Planetesimal Disk (Kirsh et al. 2009) . . . . .	95
4.5.3	Comparison to Mercury and SyMBA– Long Simulations . . . . .	96
4.6	Conclusion . . . . .	99
4.7	Summary . . . . .	100

<b>5</b>	<b>Stability of Planetary Systems</b>	<b>101</b>
5.1	Chapter Overview . . . . .	101
5.2	Introduction . . . . .	102
5.3	Methods . . . . .	104
5.3.1	Dataset . . . . .	104
5.3.2	Metrics . . . . .	105
5.3.3	Algorithm Training . . . . .	106
5.4	Results . . . . .	107
5.4.1	Model 1: Learning from Initial conditions . . . . .	107
5.4.2	Model 2: Generating Features from Short Integrations . . . . .	110
5.5	Discussion & Conclusion . . . . .	111
5.6	Summary . . . . .	116
<b>6</b>	<b>Analysis of HD155358</b>	<b>119</b>
6.1	Chapter Overview . . . . .	119
6.2	Introduction . . . . .	120
6.3	Best-Fit Parameters and Resonance Analysis . . . . .	122
6.3.1	Methods . . . . .	122
6.3.2	Best Fit Parameters . . . . .	123
6.3.3	Resonance Analysis . . . . .	126
6.4	Formation . . . . .	127
6.4.1	Methods . . . . .	127
6.4.2	Model Comparison . . . . .	129
6.4.3	Results . . . . .	132
6.5	Stability . . . . .	133
6.6	Discussion and Conclusion . . . . .	135
6.7	Summary . . . . .	136



<b>7</b>	<b>Conclusions &amp; Future Work</b>	<b>137</b>
7.1	Conclusions . . . . .	137
7.2	Future Work and Directions . . . . .	137
	<b>Bibliography</b>	<b>138</b>

# List of Tables

2.1	Planet Occurrence for $20 < P < 200$ days, $1 < R_p < 4R_{\oplus}$ . . . . .	45
5.1	Hyperparameters used for the initial-conditions (IC) model (Sec. 5.4.1) and short-integrations (SI) model (Sec. 5.4.2), and their associated performance. . . . .	117
5.2	‘Short-Integration’ Model Feature Importances. See text for a description of the gain and of the features. . . . .	118
6.1	Best-fit model parameters from our MCMC samples. Our PPI model includes planet-planet interactions, while our noPPI model excludes planet-planet interactions. The derived parameters from R2012 are also listed for ease of comparison. . . . .	125
6.2	The percent of randomly drawn samples with $\phi_1$ and $\phi_2$ librating, for our PPI and noPPI models. Error bars calculated from simple Poisson statistics. . . . .	127

# List of Figures

- 1.1 Cumulative distribution of period ratios of neighbouring planets in all known multi-planet systems. First and second-order mean motion resonances are displayed as dotted lines, and labelled at the top of the figure. Data from NASA Exoplanet Archive (2017). . . . . 10
- 2.1 A test case demonstrating the recovery of a known, artificial radius distribution (dashed line) using the method of iterative simulation. The dotted line represents the simulated observations, which consist of 364 detections, and the solid line is the reconstructed distribution (here binned for display). Error bars are determined from 25 bootstrapped simulations. . . . . 37
- 2.2 Completeness values for *Kepler* planet detection around stars in the Solar76k catalog. The numbers within each grid cell indicate the completeness percentage, and each grid has been colour coded from low (blue) to high (white) completeness. . . . . 39

2.3 Period distribution of *Kepler* small planets. The observed distribution (solid line) includes planets inward of 20 days (i.e. the 1052KOI sample), while the simulated distribution from the MCMC best fit ( $\alpha = -0.04$ , see Eq.2.2) is plotted as a dashed-dotted curve. This best fit is obtained for planets in the  $20 < P < 200$  day range, but is extended here to shorter periods to demonstrate that the observed population deviates significantly from a single power-law shortward of 20 days. The scale in the vertical axis is arbitrarily chosen. Slight horizontal offsets have been applied to each curve for clarity. . . . . 40

2.4 Size distribution of planets between  $1$  and  $4R_{\oplus}$ , obtained using the MCMC (solid black line) and the IS (dotted red line) techniques. Both show that planet occurrence peaks in the bin  $2 - 2.8R_{\oplus}$ . Earth-sized planets are less common, by a factor of  $\sim 2$ , although the statistical significance of this result is still low. If we assume that the currently determined planet radii carry no uncertainty, or that all stars (and hence planets) have 25% larger radii than their cataloged values, we obtain rather different radius distributions. The error bars for the “No Error” case account for poisson error only, while for the IS and 25% Larger cases, error bars are calculated from 50 bootstrapped simulations of the data (see §2.3.3). The MCMC error bars are calculated in the standard manner. Planet occurrence at each logarithmic radius bin is obtained by summing over all period bins. Slight horizontal offsets have been applied to each curve for clarity. . . . . 42

2.5	Our IS distribution displayed for a smaller logarithmic bin size. This finer resolution reveals more information about the intrinsic distribution, and specifically we see a potential rise in the number of $1-1.15R_{\oplus}$ planets. This bin has large error however, and thus more statistics are required to confirm this conclusion. . . . .	43
2.6	Comparison of completeness values computed with our methods to those reported by PHM13 in Figure S11, expressed as a fractional difference. Our values are generated using the “Best42k” catalog from PHM13 and our detection criteria. Bins where both our completeness and those of PHM13 are zero have been blacked out. . . . .	46
2.7	A summary of our comparison to PHM13. All curves are constructed using the “603PHM” dataset and “Best42k” sample. The results of PHM13 are plotted as the dotted curve in red with squares, “This work” using Equation 2.11 is the black solid curve in black with stars, “This work, PHM13 Completeness” using PHM13’s Figure S11 completeness values and Equation 2.11 is the green dashed curve with diamonds, and “This work, PHM13 Method” using PHM13’s method of calculating occurrence (i.e. Equation 2.12) is the blue dashed-dotted curve with triangles. Slight horizontal offsets have been applied to each curve for clarity. . . . .	48

2.8	Distribution of completeness values for Earth-sized ( $R_p = 1.25R_\oplus$ , solid, black) and Neptune-sized ( $R_p = 3.75R_\oplus$ , dashed, red) planets among a collection of 20,000 stars from the Solar76k sample, calculated on a star-by-star basis. For these calculations, all planets have been assigned a period of 30 days. As is clearly seen, the completeness variation is much larger among the Earths vs. Neptunes, illustrating how one can introduce significant detection bias into the occurrence calculations of small planets if an average over all stars is not taken. . . . .	50
3.1	<i>Kepler</i> systems close to 2:1 MMR. A statistical excess is present just wide of the 2:1 MMR, and appears to decline beyond 6% of the resonance, as marked by a red dotted line. . . . .	60
3.2	Cumulative distribution function (CDF) of our results. The solid line shows $\Delta_{num} - \Delta_{th}$ , the difference between the theoretical and simulated planet separations after $T = 10$ Gyr. The dashed line shows $\Delta_{num} - \Delta_{obs}$ , the difference between our numerical simulations and the observed <i>Kepler</i> spacing. . . . .	66
3.3	Two test cases illustrating resonant tugging and repulsion. The top and bottom panel shows the period evolution of the inner and outer planet, respectively. For the black curve $e_{in,i} = 0.125$ , while for the grey curve $e_{in,i} = 0.018$ . The dotted black curve shows the numerical trajectory of the inner planet ( $e_{in,i} = 0.125$ ) in the absence of the outer planet. . . . .	68

3.4	Three CDFs showing the theoretical minimum eccentricity required by the inner planet in order to achieve the observed $\Delta$ spacing seen by <i>Kepler</i> planets today. The solid, dashed, dotted lines represent $T = 1, 5, 10$ Gyr tracks, respectively, while the dash-dotted line represents $T \rightarrow \infty$ . In all calculations we assume the outer planet remains stationary, i.e. $(a_i/a_f)_{out} = 1$ . The red shaded region marks the unphysical region where the eccentricity is larger than unity. The blue region marks the region where most systems undergo a dynamical instability. . . . .	70
4.1	A diagram illustrating how different particle types (active, semi-active, test) affect each other. Arrows indicate directions of gravitational influence. . . . .	80
4.2	A short simulation displaying the HERMES integrator for a 2 planet, 2 planetesimal system orbiting a central star. When active, the mini simulation takes many sub-timesteps for each $dt$ and integrates planets 1, 2 and planetesimal 1 during the close encounter between planet 1 and planetesimal 1. . . . .	83
4.3	Panel a. shows a regular orbit in 2D, while panel b. shows the construction of a ring by rotating the orbit's pericenter by $2\pi$ . . . . .	86
4.4	Three body problem, in the reference frame of the planet. In a. the initial setup is shown, where the planetesimal starts near the planet, inside a sphere of radius $r_H f_H$ and the entire system is integrated purely by IAS15. Here the arrow indicates the initial direction of the planetesimal. In b. the planetesimal exits the sphere with radius $r_H f_H$ and the system is integrated purely via WHFAST, introducing a numerical error of $E_{scheme}^{WH}$ . . . . .	89

4.5	Final relative energy error as a function of $f_H$ for a star-planet-planetesimal system. Blue dots are numerical simulations, the green curve is the theoretical prediction of Eq. 4.8. . . . .	91
4.6	Final energy error as a function of $dt$ for a star-planet-planetesimal system. Blue dots are numerical simulations, the green curve is the theoretical prediction of Eq. 4.8. . . . .	92
4.7	Final relative energy error as a function of the number of close encounters, for a system composed of a star, planet and 200 planetesimals. Blue dots are numerical simulations, the green line is our unbiased theoretical prediction of Eq. 4.9 with $K = 15$ , while the red line is the biased theoretical prediction. . . . .	93
4.8	Planet's semimajor axis vs. time, analogous to the numerical experiment in the lower right panel of Figure 3 from Kirsh et al. (2009). Light green lines represent individual runs, while the dark thicker green line represents the average of the individual runs. . . . .	97
4.9	A test of HERMES, Mercury and SyMBA for collections of 50Myr, 50 planetesimal runs. Top panel shows the relative energy error over time, with individual runs in lighter shades and averaged values in dark shades. Bottom panel shows the elapsed simulation times of individual runs, using the same colour scheme as the top panel. . . . .	98



5.1	Performance on the test dataset using the machine learning model trained on system's initial conditions. Stable systems are marked blue, unstable systems are marked red. Correctly classified systems are plotted as circles, incorrect predictions are marked as crosses. The bottom and left axes show Hill-sphere separations $\Delta$ for the inner and outer planet pairs, respectively. The top and right axes correspond to period ratios between the planet pairs. The dashed black line corresponds to the Lissauer-family model $\Delta_1 + \Delta_2 > 16.1$ . . . . .	109
5.2	Comparison of predictions of the initial-condition and short-integration models on the test set. Stable systems are shown in green, unstable systems are shown in blue, and the model-predicted probability of stability for each system is shown along the x-axis. The leftmost blue bin is cut off to render smaller bins visible—in the top panel it reaches 395, and in the bottom panel 640. . . . .	112
5.3	Precision-recall curves for each model in this paper, generated from all possible values of the model's threshold classification probability. The Lissauer-family models predict stability if the sum of the Hill-sphere separations is greater than a particular threshold, and the corresponding curve was generated by considering all possible threshold values. The horizontal black-dashed line is the 90% precision requirement we imposed on all models in this paper. . . . .	114
6.1	RV data and PPI model fit. Top panel shows the RV data points, MCMC MAP value (green), and 100 randomly plotted samples from the posterior (black). Bottom panel shows the residuals for the MAP fit to the RV data. . . . .	124

6.2	RV data and $\theta_{\text{mig,best}}$ fit. Top panel shows the RV data points, MCMC MAP value (green), and 100 randomly plotted samples from the posterior (black). Bottom panel shows the residuals for the MAP fit to the RV data. . . . .	130
6.3	The best 45 models $\theta_{\text{model}} = \{\tau_{a_1}, K_1, K_2\}$ with Bayes' factors less than 100 when compared against the best model in our sample of 3000 simulations. Top panel presents the data in $(K_1, K_2)$ space, and the parameters from our 3000 simulations were uniformly sampled from the region displayed. Bottom panel displays the same data in $(\tau_{e_2}, \tau_{e_2})$ space. Colour indicates the log value of $\tau_{a_1}$ . . . . .	131
6.4	Histograms of each parameter showing the distribution of 2000 stable (green) and unstable (red) systems drawn from our PPI model's posterior distribution and simulated for $10^9$ years. The black vertical dashed line in each histogram represents our MAP estimate for that parameter.	134

# Chapter 1

## Introduction

### 1.1 Exoplanet Observations

#### 1.1.1 Detection Methods

##### Radial Velocity

A periodic wobble will be observed in the lightcurve of a star with an orbiting planet due to their motion around the common centre of mass. From the conservation of energy and angular momentum this wobble, or radial velocity, of a star due to a planetary companion can be calculated according to (Beaugé et al. 2007):

$$V_r = K \cdot [\cos(v(t) + \omega) + e \cdot \cos(\omega) + \gamma] \quad (1.1)$$

where  $K$  is the semi-amplitude:

$$K = \frac{m_p \sin(i)}{m_* + m_p} \frac{2\pi a}{P\sqrt{1 - e^2}} \quad (1.2)$$

$a$  is the semi-major axis of the planet,  $P$  is the orbital period,  $m_p$  is the planet mass,  $m_*$  is the stellar mass,  $i$  is the inclination,  $e$  is the eccentricity,  $v(t)$  is the true anomaly,  $\omega$  is the argument of periastron, and  $\gamma$  is the stellar drift in velocity. Since the probability

of detecting a planet is related to  $K$ , radial velocity preferentially detects massive planets on short orbits.

In theory one can extract the orbital parameters of the planet from the radial velocity (mass, eccentricity, orbital period, etc.), however in practice it is more complicated. For example, successful extraction of orbital parameters requires accurate and precise knowledge of the stellar mass, which is typically difficult to obtain (e.g. Brown et al. 2011). Furthermore, only a lower limit  $m \sin(i)$  estimate on planet mass can be calculated unless the inclination relative to Earth's line of sight is known. In addition, the radius of the planet cannot be calculated from the radial velocity method, precluding any information about size and density.

When multiple planets orbit a star the radial velocity signal becomes more complex, though it is still quasi-periodic in nature (assuming orbital stability). Assuming that the planets are well-separated such that their mutual gravitational interactions are weak, the radial velocity of the star can be approximated as the sum of planetary Keplerian orbits:

$$V_r = \gamma + \sum_{i=1}^{n_p} K_i \cdot [\cos(\nu_i(t) + \omega_i) + e_i \cdot \cos(\omega_i)] \quad (1.3)$$

where  $n_p$  is the number of planets in the system. If however the planet-planet gravitational interactions are strong, Equation 1.3 is invalid and must be replaced with a more careful numerical treatment.

### Transit Method

When a planet passes (or transits) in front of its host star, a portion of the star's emitted flux  $F$  will be blocked. The fraction of blocked flux is proportional to the relative areas of the star and planet:

$$\frac{\Delta F}{F} \propto \left( \frac{r_p}{r_*} \right)^2 \quad (1.4)$$

where  $r_p$  and  $r_*$  are the planet and stellar radii, respectively. In addition, the probability of a transiting planet  $P_t$  is inversely proportional to its semi-major axis:

$$P_t = \frac{r_*}{a} \quad (1.5)$$

Thus, from Equations 1.4 and 1.5 we see that large, short-period planets are preferentially detected by the transit method.

The first transiting planet was detected by Henry et al. (1999) and independently by Charbonneau et al. (2000). Since then the transit method has become the most successful detection technique, with over 2,700 confirmed planets to date (NASA Exoplanet Archive 2017). Most of these discoveries have come from the *Kepler Space Telescope* (hereafter *Kepler*). For reference, the next most successful detection technique is the radial velocity method (Section 1.1.1) with over 600 confirmed planets to date (NASA Exoplanet Archive 2017).

From the transit method one can determine the period and radius of the planet. In addition, the atmospheric properties of exoplanets can also be probed (Kreidberg et al. 2014; Tsiaras et al. 2016; Stevenson et al. 2016). In total, the transit method is able to provide essential information about the composition, formation and habitability of a planet. However, the transit method is not without its limitations. For example, most orbital parameters needed for dynamical studies, like eccentricity and mass, cannot be determined for individual systems via the transit method. In addition, false positives from eclipsing binaries and background targets are a huge source of contamination (Fressin et al. 2013), and confirmation via a different method is often required. Smaller planets and/or planets belonging to multi-planet systems are much less likely to be false positives than large, single planets (Fressin et al. 2013).

### 1.1.2 Statistics of Kepler Planets

The *Kepler* mission is the most successful planet-finding mission to date, providing scientists for the first time a population of planets orbiting other stars. Due to the

selection bias of the transit method (see Section 1.1.1), most of these planets have periods of less than 50 days and are larger than Earth. However, sufficient detection across the full range of Earth-to-Jupiter sized planets has enabled scientists to calculate the occurrence of planets around other stars in our galaxy.

Two seminal works analyzing the *Kepler* population are Fressin et al. (2013) and Petigura et al. (2013). Fressin et al. (2013) found that the global false positive rate of the *Kepler* data is roughly 10%, the radius distribution peaks at mini-Neptune ( $2 < r_p/r_\oplus < 2.8$ ,  $r_\oplus$  is the radius of Earth) sized planets, and the occurrence of Neptune and Jupiter sized planets is significantly lower than the occurrence of  $r_p/r_\oplus < 2.8$  sized planets. Using a carefully vetted data sample, Petigura et al. (2013) found a similar result as Fressin et al. (2013), i.e. that the radius distribution peaks at mini-Neptune and the occurrence of Neptune and Jupiter sized planets is much lower.

A calculation of planet occurrence is usually performed by binning the planets in  $r$ – $P$  space (where  $r$  is planet radius and  $P$  is planet period), and calculating planet occurrence for each bin. The occurrence  $f(P_i, r_j)$  of planets in bin  $(i, j)$  for a population of planets is:

$$f(P_i, r_j) = \frac{1}{N_*} \sum_k^{n_p(i,j)} \left( \frac{a_k}{r_{*,k}} \frac{1}{\epsilon(i, j)} \right) \quad (1.6)$$

where  $N_*$  is the total number of stars surveyed in the sample,  $n_p(i, j)$  are the number of planets falling into bin  $(i, j)$ ,  $\frac{a_k}{r_{*,k}}$  is the geometric correction factor to account for missed non-transiting planets (inverse of Equation 1.5) and  $\epsilon(i, j)$  is the detection completeness of bin  $(i, j)$  to account for missed transiting planets due to low signal-to-noise.

Of the ingredients that go into a Equation 1.6, the most difficult quantity to accurately measure is the detection completeness. Unlike Fressin et al. (2013) who used Combined Differential Photometric Precision (CDPP) values to estimate the detection completeness of known planets, Petigura et al. (2013) instead performed an injection and recovery of simulated light curves. Although the injection and recovery technique is certainly a more accurate method for calculating detection completeness,

Fressin et al. (2013) found that CDP estimates were robust and could lead to accurate predictions.

One critical aspect of planet occurrence that Fressin et al. (2013) and Petigura et al. (2013) failed to incorporate into their calculations was the large error bars present in the *Kepler* data. The mean planetary radius error in the Batalha et al. (2013) *Kepler* dataset is 30%, meaning that, within 3 standard deviations a super-Earth sized planet could actually be Neptune or Earth-sized. These errors primarily stem from the fact that the radii of *Kepler* stars are not well known (Brown et al. 2011), also with a mean radius error of 30%. With such large error bars present in the *Kepler* data, ignoring them can affect the resulting radius and planet occurrence distributions.

## 1.2 Planet Formation

### 1.2.1 Minimum Mass Solar Nebula and Snowline

The initial conditions of the Solar System are still largely unknown. Hayashi (1981) and Weidenschilling (1977b) provided the first benchmarks for the initial mass of the Solar System by assuming a rocky core for all planets and calculating the initial surface density distribution  $\Sigma$  as a function of distance  $d$  required to produce the masses of the planets:

$$\Sigma(d) = \Sigma_0 \left( \frac{d}{1\text{AU}} \right)^{-3/2} \quad (1.7)$$

where  $\Sigma_0 = 1700\text{g/cm}^2$ . This initial surface density distribution is known as the “minimum mass solar nebula” (MMSN), and is a benchmark against which most planet formation studies are compared to.

A second critical property of circumstellar disks is the location of the snowline. In standard formation theory the snowline marks the boundary where water ice begins to form, providing the additional solid material required to make large cores and

form Jovian planets. Hayashi (1981) provided a benchmark temperature profile  $T(d)$  for the Solar System:

$$T(d) = T_0 \left( \frac{d}{1\text{AU}} \right)^{-1/2} \quad (1.8)$$

where  $T_0 = 280\text{K}$ . In this model, the distance at which the temperature drops to below freezing is  $\sim 2.7$  AU. More recent models of the snowline (Sasselov & Lecar 2000) include detailed radiative transfer physics and heating via accretion, and show that the primordial snow line in our Solar System could have been as close as 1 AU.

Until recently, scientists have lacked the tools to observationally test these theories. Telescopes like the Atacama Large Millimeter/submillimeter Array (ALMA) have begun providing observations of circumstellar disks around young stellar objects like HL Tau (ALMA Partnership et al. 2015). In total, about 80 circumstellar and debris disks have been observed to date (e.g. Schneider et al. 2014; Choquet et al. 2016), revealing unexpected features like concentric rings sculpted by large planets (Tamayo et al. 2015). *AS[This paragraph can be stronger. ]*

## 1.2.2 Planetesimal Formation

Before planets can form there must be an abundance of kilometre-sized planetesimals. There are currently two leading models for forming such kilometre-sized planetesimals – coagulation (core-accretion) and gravitational instability. In the coagulation model, pairwise collisions between sticky dust particles lead to steady growth up to meter-sized and beyond (Weidenschilling 1977a; Armitage 2010). However, mean collision velocities are strongly coupled to size and destructive collisions tend to occur for meter-sized objects (Weidenschilling 1977a; Blum & Wurm 2008), hindering planetesimal growth. In addition, meter-sized objects embedded in a protoplanetary disk will strongly couple to the gas and typically drift into the central star on a timescale of  $10^3$  years (Weidenschilling 1977a). Thus, a mechanism is required to quickly grow particles beyond a meter in size to avoid destruction. Solutions to this "meter-barrier



problem" have been proposed (e.g. Boley et al. 2014), however no clear consensus has yet emerged.

In the gravitational instability model, as the solar nebula cools, dust particles settle in the mid plane, becoming vulnerable to collapse (Goldreich & Ward 1973). These dust particles clump and eventually become gravitationally unstable, forming  $\sim 100\text{m}$  sized particles (Goldreich & Ward 1973). This process then repeats, each time forming larger and larger planetesimals via gravitational instability. This model is attractive since it bypasses the scales most vulnerable to destructive collisions (i.e. the meter-barrier problem), and can form large planetesimals in  $\sim 10^3$  years (Goldreich & Ward 1973; Armitage 2007). However, in practice it is very difficult to collect dust particles in densities high enough for gravitational instability, and especially so in turbulent disks (Armitage 2007).

The formation mechanism of planetesimals is still unclear, however, *some* mechanism must exist since planetesimals are ubiquitous.

### 1.2.3 Formation of Protoplanets

The formation of protoplanets occurs shortly after the formation of large, kilometre-sized planetesimals. In a pioneering study, Greenberg et al. (1978) found that in the early stage of planet formation larger planetesimals grow more rapidly than smaller ones, resulting in the runaway growth of the largest planetesimal. As a result, 1–10km sized planetesimals at 1AU can grow into  $10^{22} - 10^{24}$  kg protoplanets in  $10^5 - 10^6$  years (Wetherill & Stewart 1989). This runaway process stems from the fact that 1–10 km sized planetesimals are large enough to gravitationally focus each other yet are still dynamically cool via gas damping, resulting in a maximum collision cross section (Armitage 2010). Since growth time is related to orbital frequency, more distant regions will have slower runaway growth timescales.

Eventually this runaway growth transitions into a slower, "oligarchic" growth. As

protoplanets grow, surrounding planetesimals are dynamically excited via gravitational stirring, decreasing the collision cross section and slowing the rate of protoplanetary growth (Kokubo & Ida 1998). By the end of oligarchic growth protoplanets have consumed most of the surrounding material and have reached their isolation mass (Schlichting 2014). Beyond the snowline the isolation mass is roughly the mass of Neptune, however inside the snowline it is a fraction of an Earth mass (Schlichting 2014). Since numerous *Kepler* planets larger than Earth reside inside the snowline of their host star, this suggests that either i) giant impacts between protoplanets, ii) inward drift of additional material, or iii) migration must have taken place (Schlichting 2014).

## 1.3 Planetary Dynamics

### 1.3.1 Mean Motion Resonance

Mean motion resonance (MMR) occurs when the orbital period of one planet is an integer ratio of another. Like other types of resonances occurring in nature, MMR results in the amplitude growth of various quantities characterizing the system like eccentricity, semi-major axis and the longitude of pericentre (Murray & Dermott 1999). As a result, the presence of MMR can strongly affect the formation, evolution and longterm stability of planetary systems in a diversity of ways. For example, Kirkwood gaps are unstable regions in the asteroid belt carved by MMRs with Jupiter, while Pluto and Neptune are protected from going unstable due to a 3:2 MMR.

For every  $p : q$  MMR (where  $p$  and  $q$  are integers) there are two important resonant angles:

$$\begin{aligned}\phi_1 &= p\lambda_1 - q\lambda_2 + \varpi_1 \\ \phi_2 &= p\lambda_1 - q\lambda_2 + \varpi_2\end{aligned}\tag{1.9}$$

where  $\lambda$  is the mean longitude and  $\varpi$  is the longitude of periaapse. For planets in MMR the time variation of one or both resonant arguments must be zero. As a result, MMRs can be modelled in terms of a pendulum oscillating about a stable, fixed point. After some algebra it can be shown that a MMR can be modelled as (Murray & Dermott 1999):

$$\ddot{\phi} = -\omega_0^2 \sin \phi \quad (1.10)$$

where  $\omega_0$  is the amplitude of libration and is dependent upon the orbital parameters of the system (mass, eccentricity, semi-major axis).

The pendulum model facilitates an understanding about certain properties of MMR. For energies larger than a critical energy  $E_{crit}$  the pendulum will circulate over all possible values of  $\phi$ , while for energies smaller than  $E_{crit}$  the pendulum will be in MMR and librate about  $\phi = 0$ . The critical energy,  $E_{crit}$ , defines motion on the separatrix, which separates the circulation and libration regimes. In context of a pendulum, this would correspond to the pendulum suspended vertically in the air with an infinite period of libration.

The strength of a given MMR is related to its width, which in turn is related to the order of the resonance ( $= p - q$ ) and the magnitude of  $p$  and  $q$  (Murray & Dermott 1999). More fundamentally, the strength of a MMR is related to the mass, eccentricity and mean motions of the planets involved (Murray & Dermott 1999). Stronger MMRs are associated with lower values of  $p$ ,  $q$  and  $p - q$ , making the 2:1 and 3:2 MMRs the most probable resonant locations in nature. Figure 1.1 shows the distribution of period ratios for planets discovered by *Kepler*, along with the locations of first and second order MMRs. As can be seen, statistical excesses of planets exist near the 3:2 MMR and to lesser degree the 2:1 MMR (Lissauer et al. 2011; Fabrycky et al. 2014; Steffen & Hwang 2015), supporting the idea that these resonances are most capable of trapping planets.

Planets from these statistical pileups are typically a few percent away from exact

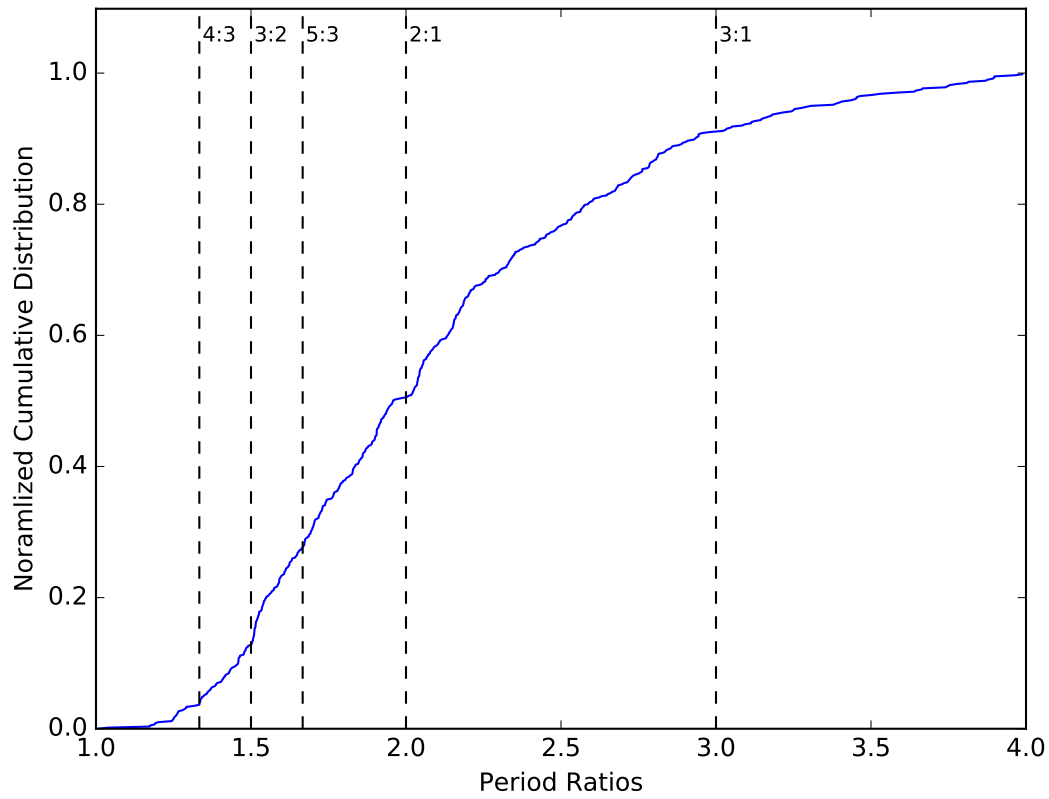


Figure 1.1: Cumulative distribution of period ratios of neighbouring planets in all known multi-planet systems. First and second-order mean motion resonances are displayed as dotted lines, and labelled at the top of the figure. Data from NASA Exoplanet Archive (2017).

period commensurability, and dissipative mechanisms have been proposed to transport these planets from exact MMR. The most popular of these mechanisms are tidal (Lithwick & Wu 2012; Batygin & Morbidelli 2013; Delisle et al. 2014), protoplanetary (Rein 2012; Baruteau et al. 2013; Goldreich & Schlichting 2014), and planetesimal (Moore et al. 2013; Chatterjee & Ford 2015). The formation implications for each mechanism are different, and no clear consensus has yet emerged.

### 1.3.2 Migration

Planetary migration is believed to be the best way to place planets in MMR (e.g. Lee & Peale 2002), making it very important for planetary formation. Presented here are the two primary ways that planets can migrate – planetesimal-driven and gas-driven migration.

#### Planetesimal-Driven Migration

Planetesimals passing through the Hill sphere of a planet will exchange angular momentum via gravity (Ida et al. 2000; Kirsh et al. 2009). If there is an asymmetry to the number of planetesimals interacting with the planet on its near and far sides, a net force will migrate the planet. However, to guarantee a net migration, planetesimal orbits must decouple from the planet. A massive enough planet (e.g. Jupiter) will directly eject and decouple planetesimals from the system, however if the planet is smaller (e.g. Neptune) planetesimals must decouple by interacting with a neighbouring planet. In addition, for sustained migration the planet must constantly encounter fresh, dynamically cold planetesimals (Gomes et al. 2004).

Since protoplanetary growth is proportional to orbital frequency (e.g. Rafikov 2003), planetesimal disks are most likely to exist in the outer reaches of planetary systems where fewer orbital cycles have occurred. In the Solar System, the primordial Kuiper belt is believed to have once been such a planetesimal disk, causing Neptune to

migrate outwards into the Kuiper belt and shepherd planetesimals inwards to Jupiter, which subsequently ejected them from the Solar System (Fernandez & Ip 1984). This idea is well supported by observations of the outer Solar System, which show that Pluto, along with a host of smaller bodies, orbit in stable 3:2 MMRs with Neptune (Malhotra 1993; 1995).

### **Gas-Driven migration**

Since the discovery of the first hot Jupiter (Mayor & Queloz 1995), gas-driven migration is believed to play an important role in shaping exoplanetary systems (Lin et al. 1996). Whenever a fully-formed planet is embedded in a protoplanetary disk, angular momentum can be exchanged via disk-planet torques (Goldreich & Tremaine 1980). The result of this exchange is planetary migration, and this scenario is believed to be common to all young planetary systems. Gas-driven migration comes in two main flavours – Type I and Type II.

Type I migration occurs when low-mass planets are fully embedded in a protoplanetary disk and do not significantly perturb the disk structure (Armitage 2010). At particular resonant locations, known as "Linblad resonances", density waves are excited due to gravitational interactions between the planet and disk (Goldreich & Tremaine 1979). These density waves exchange angular momentum with the planet, and migration occurs when the inner and outer disk interact asymmetrically with the planet (Goldreich & Tremaine 1979). In general, the direction of Type-I migration tends to be inwards towards the central star (Ward 1997).

Type II migration occurs when high-mass Jovian planets significantly modify the structure of the surrounding protoplanetary disk, opening up a gap. This gap locks the planet in place, coupling the migration of the planet to the evolution of the disk (Lin & Papaloizou 1986). The viscous evolution of the disk causes the planet to slowly migrate inwards, at speeds typically one or two orders of magnitude slower than

Type-I migration (Ward 1997).

In comparison to planetesimal migration, gas-driven migration is still not well understood. In particular, standard calculations of gas-driven migration are too quick by 1-2 orders of magnitude (Lin & Papaloizou 1986; Tanaka et al. 2002), causing planets to spiral into their central stars before the protoplanetary disk has dispersed. In contrast to this standard view, recent work (Fung & Chiang 2017) has suggested that planets actually do not migrate that much and tend to be better behaved than originally believed. A consensus on migration has yet to be established, but it is clear that some form of migration must occur in the universe due to the large number of planets in or near MMR (Lissauer et al. 2011; Fabrycky et al. 2014; Steffen & Hwang 2015).

### 1.3.3 Stability

The longterm stability of planetary orbits has been studied for hundreds of years by many famous scientists including Issac Newton, Joseph-Louis Lagrange and Carl Friederich Gauss. However, due to the chaotic and non-integrable nature of planetary systems it has been historically difficult to make progress on N-body problems. The chaos in planetary systems is caused by overlapping resonances (Chirikov 1979; Lecar et al. 2001), resulting in the divergence of near-identical systems on long timescales. However, with the aid of computers the equations of motion governing planetary systems can be brute-force integrated into the future or past, allowing scientists to answer fundamental questions that have plagued humans for hundreds of years. For example, it is now known that the Solar System is marginally stable (Sussman & Wisdom 1988; Laskar 1994; Lecar et al. 2001), with Mercury having a 1% chance of colliding with Venus or the Sun within a couple billion years (Laskar & Gastineau 2009). It is also now well established that most known multi-planet systems are packed to capacity, and adding additional planets into these systems would result in

dynamical instabilities (Fang & Margot 2013; Pu & Wu 2015).

Although most planetary systems cannot be analytically solved, constraints on these systems can still be derived from analytical means. For example, Wisdom (1980) and Duncan et al. (1989) showed that for small eccentricities in the Restricted 3-Body Problem (R3BP), chaotic orbits (leading to close encounters, collisions and ejections) will occur when the perturber and particle are separated by  $\Delta a \leq 1.3\mu_p^{2/7}a_p$  (where subscript  $p$  indicates the perturber). Also associated with the R3BP is the Jacobi constant, which can be used to constrain the chaotic motion of a particle in parameter space. For two massive planets, Gladman (1993) showed that orbits are Hill stable if  $\Delta a \geq 3.46R_H$  (where  $R_H$  is the mutual Hill radius), forbidding close encounters for all time.

Since the discovery of numerous exoplanetary systems via *Kepler*, longterm stability has become a popular way to constrain orbital parameters (Lissauer et al. 2011; Steffen et al. 2013; Jontof-Hutter et al. 2014; Tamayo et al. 2015). If one assumes that an observed system is stable over billions of years, grids of N-body integrations can be used to find stable regions of parameter space, further narrowing the range of valid solutions originally constrained by observations. Although this brute-force method is certainly useful, it is not without its costs. A 10 billion year integration of the Solar System takes weeks to complete, and due to the chaotic nature of planetary systems hundreds to thousands of realizations must be simulated to acquire statistically rigorous results.



## 1.4 Numerical Integration

### 1.4.1 Hamiltonian Dynamics

The Hamiltonian  $\mathcal{H}$  encodes the kinetic and potential energy for a system of  $N$  bodies. In its most basic form, the Hamiltonian is:

$$\mathcal{H} = \sum_{i=0}^{N-1} \frac{\mathbf{p}_i^2}{2m_i} - \sum_{i=0}^{N-1} \sum_{j=i+1}^{N-1} \frac{Gm_i m_j}{|\mathbf{r}_i - \mathbf{r}_j|} \quad (1.11)$$

where  $\mathbf{r}_i$ ,  $\mathbf{p}_i$  and  $m_i$  are the position, momentum and mass of body  $i$ , respectively. The first term in Equation 1.11 sums the kinetic energies of the system, while the second term sums the potential energies of the system.

The coordinates  $(\mathbf{r}, \mathbf{p})$  used in Hamiltonian mechanics are canonical, obeying the fundamental Poisson bracket relations:

$$\{\mathbf{r}_i, \mathbf{r}_j\} = 0, \quad \{\mathbf{p}_i, \mathbf{p}_j\} = 0, \quad \{\mathbf{r}_i, \mathbf{p}_j\} = \delta_{ij} \quad (1.12)$$

where  $\delta_{ij}$  is the Kronecker delta. A primary benefit of using the Hamiltonian framework is the ease of evolving a N-body system into the future or past via Hamilton's equations:

$$\begin{aligned} \frac{d\mathbf{p}}{dt} &= -\frac{\partial H}{\partial \mathbf{r}} \\ \frac{d\mathbf{r}}{dt} &= \frac{\partial H}{\partial \mathbf{p}} \end{aligned} \quad (1.13)$$

Numerically this is trivial to do, with the accuracy of the result being inversely proportional to the size of the timestep,  $dt$ . A second benefit is the inherent "area preserving" or symplectic nature of Hamiltonian systems, where the energy error is bound to a finite value (excluding e.g. numerical roundoff errors which grow with time).

In the context of planetary systems Equation 1.11 can be modified to make integration more efficient. For example, a planet will orbit in a Keplerian fashion around a

central star, determined exactly by the planet's orbital parameters and stellar mass. In addition, for multi-planet systems gravitational interactions between planets will occur, perturbing planets off their original Keplerian trajectories. Thus, a new Hamiltonian can be constructed consisting of a "Keplerian" term,  $\mathcal{H}_K$ , and "Interaction" term,  $\mathcal{H}_I$  according to (Wisdom & Holman 1991):

$$\mathcal{H} = \mathcal{H}_K + \mathcal{H}_I$$

If the planets are well-separated these gravitational interactions are small and the system can be numerically integrated by applying Keplerian and Interaction operators in a "leapfrog" manner:

$$E_{\mathcal{H}}(dt) = E_{\mathcal{H}_K}(dt/4) \cdot E_{\mathcal{H}_I}(dt/2) \cdot E_{\mathcal{H}_K}(dt/4) \quad (1.14)$$

where  $E_X(Y)$  represents the evolution (or integration) of the system under  $X$  for time  $Y$ . Equation 1.14 is a second order integration scheme, and is the most popular choice for simulating planetary systems.

## 1.4.2 Coordinate Systems

As mentioned above, the most efficient way to solve the N-body problem is to split the Hamiltonian into Keplerian and Interaction components. In general, the Keplerian and Interaction Hamiltonians take the following form:

$$\mathcal{H}_K = \sum_{i=1}^N \frac{\mathbf{p}_i^2}{2m_i} - \frac{Gm_0m_i}{|\mathbf{r}_i|}, \quad \mathcal{H}_I = \sum_{i=1}^N \sum_{j=1, j \neq i}^N \frac{Gm_i m_j}{|\mathbf{r}_i - \mathbf{r}_j|} \quad (1.15)$$

However, there are numerous ways to perform these splits, with each coordinate system having relative strengths and weaknesses. The most popular splittings are discussed below. In all cases  $\mathbf{r}$  and  $\mathbf{p}$  represent cartesian position and momenta, respectively,  $N$  is the total number of particles, and  $M$  is the total mass of the system.

## Jacobi

Carl Jacobi worked out a coordinate system in which the planet positions are measured relative to the centre of mass of all bodies interior to it. Since a planet's semi-major axis (and hence position) is dependent upon the mass interior to it by Kepler's 3rd law, in this coordinate system the position of a particle is directly affected by all bodies interior to it.

The Jacobi position  $\mathbf{r}'$  and momentum  $\mathbf{p}'$  are a canonical set and are related to the cartesian position and momentum according to (Murray & Dermott 1999):

$$\mathbf{r}'_i = \mathbf{r}_i - \mathbf{R}_{i-1}, \quad \mathbf{p}'_i = \frac{\eta_{i-1}}{\eta_i} \mathbf{p}_i - \frac{m_i}{\eta_i} \sum_{j=0}^{i-1} \mathbf{p}_j \quad (1.16)$$

where  $\mathbf{R}_i = \frac{1}{\eta_i} \sum_{j=0}^i m_j \mathbf{r}_j$  is the centre of mass of all particles interior to body  $i$  and  $\eta_i = \sum_{j=0}^i m_j$  is the sum of masses interior to body  $i$ . For the special case of  $i = 0$ :

$$\mathbf{r}'_0 = \mathbf{R}_N, \quad \mathbf{p}'_0 = \sum_{j=0}^N \mathbf{p}_j \quad (1.17)$$

The inverse transformations from Jacobi coordinates to cartesian coordinates can be found in Chapter 9.5 of Murray & Dermott (1999).

The benefit of Jacobi coordinates is that the kinetic terms remain a sum of squares (Plummer 1918), making numerical integration a straightforward process according to Equation 1.14. In addition, these coordinates solve the Two Body and Restricted Three Body Problems exactly. However, the primary disadvantage is that a clear ordering of bodies is required for efficient integration in Jacobi coordinates. For example, orbits within a planetesimal disk frequently cross, and there is no straightforward and (computationally) cheap way to order these bodies.

## Democratic Heliocentric

In this coordinate system positions  $\mathbf{Q}$  and momenta  $\mathbf{P}$  form a canonical set with  $\mathbf{Q}$  measured relative to the central body and  $\mathbf{P}$  measuring barycentric momenta. These

coordinates are related to the cartesian position and momenta according to (Duncan et al. 1998):

$$\mathbf{Q}_i = \mathbf{r}_i - \mathbf{r}_0, \quad \mathbf{P}_i = \mathbf{p}_i - \frac{m_i}{M} \sum_{j=0}^N \mathbf{p}_j \quad (1.18)$$

For the special case of  $i = 0$ :

$$\mathbf{Q}_0 = \frac{1}{M} \sum_{j=0}^N m_j \mathbf{r}_j, \quad \mathbf{P}_0 = \sum_{j=0}^N \mathbf{p}_j \quad (1.19)$$

The benefit of Democratic Heliocentric coordinates is that they do not directly require other bodies to derive their positions (unlike Jacobi coordinates) and thus are conceptually easier to understand. However, these coordinates do not solve the Two Body Problem or Restricted Three Body Problems exactly. In addition,  $\mathcal{H}_K$  cannot be cleanly written as shown in Equation 1.15 due to several cross terms that arise when substituting  $\mathbf{Q}$  and  $\mathbf{P}$ . However, this problem can be rectified by transferring these cross terms into an additional “Jump” Hamiltonian:

$$\mathcal{H}_J = \frac{1}{2m_0} \left| \sum_{i=1}^N \mathbf{P}_i \right|^2 \quad (1.20)$$

Therefore, the evolution of  $\mathcal{H}$  in Equation 1.14 must be modified to include an additional evolution operator under the Jump Hamiltonian,  $E_{\mathcal{H}_J}$ . Note that since  $\{\mathcal{H}_J, \mathcal{H}_I\} = 0$ , the ordering of  $E_{\mathcal{H}_I}$  and  $E_{\mathcal{H}_J}$  does not matter.

## WHDS

The WHDS is a modification of the Democratic Heliocentric mapping and splits the kinetic energy slightly differently. The canonical coordinates  $\mathbf{Q}$  and  $\mathbf{P}$  have the same form, but the Keplerian, Interaction and Jump steps are now (Laskar & Robutel 1995;

Wisdom 2006; Hernandez & Dehnen 2016):

$$\begin{aligned}
\mathcal{H}_K &= \sum_{i=1}^N \frac{\mathbf{P}_i^2}{2\mu_i} - \frac{G(m_0 + m_i)\mu_i}{\mathbf{Q}_i} \\
\mathcal{H}_I &= \sum_{i=1}^N \sum_{j=1, j \neq i}^N \frac{Gm_i m_j}{|\mathbf{Q}_i - \mathbf{Q}_j|} \\
\mathcal{H}_J &= \sum_{i=1}^N \sum_{j=1, j \neq i}^N \frac{\mathbf{P}_i \cdot \mathbf{P}_j}{m_0}
\end{aligned} \tag{1.21}$$

where  $\mu \equiv m_i m_0 / (m_0 + m_i)$ .

The benefit of these coordinates is that, unlike Democratic Heliocentric coordinates, the Two Body and Restricted Three Body Problems are now solved exactly. In addition, (like Democratic Heliocentric coordinates) a particle's position are not dependent upon any other bodies. One price to pay for these benefits is that  $\{\mathcal{H}_J, \mathcal{H}_I\} \neq 0$ , and in Equation 1.14  $E_{\mathcal{H}_J}$  must be exactly nestled in between the  $E_{\mathcal{H}_K}$  and  $E_{\mathcal{H}_I}$  operators. In addition, the standard symplectic correctors of Wisdom (2006) cannot be used in this coordinate system, however other correctors may be possible to construct.

### 1.4.3 Integrator Types

The three main classes of N-body integrators are symplectic, non-symplectic and hybrid. Symplectic integrators employ a fixed timestep, bounded energy error (excepting bias and roundoff errors which grow with time) and fast integration time. These integrators are best suited for well-separated bodies where  $\mathcal{H}_I \ll \mathcal{H}_K$ , otherwise the energy error increases dramatically or the timestep must be changed, both of which break symplecticity. The most popular symplectic integrator is the Wisdom-Holman mapping (Wisdom & Holman 1991).

Non-symplectic integrators do not require a fixed timestep and do not have a bounded energy error over time. However, these integrators can employ very accurate and precise numerical convergence schemes, for example the Burlish-Stoer or predictor-corrector algorithms (Press et al. 2002). As a result, non-symplectic integrators are

typically more accurate but slower than their symplectic counterparts, and can solve most classes of planetary physics problems. A popular non-symplectic integrator is IAS15 (Rein & Spiegel 2015).

Hybrid integrators typically mix the symplectic and non-symplectic schemes, applying the symplectic component on bodies that are distant and non-symplectic component on bodies that are close. However, there are hybrid schemes that purely rely on symplectic principles (e.g. Duncan et al. 1998). As a result, hybrid integrators are often an optimal balance between speed and accuracy, especially for problems involving numerous close encounters. The most popular hybrid integrator is *Mercury* (Chambers 1999).

## 1.5 This Work

The work presented in this thesis focusses on the dynamics, formation and statistics of planetary systems. Chapter 2 deals with a statistical analysis of *Kepler* planets while incorporating the large radius errors present in the *Kepler* data. As mentioned in Section 1.1.2, the analyses by Fressin et al. (2013) and Petigura et al. (2013) ignored these large errors in planetary radius, affecting their calculations of planet occurrence.

Chapter 3 investigates the role of tides in transporting planets from exact MMR commensurability to a few percent wide. From Figure 1.1, an excess of planets is seen wide of the 3:2 MMR, and to some degree the 2:1 MMR as well. As mentioned in Section 1.3.1, it is believed that these planets were originally trapped in MMR and some mechanism transported them a few percent wide. Other studies have investigated the role of tides in transporting planets from MMR using analytical (Lee et al. 2013; Delisle et al. 2014) means, but no one has yet investigated this question numerically. Although computationally expensive, N-body simulations are very accurate and avoid approximations.

Chapter 4 presents HERMES, a hybrid integrator for simulating planetesimal migration, built from IAS15 (Rein & Spiegel 2015) and WHFAST (Rein & Tamayo 2015). The primary motivation for building HERMES is to investigate the role of planetesimals in transporting planets from MMR. Other scientists (Chatterjee & Ford 2015) have researched this question, but further investigation is required before conclusive answer is established. As outlined in Section 1.4.3, hybrid integrators are best for simulating planets embedded in planetesimal disks.

Chapter 5 investigates the role of machine learning in predicting the longterm stability of planetary systems. As stated in Section 6.5, due to the non-integrable and chaotic nature of multi-planet systems, classification of planetary stability is difficult without performing numerous costly N-body simulations. However, using information from the initial conditions and early evolution, a trained machine learning algorithm can accurately predict whether a planetary system will be longterm stable. This tool is useful to the scientific community due to its speed in classifying systems over brute-force N-body integrations.

Finally, in Chapter 6 the radial velocity data of HD155358 is analyzed. The system consists of two Jovian-sized planets orbiting a few percent from the 2:1 MMR around a  $0.92M_{\odot}$  star. This system was previously analyzed by Robertson et al. (2012), but they did not account for gravitational planet-planet interactions when deriving the orbital parameters. As mentioned in Section 1.1.1, neglecting planet-planet interactions in the orbital fit is only valid when the interactions are weak, and careful numerical treatments must otherwise be used. In addition, as mentioned in Section 1.3.2 planets near MMR are likely to have formed via migration. Thus, in addition to deriving updated orbital parameters I also assess the probability that the planets are in MMR, and analyze the formation and longterm stability of the system.

## Chapter 2

# A Statistical Reconstruction of the Planet Population around Kepler Solar-Type Stars

### 2.1 Chapter Overview

Using the most recent Kepler catalog, we reconstruct the occurrence rate of small (Neptune-sized or below) planets as a function of orbital period and planet radius, taking careful account of various detection biases. We analyze a sample of 76,000 Sun-like stars and their associated planet candidates with periods between 20 and 200 days, and sizes between 1 and  $4R_{\oplus}$ . Such planets have likely experienced little photoevaporation, and may reflect the “primordial” planet population. Assuming that the size distribution of planets are independent of their orbital periods (and vice versa), we conclude that Kepler planets are preferentially peaked at  $2 - 2.8R_{\oplus}$ , with their numbers decreasing gradually toward smaller sizes. These planets are found roughly uniformly in logarithmic period. The average number of planets per star, in the stated period and size ranges, is  $0.46 \pm 0.03$ . This number rises by  $\sim 0.2$  if one includes planets inward of 20 days. Upon extrapolation we obtain an occurrence



rate, for Earth-like planets within the “habitable zone” (as calculated by 1-D climate models), of  $6.4^{+3.4}_{-1.1}\%$ . We discuss the astrophysical implications of our results.

In our study, we introduce a number of novel statistical approaches, including the adoption of the “iterative simulation” technique (in addition to the standard MCMC technique), incorporation of uncertainties in planet radii, and an improved consideration of detection bias. Our results largely agree with those from an earlier work by Petigura et al. (2013), based on different statistical treatments and noise models. However, this agreement masks two substantial underlying discrepancies that (to first order) cancel each other out.

## 2.2 Introduction

Anaximander of Miletus proposed that there were many Earth-like worlds<sup>1</sup>. In the twenty five centuries since the Ionian philosopher’s speculation, we have seen an accelerating convergence towards an answer: many if not most stars have planets, Earth-sized (and presumably rocky) bodies are more common than Jupiter-sized gaseous bodies, and some Earth-sized planets are on orbits in the so-called “habitable zones” of their stars. The most recent advances in this field have come from data collected by the *Kepler* transiting-planet mission (Borucki et al. 2010). Four years of observations of a  $\sim 100$  sq. deg. field have led to the identification thus far of 4254 candidate transiting planets, the vast majority of which are thought to be bona fide detections. About 84% of the candidates appear to be smaller than Neptune ( $3.88R_{\oplus}$ ).

Beyond simple human curiosity about the prevalence of Earth-like planets and possibility of life elsewhere, planet statistics provide an important test of planet formation models (e.g. Benz et al. 2014). For example, the distribution of planets with respect to orbital period and mean motion resonances test models of planet formation

---

<sup>1</sup>*Dissertation on the Philosophy of Aristotle, in which his Pricipal Physical and Metaphysical Dogmas are Unfolded*, transl. by T. Taylor, London, 1812

and early migration (e.g., Hansen & Murray 2013; Baruteau et al. 2013). Planet radius and period distributions can be combined to reconstruct the distribution of solid mass in disks (e.g., Chiang & Laughlin 2013; Raymond & Cossou 2014).

There have been many previous studies that use the *Kepler* data to infer the intrinsic population of planets around *Kepler* target stars, or subsets of those stars (e.g. Catanzarite & Shao 2011; Youdin 2011; Traub 2012; Howard et al. 2012; Fressin et al. 2013; Dressing & Charbonneau 2013; Gaidos 2013; Dong & Zhu 2013; Kopparapu 2013; Petigura et al. 2013). These works differ in their samples and methods, but are broadly consistent in estimating that the occurrence of planets on close orbits to be of order unity. Some of these works have estimated  $\eta_{\oplus}$ , the occurrence of Earth-size planets in a circumstellar “habitable zone” (where stellar irradiation is similar to the solar constant), and find that  $\eta_{\oplus}$  is of order tens of percent. Of particular interest to us is the work of Petigura et al. (2013, hereafter PHM13) who performed an independent analysis of the *Kepler* photometric lightcurves, both identifying candidate planet transits and determining the detection efficiency by injecting synthetic transit signals into *Kepler* lightcurves and recovering them. Among the salient conclusions from PHM13 are that the distribution of planets peaks at a radius of  $2\text{--}2.8R_{\oplus}$  and that,  $\eta_{\oplus}$  is about 22% (using a liberal definition of the habitable zone).

We identify two reasons to revisit the derivation of the *Kepler* planet population. Firstly, we want to more fully account for the uncertainties and biases in the *Kepler* data and related observations of the target stars. Secondly, we wish to consider a “primordial” planet population, and restrict our analysis to planets far enough from their host stars that their properties have not been altered by proximity since their formation.

Precise statements on the occurrence of planets requires rigorous statistical methods, full accounting of errors, and adequate assessment of potential biases. First, while the overall rate of “false positives” among *Kepler* candidate planets appears

to be low (Morton & Johnson 2011; Fressin et al. 2013), it is not uniform across all periods and all sizes (Santerne et al. 2013). Second, determination of planet occurrence from transit surveys requires accurate estimates of detection efficiency (also known as “completeness”), which depends on the parameters (i.e. density and/or radius) of not only the planet host stars but of the entire target catalog. The parameters of *Kepler* stars were first determined by combining multi-wavelength photometry, stellar models, and Bayesian inference (Brown et al. 2011). Colors of solar-type stars depend only weakly on gravity and metallicity, and parameter values based on photometry have large random and systematic errors in both effective temperature (Pinsonneault et al. 2012), gravity and luminosity class (Mann et al. 2012). Spectroscopy, asteroseismology, and improved stellar models have yielded more reliable parameters (Huber et al. 2014), especially for *Kepler* planet-hosting stars (*Kepler* Objects of Interest or KOIs). Nevertheless, 70% of all stars in the Huber et al. (2014) catalog have assigned parameters based on KIC photometry, and for reference the median upper and lower fractional errors in stellar radius among solar-type stars is 40% and 10%, respectively. Because the estimated radius of a planet detected by transit depends on the stellar radius, and the probability of transit depends on stellar density, these errors need to be taken into account when computing occurrence rates. Errors in luminosity also affect the certainty with which a planet can be assigned to a habitable zone described by a range of stellar irradiance (Gaidos 2013; Mann et al. 2013).

Third, biases if uncorrected or unaccounted for will distort our perspective on planet populations. Perhaps the most insidious is detection bias, where the properties of stars with detected planets are statistically different from that of the overall target population. The assumption that there is no such difference can lead to erroneous conclusions about the properties of stars with planets and occurrence rates. Mann et al. (2012) found that a large fraction of the reddest *Kepler* target stars are giants, even though virtually all red KOI hosts are dwarfs for the simple reason that it is

extremely difficult to detect a transiting planet around a giant star. They showed that dilution of the target catalog by giants had led to an underestimate of the occurrence rate and an incorrect claim that M dwarf hosts of detected planets are redder and thus more metal-rich than those without detected planets.

Gaidos & Mann (2013) showed that because the *Kepler* target catalog is essentially magnitude-limited, Malmquist bias combined with uncertainties in stellar parameters means that stellar distances are underestimated and many stars are likely to be more luminous, evolved, and larger than their nominal values. Follow-up observations and analysis thus far seem to confirm this (e.g. Bastien et al. 2014; Everett et al. 2013; Verner et al. 2011). Because transiting planet radius scales with increasing stellar radius, this means that planet radii are underestimated. Moreover, the rate of planet detection decreases with increasing stellar radius or density, thus for a given planet radius, the detection rate is overestimated and thus the occurrence is underestimated. Detection bias again means that any estimate of this effect based on the host stars of transiting planets is an *underestimate*: the effect will be greater among stars in the overall target catalog. Another bias is Eddington bias: scatter by error from more populated regions of parameter space into less populated regions will produces the opposite effect, i.e. occurrence will be overestimated (Gaidos 2013).

Previous analyses of the *Kepler* planet population have often not taken these errors or biases into account, and instead have considered only Poisson (counting) statistics (e.g. Petigura et al. 2013; Howard et al. 2012). More seriously, some estimates of detection completeness and hence occurrence are based on the properties of the host stars of detected planets, (e.g. Petigura et al. 2013), not the statistical properties of the catalog, thus inviting detection bias. Finally, many analyses were performed by binning the data into discrete bins of planet radius  $R_p$  and orbital period  $P$ . While simple and readily explicable, the binning method runs the risk of masking details of a distribution, especially that of radius, which may be important for testing theoretical

models.

In this work we wish to consider a “primordial” population of planets, as opposed to one that has evolved under the influence of the host star. Effects of the latter, including tidal heating (Jackson et al. 2008), atmospheric escape (Tian et al. 2005), ohmic heating (Batygin et al. 2011), and impact erosion (Marcus et al. 2009), act with an efficiency that is inversely proportional to the distance to the host star. In particular, Owen & Wu (2013) proposed that photoevaporation by stellar XUV irradiation have effectively removed the hydrogen envelopes of close-in planets ( $P \leq 10$  days), leading to the observed paucity of super-Earth sized planets in that neighbourhood. This process was also investigated for a few *Kepler* systems by Lopez et al. (2012). Regardless of the mechanism, the distinctiveness of the  $P < 20$  d and  $P > 20$  d populations (see, e.g. Youdin 2011) suggests that any analysis treat these separately. In this study, we focus exclusively on the latter population as we believe it is more likely to represent the “primordial” state. On the other hand, because of *Kepler*’s low efficiency at detecting long-period planets (see §2.4.1), we are forced to limit our consideration to planets with  $P < 200$ d.

Practical reasons also limit the range of planet radius  $R_p$  considered. Although *Kepler* can readily detect a transiting giant planet, the occurrence of these objects is indubitably much lower than that of smaller planets. The distribution with planet radius falls to a very low level beyond Neptune-size objects: only 8% of *Kepler* candidate planets have nominal radii  $> 8R_{\oplus}$ , and the false-positive rate increases as well (Santerne et al. 2012; Colón et al. 2012). Conversely, *Kepler* can detect planets smaller than  $1R_{\oplus}$  for only a tiny fraction of stars, mostly M dwarfs. For these reasons we restrict our analysis to a radius range of  $1-4R_{\oplus}$  over which statistically rigorous analyses can be performed.

In this contribution, we infer the intrinsic distribution of planets with  $20 < P < 200$  days (equivalent to 0.16-0.67 AU) and  $1R_{\oplus} < R_p < 4R_{\oplus}$  around solar-type stars as

observed by *Kepler* over its entire mission (Quarters 1-17). This analysis includes the effects of errors in stellar and planet radius, and takes into account some of the biases that may affect previous works. We introduce the method of iterative simulation to determine the radius distribution of planets without resorting to binning. We compare our results with those of PHM13 and also carry out a detailed comparison of the two methods to understand the source of any discrepancies. We use our simulations to assess the effect of systematic biases, including detection bias and an overall underestimate of stellar radius, on inferences of a planet population from the *Kepler* catalog.

## 2.3 Methods

### 2.3.1 Catalogs of Stars and Planets

We construct a stellar sample from the Huber et al. (2014) catalog of 196,468 stars observed during the *Kepler* mission (Quarters 1-17), selecting stars with radii  $0.8R_{\odot} < R_{*} < 1.2R_{\odot}$ . We restrict the sample to stars with a Kepler magnitude  $K_{mag} < 15.5$  to avoid faint stars with uncertain properties and noisy lightcurves. This leaves a sample of 76,711 solar-type stars, hereafter known as the “Solar76k” sample. Our planet sample is constructed from the 26 February 2014 version of the KOI catalog (Ramirez et al. 2014). Planet and stellar parameters are updated with values from Huber et al. (2014) where available. In addition to the cuts made on our stellar sample we also require  $20 < P < 200$  d,  $0.5R_{\oplus} < R_p < 6R_{\oplus}$  and  $\text{SNR} > 12$ . Although we are only interested in the occurrence of planets  $1R_{\oplus} < R_p < 4R_{\oplus}$ , we use a larger radius range for our analysis since these planets have a non-zero probability of being in our region of interest after accounting for radius errors (§2.3.3). This leaves us with 430 candidate planets, hereafter known as the “430KOI” sample. We also construct a second planet sample (used only in §2.4.2) using the same cuts above except relax the

period restriction to  $5 < P < 200$ . This leaves us with 1052 KOIs, hereafter known as the “1052KOI” sample.

To ease comparison with PHM13, we retrieve their vetted sample of 603 planet candidates that fall within  $5 < P < 100$  days. We update the stellar parameters where possible, using Huber et al. (2014). We hereafter refer to this planet sample as the “603PHM” sample.

### 2.3.2 Simulated Planet Detections

Our simulator synthesizes single planet-star pairs<sup>2</sup>, drawing stars from one of the catalogs described above, and planet parameters from a large “master” population as we describe in §2.3.3. We calculate whether each planet transits its host star in a probabilistic manner, and then determine whether *Kepler* could have detected it. We compare the properties of these simulated detections with the observed candidate *Kepler* planets, and modify the master population using two different techniques: Monte Carlo Markov Chain (MCMC) and Iterative Simulation (IS). In implementing our simulations we make two critical assumptions. First, that the orbital periods and radii of *Kepler* planets (as well as orbital eccentricities), are independently distributed, i.e. the occurrence is a separable function of period and radius:

$$\frac{d^2N}{d \log P d \log R} = p(P)r(R), \quad (2.1)$$

where  $p$  and  $r$  are some yet-to-be-determined functions. Note that we measure occurrence in logarithmic period and logarithmic radius. Second, we assume that these distributions do not vary over the range of stars considered. We discuss these assumptions in §2.6.1. In this study, we further specify that the period distribution is a power-law:

$$\frac{dN}{d \log P} = P^\alpha. \quad (2.2)$$

---

<sup>2</sup>We ignore the occurrence of multiple systems and assume that each planet has an independent occurrence.

The geometric probability that a planet transits its host star is (Winn 2010),

$$p = \frac{R_*}{a} \frac{1 + e \sin \omega}{1 - e^2} \quad (2.3)$$

where  $a$  is the semimajor axis,  $e$  the orbital eccentricity, and  $\omega$  the argument of periastron. While  $a$  can be calculated from  $P$  and the estimated mass of the host star, the orbital eccentricity of *Kepler* planets are unknown and must be estimated statistically. Assuming a Rayleigh distribution with dispersion  $\sigma_e$ , Moorhead et al. (2011) estimated  $\sigma_e = 0.2$  by studying the distribution of transit durations. This is likely affected by uncertain stellar radii and may be an overestimate. TTV studies have led to much smaller eccentricity dispersion ( $\sigma_e \sim$  a few percent), at least in multiple planet systems (Wu & Lithwick 2013; Hadden & Lithwick 2014). Here, we choose  $\sigma_e = 0.18$  and show that our results are not sensitive to the exact value of  $\sigma_e$  (§2.6.1). The underlying distribution of  $\omega$  can be safely assumed to be uniform over  $[0, 2\pi]$ . Integrating  $p$  over the distributions of  $e$  and  $\omega$ , Eq.2.3 becomes  $p = p_0 R_*/a$ , with  $p_0 = 1.073$ . As in previous works, we require that at least three transits have been observed. We scale every transit probability by  $(1/p_0)(a/R_*)_{max}$ , the inverse of the max transit probability, which preserves the relative occurrence of simulated transits but speeds up simulation time.

We now proceed to assign a transit duration,  $T$ , to a given transiting planet. We follow the procedure of Gaidos (2013) by setting

$$T = \tau^{2/3} p^{1/3} \Delta, \quad (2.4)$$

where  $\tau = 2\sqrt{R_*^3/(\pi G M_*)}$  is the stellar free-fall time,  $G$  the gravitational constant,  $M_*$  the stellar mass, and

$$\Delta = \frac{\sqrt{(1 - e^2)(1 - b^2)}}{1 + e \cos \omega}, \quad (2.5)$$

with  $b$  being the impact parameter. For  $a \gg R_*$ , the impact parameter  $b$  is uniformly distributed in the range  $[0, 1]$ . We then calculate  $dN/d\Delta$ , the likelihood of drawing



a given  $\Delta$ , or rather, its cumulative distribution,  $\overline{N(\Delta)} \equiv \overline{\frac{\int_0^\Delta dN}{d\Delta'}} d\Delta'$ , with the overbar indicating marginalization over  $e$  and  $\omega$  distributions. Using the chain rule, we find

$$\frac{dN}{d\Delta} d\Delta = \frac{dN}{db} \frac{db}{d\Delta} d\Delta = \frac{db}{d\Delta} d\Delta, \quad (2.6)$$

where we have used the fact that  $dN/db = 1$  (i.e.  $b$  is uniformly distributed) for transiting systems. As a result,  $\overline{N(\Delta)} = \bar{b} = \overline{\int_0^\Delta \frac{db}{d\Delta'} d\Delta'}$ . Inverting Eqn. 2.5 then yields:

$$\overline{N(\Delta)} = \int_0^1 \eta(e) de \int_0^{2\pi} \sqrt{1 - \frac{\Delta^2 (1 + e \cos \omega)^2}{(1 - e^2)}} d\omega, \quad (2.7)$$

where  $\eta(e)$  is the assumed eccentricity distribution.

We also need to assign a radius to each trial planet: this process differs between our MCMC and IS methods and is described in their respective sections. Moreover, in comparing the radius distribution of trial planets to the observations, we must take into account significant uncertainties in the radius of KOIs. We describe how we do this in the next section.

Our detection criterion is based on a comparison between the transit signal,  $(R_p/R_*)^2$ , and the effective noise over the transit duration. Fressin et al. (2013) established that at signal-to-noise  $\text{SNR} > 12$  the false-positive rate among *Kepler* KOIs is very low. PHM13 used this criterion for their analysis and we follow suit. Noise in *Kepler* lightcurves derives from photon (shot) noise, stellar variability, and measurement error (Koch et al. 2010). The *Kepler* team encapsulates the total noise of each star into quarterly transit durations of 3-hr, 6-hr and 12-hr, known as “CDPP” (Combined Differential Photometric Precision, Christiansen et al. 2012) values. For a given star in a given quarter, we generate the appropriate noise for transit duration  $T$ , by interpolating among the various CDPP values using a power-law model. Because sources of noise (e.g., stellar variability) are not necessarily “white”, the power-law index can and often does depart from -0.5, the white noise value.

We then calculate the total SNR of a model star-planet pair as

$$SNR = \left( \frac{R_p}{R_*} \right)^2 \left[ \sum_{j=1}^{17} \frac{n_j}{(\text{CDPP}_j)^2} \right]^{1/2}, \quad (2.8)$$

where  $n_j$  is the number of transits in quarter  $j$ , and  $\text{CDPP}_j$  is the interpolated CDPP value for that quarter. The system is proclaimed detectable if  $SNR > 12$ . Eq. 2.8 does not account for noise that is non-Gaussian or non-stationary on a timescale shorter than one observing quarter (90 d). However, the conservative requirement that  $SNR > 12$  for detection partially addresses this limitation and we consider the possible impact of this simplification in §2.5 when we compare our analysis to PHM13.

### 2.3.3 Uncertainties in Planet Radii

As described in §3.2, there are significant uncertainties in the radii of most KOIs (median uncertainty = 33%), primarily due to our limited knowledge of the host star. For example, this means that there is a non-negligible chance that a planet with a cataloged radius value of  $R_p = 2.5R_\oplus$  is actually Earth-sized or Neptune-sized. It is important that uncertainties of such magnitude be considered, and we do this by replacing each nominal radius by a distribution of radii governed by Bayesian statistics. The probability that a planet with a reported radius  $R$  actually has a true radius  $R'$  is given by  $p(R'|R) = q(R|R')r(R')$ , where  $r(R')$  is a normalized prior and is the probability that a planet of radius  $R'$  (with same period  $P$ ) would be detected by *Kepler* around a given star. Put another way,  $r(R')$  is essentially the survey completeness (§2.4.1) of planet  $R'$  (having period  $P$ ) with respect to the entire Solar76k catalog.

In our treatment, we assume that errors in  $R_*$  and hence  $R_p$  are normally distributed. This means that  $q(R|R') = q(R'|R)$  because the Gaussian only depends on the square of the difference  $R - R'$ . We also assume that the two errors are uncorrelated. This latter assumption means that a planet with a radius that has been

over/underestimated would, on average, produce a weaker/stronger transit signal among the ensemble of target stars and that such a planet would become less/more detectable. If errors in  $R_*$  are exactly correlated, then errors in  $R_p$  are unaffected by considerations of detection; if all stars are smaller then their planets will also be smaller but by the same proportion, and thus produce transit signals of the same depth.

Provided these assumptions hold, a planet cannot be arbitrarily small, even if the errors in radius are large, because it would never have been detected in the first place. The  $r(R')$  factor accounts for this fact. Our prescription for handling radius errors also accounts for the fact that the cataloged radius is more likely to be an underestimate, rather than an overestimate, of the true radius. This effect becomes most pronounced among KOIs with small cataloged radii and large uncertainty. For these cases the result is an error distribution that is no longer a Gaussian but is strongly asymmetric, with a cutoff just below the cataloged radius and an extended tail to larger radii.

We implement radius errors into our analysis by replacing each KOI with a probability distribution function (PDF) that is the product of a Gaussian times a prior detection function which is the fraction of stars around which the planet would be detected (i.e. completeness). We represent the PDF by a large number of Monte Carlo planets drawn from a Gaussian distribution with mean equal to the nominal value of  $R_p$  and standard deviation equal to the cataloged error. We calculate the fraction of stars  $F$  around which each Monte Carlo planet could be detected. We then compute a normalized CDF of  $F$  with  $R_p$  for each Monte Carlo set. We can then draw a radius value from each corrected error distribution by comparing the CDF to a unit random deviate. We create a “master” radius distribution by randomly drawing 2 million values from all of these distributions according to their CDFs. We use this distribution to represent the inferred radius distribution of observed candidate planets after errors have been accounted for.

### 2.3.4 Monte Carlo Markov Chain

We discretize the radius-period plane into 16 bins, 4 period bins equally spaced in  $\log P$  ( $P = [20-40, 40-80, 80-160, 160-200]$  days) and 4 radius bins equally spaced in  $\log R$  ( $1-1.4R_{\oplus}, 1.4-2R_{\oplus}, 2-2.8R_{\oplus}, 2.8-4R_{\oplus}$ ). We parametrize the planet population by a set of 4 parameters:  $\alpha$  (from Eq.2.2), and  $\kappa_1, \kappa_2, \kappa_3$ , where the latter 3 parameters are the relative numbers of planets in the first 3 radius bins to the last bin. For each set of parameters, we generate a mock catalog by simulating  $10^5$  transiting pairs around a given stellar sample (§2.3.2) while properly taking into account errors in planet radius (§2.3.3). We then compare our mock population against the 430KOI sample by first binning the KOIs in the same manner and then removing a portion from each bin to account for false positives (Table 1 from Fressin et al. 2013). We then scale our mock catalog down from  $10^5$  to match the total number of remaining KOIs. The goodness of fit is measured by comparing the simulated number of planets in each of the 16 bins,  $S_i$ , versus that of the observed,  $D_i$ ,

$$\chi^2 = \sum_{i=1}^{16} \frac{(D_i - S_i)^2}{S_i}, \quad (2.9)$$

Here, we have assumed that the error in each bin is dominated by Poisson error. Our Markov chain is run for 4000 iterations, with a “burn in” of 200 steps that are excluded from subsequent statistical analysis. A new set of parameters are accepted if  $\chi_n^2 < \chi_{n-1}^2$ , where the index refers to the Markov step. If  $\chi_n^2 > \chi_{n-1}^2$ , the algorithm accepts the new parameter set with probability  $e^{-(\chi_n^2 - \chi_{n-1}^2)/2}$ . We adopt the medians of the accepted steps as the best-fit set, and we calculate both upper and lower standard errors using the 16th and 84th percentile values. The error of the  $2.8 < R_p < 4$  bin is calculated from the standard deviation of  $1/\kappa_3$ , i.e. the relative occurrence of the  $2.8-4R_{\oplus}$  bin with respect to the  $2-2.8R_{\oplus}$  bin.

### 2.3.5 Iterative Simulation (IS)

We use the method of Iterative Simulation (IS) to infer the intrinsic planet radius distribution without resorting to binning. In this technique we first generate a trial population of planets by simulating detections (§2.3.2). The radii of these simulated detections are then replaced by actual KOIs, and the process repeats until the simulated detections converge on the observations. The radius distribution of the trial population then reflects that of the intrinsic population of planets. With a sufficiently large trial population, the resolution of the radius distribution is limited only by the amount of information in the observations (i.e. KOIs), not the size of bins. We refer the reader to Gelman & Rubin (1992) for a general explanation of the IS method.

Our IS simulates  $10^6$  transiting planet-star pairs, drawing stars from the selected catalog with replacement (§2.3.2). Eccentricities and arguments of periastron of trial planets are drawn from Rayleigh and uniform distributions and periods are drawn from a power-law with the index of the best-fit MCMC model (§2.3.4),  $\alpha = -0.04$ . Planet radii are initially drawn from a uniform distribution over  $0.5-6R_{\oplus}$ . Detections are simulated as described in §2.3.2. We randomly replace the radii of all simulated detected planets with values drawn from the “master” radius distribution (§2.3.3), after correcting for false positives using the rates in Table 1 of Fressin et al. (2013). We then redraw new values for all the other planet parameters besides radius and period, and reshuffle the planets among the stars. We repeat this process until acceptable convergence is achieved, usually within 100 iterations. At this point, the trial population is used to calculate the intrinsic radius distribution.

Errors are calculated by constructing 50 bootstrapped samples of the detected planet catalog. The size of each sample is a random Poisson deviate with expectation equal to the size of the actual sample. The bootstrapped samples are drawn with replacement from the actual KOI sample. Planets are randomly removed according to the false positive probabilities of Fressin et al. (2013) and then intrinsic radius distri-

butions are calculated as in §2.3.3. For our bootstrapped samples we make the false positive correction before constructing the much larger intrinsic distribution to capture the contribution of false positives to the “noisiness” of each bootstrapped sample. We analyze each sample using the IS technique and compute standard deviations of the ensemble of bootstrapped planet populations to represent  $1\sigma$  uncertainties.

Figure 2.1 shows the results of an artificial test case of the reconstruction of a planet radius distribution using the IS technique. The intrinsic distribution (dashed line) is the sum of a Gaussian plus a rising slope. The dotted line is the distribution of 364 simulated observations, which is similar in scale to our 430KOI sample. We apply the IS technique on these simulated observations to recover the actual distribution: the result is plotted as the solid line, with error bars determined from 25 bootstrapped runs. The ability of IS to reconstruct an intrinsic distribution is limited by the information available in any region of a distribution, i.e. it will fail where the number of planets or rate of detection is too low. In Fig. 2.1, errors or large uncertainties appear in the reconstructed at  $R_p \sim 1R_\oplus$  where the detection efficiency is low. Also, in this simple demonstration we ignore the effect of planet radius errors. Adding planet errors tends to broaden and smooth features.

### 2.3.6 Calculation of Occurrence

After obtaining best-fit distributions from our MCMC and IS analyses, we calculate the rate of planet occurrence as a function of  $P$  and  $R_p$ . We generate  $10^6$  mock pairs and the corresponding simulated detections (§2.3.2). These planets are binned in a logarithmic grid of  $P$  (index  $i$ ) and  $R_p$  (index  $j$ ). The occurrence  $f(i, j)$  in the bin  $(i, j)$  is then

$$f(i, j) = \frac{K_{ij}}{N_*} \frac{N_{*,S}}{S}, \quad (2.10)$$

where  $K_{ij}$  is the false positive-corrected (Table 1, Fressin et al. 2013) number of KOIs falling into the bin  $(i, j)$ ,  $N_*$  (=76,711) is the total number of Kepler target stars in the

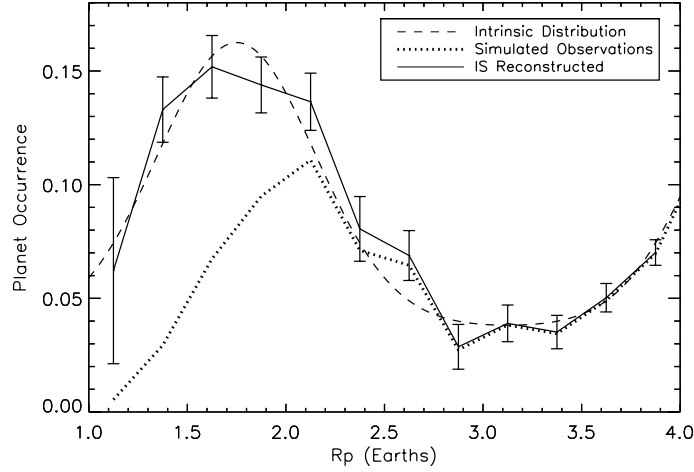


Figure 2.1: A test case demonstrating the recovery of a known, artificial radius distribution (dashed line) using the method of iterative simulation. The dotted line represents the simulated observations, which consist of 364 detections, and the solid line is the reconstructed distribution (here binned for display). Error bars are determined from 25 bootstrapped simulations.

Solar76k sample,  $N_{*,S}(=10^6)$  is the total number of mock pairs, and  $S$  is the number of simulated detections. The ratio  $S/N_{*,S}$ , the fraction of mock pairs that should be detected, and is the product of the geometric factor  $R_*/a$  as well as the detection completeness in bin  $(i, j)$ , hereafter known as  $C(i, j)$  (see §2.4.1). We then sum over all bins to obtain the total occurrence,  $f$ .

To demonstrate the importance of accounting for radius errors (§2.3.3) when calculating occurrence, we also conduct a separate analysis which excludes radius errors. Observed planets are binned as above and we calculate the occurrence of each bin,  $f$  according to:

$$f(P_i, R_i) = \frac{1}{N_*} \sum_k^{n_p(i,j)} \left( \frac{a_k}{R_{*,k}} \frac{1}{C(i, j)} \right) \quad (2.11)$$

Where  $C(i, j)$  is the average completeness of the bin (see §2.4.1),  $n_p(i, j)$  is the number of planets in bin  $(i, j)$ ,  $N_*$  ( $=76,711$ ) is the total number of stars in the sample and  $a_k/R_{*,k}$  is the geometric correction factor for planet  $k$ . The geometric effect here does not include a factor  $\mathcal{O}(1)$  that accounts for non-zero orbital eccentricities.

Lastly, in order to compare to PHM13, we estimate  $f$  without correcting for radius errors, as well as calculate the completeness  $C$  based on the *detected systems*, not the entire target catalog as in Eqn. 2.11. Simulations and observations are binned as above and we calculate the occurrence of each bin according to:

$$f_b(P_i, R_i) = \frac{1}{N_*} \sum_k^{n_p(i,j)} \left( \frac{a_k}{R_{*,k}} \frac{1}{C_k} \right) \quad (2.12)$$

where the sum is over detected systems in the bin  $n_p(i, j)$  and  $C_k$  is the completeness of planet  $k$  around star  $k$ . As above, the geometric effect here also does not include a factor  $\mathcal{O}(1)$  that accounts for non-zero orbital eccentricities.

For clarity, we underscore an important difference between these last two equations - the completeness  $C(i, j)$  used in Eqn. 2.11 is calculated from the *entire target catalog* for each bin, while  $C_k$  in Eqn. 2.12 is calculated from the *detected systems on a system-by-system basis*. As we will see in §2.5, this difference makes a significant impact on the occurrence.

## 2.4 The Primordial Population of Kepler Planets

### 2.4.1 Completeness

For a transit survey, completeness is the fraction of transiting planets of a given  $P$  and  $R_p$  that are actually detected, i.e. not including the geometric transit probability. Accurately capturing the dependence of completeness on  $R_p$  and  $P$  is crucial to a robust determination of planet occurrence.

We emphasize that survey completeness depends, not only on the properties of the planet host stars, but also on the stellar and noise properties of the *entire catalog*. We calculate the completeness  $C(i, j)$  of bin  $(i, j)$  by inserting  $2 \times 10^4$  planets randomly distributed around the Solar76k sample of stars. The fraction of “detected” planets,



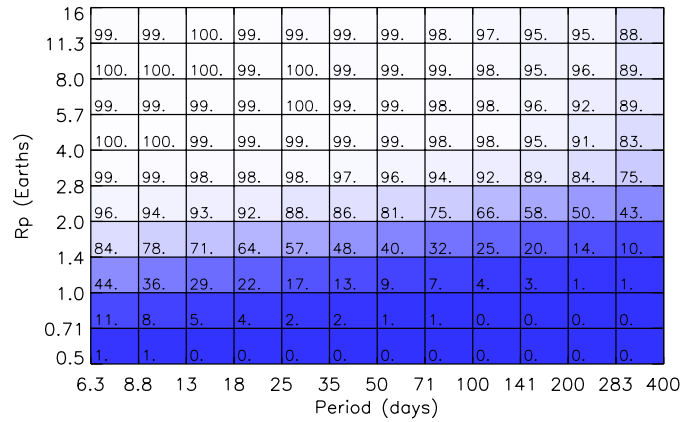


Figure 2.2: Completeness values for *Kepler* planet detection around stars in the Solar76k catalog. The numbers within each grid cell indicate the completeness percentage, and each grid has been colour coded from low (blue) to high (white) completeness.

modulo the transit probability factor, yields the completeness in this bin. The results are displayed in Figure 2.2.

Figure 2.2 shows that *Kepler* completeness is nearly 100% for planets larger than Neptune ( $3.8R_{\oplus}$ ), for nearly the full range of periods shown here. This falls rapidly beyond  $P \sim 500$  days (not shown) since some systems no longer have the required three transits during the four-year *Kepler* mission. The completeness drops rapidly with decreasing radius and/or increasing period: Earth-sized planets are readily detected by *Kepler* only if they have orbital periods of a few days, and beyond  $P = 200$  days, even the completeness of  $2R_{\oplus}$  planets falls below 50%. For these reasons we restrict our analysis to  $P < 200$ d.

Our completeness calculations consider the entire stellar population, while other works (e.g. PHM13) have considered only stars with detected planets. For large planets this difference is small, but for small planets the two methods diverge: completeness calculations from previous works lead to an *overestimate of completeness and thus an underestimate of planet occurrence*. This is particularly substantial for the smallest radius

bin. In §2.5 we compare our completeness results with those from PHM13.

## 2.4.2 Period Distribution

Our MCMC study yields a best-fit distribution for the 430KOI sample of  $\alpha = -0.04 \pm 0.09$ , with a reduced chi-squared  $\chi^2_\nu$  of 1.07. Our value of  $\alpha$  is consistent with zero (a flat logarithmic distribution) within errors, confirming previous determinations (e.g., Youdin 2011; Howard et al. 2012; Petigura et al. 2013; Fressin et al. 2013).

Figure 2.3 compares this best-fit period distribution with the observed sample (extended here to include planets inward of 20 days, i.e., the 1052KOI sample). Inside of  $P = 20$  days, *Kepler* planets deviate from a simple power-law distribution (also see Youdin 2011; Howard et al. 2012).

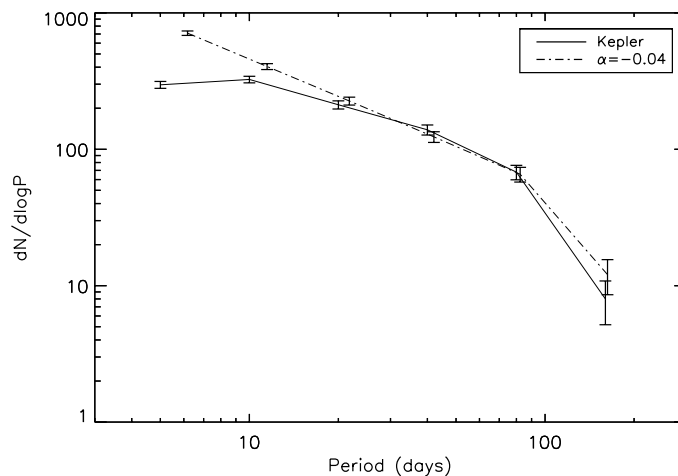


Figure 2.3: Period distribution of *Kepler* small planets. The observed distribution (solid line) includes planets inward of 20 days (i.e. the 1052KOI sample), while the simulated distribution from the MCMC best fit ( $\alpha = -0.04$ , see Eq.2.2) is plotted as a dashed-dotted curve. This best fit is obtained for planets in the  $20 < P < 200$  day range, but is extended here to shorter periods to demonstrate that the observed population deviates significantly from a single power-law shortward of 20 days. The scale in the vertical axis is arbitrarily chosen. Slight horizontal offsets have been applied to each curve for clarity.

### 2.4.3 Radius Distribution

Figure 2.4 displays our best-fit radius distributions for both the MCMC (solid, black) and IS (dotted, red) techniques, where we have binned the IS result for ease of comparison. Both the IS and MCMC distributions peak at  $2\text{--}2.8R_{\oplus}$  and decrease towards smaller radii. There is a small and statistically insignificant discrepancy between the MCMC and IS results at the smallest bin ( $1 < R_p < 1.4R_{\oplus}$ ). Since the two methods use identical input catalogs (§2.3.1) and detection algorithms (§2.3.2), the difference could be due to the intrinsic binning in the MCMC method. We have also plotted two additional distributions in Figure 2.4, a “No Error” case (dashed, green) constructed from Eq.2.11 and a “25% Larger” IS case (dashed-dotted, blue) where it is assumed that both planet and stellar radii are 25% larger than their catalog values.

As we discuss in §2.3.3, errors in the radius of candidate *Kepler* planets, primarily due to uncertainties in stellar radius, are large and detection bias against small planets means that a planet’s cataloged radius is likely an underestimate. Comparing our IS and MCMC results (which include radius errors) with our “No Error” case (which doesn’t include radius errors) we see that the latter exhibits a significant excess of  $1\text{--}1.4R_{\oplus}$  planets. This is as expected. Correcting for radius error in a Bayesian way (§2.3.3) tends to promote small planets to larger size bins, and de-populates the smallest radius bin. The occurrence of the larger bins however do not substantially increase because the survey completeness is substantially higher in these bins compared to the  $1\text{--}1.4R_{\oplus}$  bin. We conclude that not accounting for this detection bias on radius leads to an erroneously high (by a factor of  $\sim 2$ ) value of occurrence for the  $1\text{--}1.4R_{\oplus}$  bin.

If we assume the extreme scenario that the true radii of all stars (and therefore their planets) are 25% larger than the KOI values (“25% Larger” case in Fig. 2.4), as is shown to be the case for at least a subset of the *Kepler* stars (§2.6.1), we observe that the  $2\text{--}2.8R_{\oplus}$  peak is now shifted to  $2.8\text{--}4R_{\oplus}$ . However, we do not see a significant change in the bin  $1\text{--}1.4R_{\oplus}$  because the depopulation of this region (due to increased

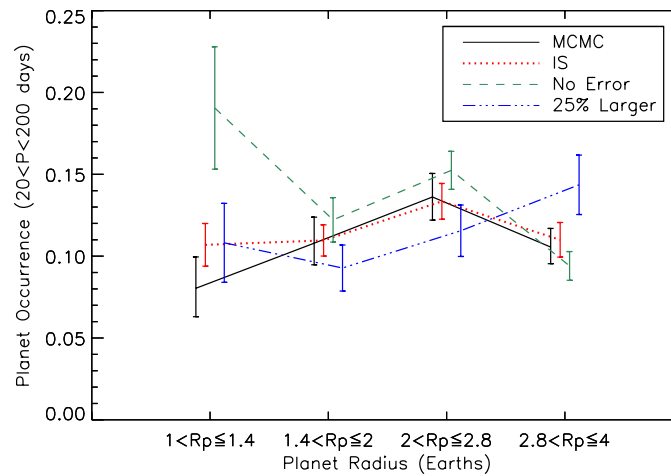


Figure 2.4: Size distribution of planets between 1 and  $4R_{\oplus}$ , obtained using the MCMC (solid black line) and the IS (dotted red line) techniques. Both show that planet occurrence peaks in the bin  $2 - 2.8R_{\oplus}$ . Earth-sized planets are less common, by a factor of  $\sim 2$ , although the statistical significance of this result is still low. If we assume that the currently determined planet radii carry no uncertainty, or that all stars (and hence planets) have 25% larger radii than their cataloged values, we obtain rather different radius distributions. The error bars for the “No Error” case account for poisson error only, while for the IS and 25% Larger cases, error bars are calculated from 50 bootstrapped simulations of the data (see §2.3.3). The MCMC error bars are calculated in the standard manner. Planet occurrence at each logarithmic radius bin is obtained by summing over all period bins. Slight horizontal offsets have been applied to each curve for clarity.

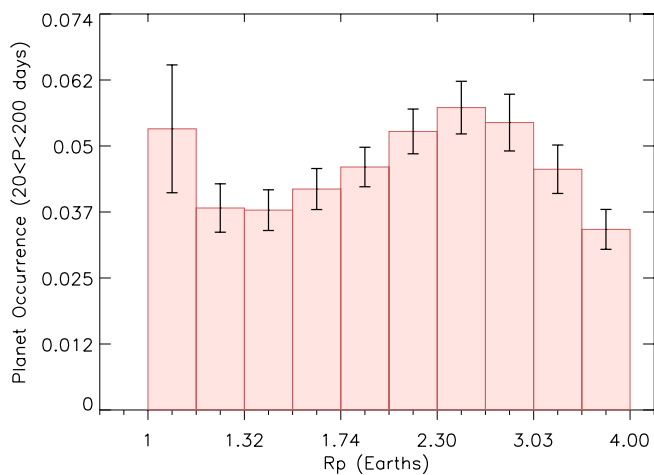


Figure 2.5: Our IS distribution displayed for a smaller logarithmic bin size. This finer resolution reveals more information about the intrinsic distribution, and specifically we see a potential rise in the number of  $1\text{--}1.15R_{\oplus}$  planets. This bin has large error however, and thus more statistics are required to confirm this conclusion.

planet radii) is roughly balanced by a decrease in completeness as the stars have also become larger. See §2.6.1 for a more detailed discussion.

We comment that our treatment for the radius error is far from perfect. Some genuinely small planets may, under our procedure, be wrongly inferred to have larger radii. A better treatment will require improved errors in stellar/planet radius (see, e.g. §2.6.3).

Lastly, we display the IS radius distribution for a smaller logarithmic bin size in Figure 2.5. As explained in §2.3.5, since the IS technique requires no binning, the resolution of the result is limited only by the data and its errors. This improved resolution can reveal finer detail about the intrinsic radius distribution. We observe a slight excess of planets in the now smallest bin ( $1\text{--}1.15R_{\oplus}$ ), over that in larger bins. Improved statistics is required to confirm this upward turn, but if it is true, it would imply a rising number of planets below the size of Earth, an exciting possibility for life elsewhere. We expect that, with its independence on binning, the IS technique

will become central to future analysis.

## 2.4.4 Total Occurrence of Small Planets

In Table 2.1 we report our estimates for the total planet occurrence within  $20 < P < 200$  days and  $1 < R_p < 4R_\oplus$ , for the four curves in Figure 2.4. There is excellent agreement between the MCMC and the IS results. Even cases with different assumption about the radius error yield statistically consistent occurrence rates.

PHM13 reported an occurrence of  $37\% \pm 3.4\%$  for planets with  $25 < P < 200$  days and  $1 < R_p < 4R_\oplus$ . Including planets from  $20 < P < 25$  days raises this value to  $42\% \pm 3.6\%$ . So the occurrence rates are consistent among studies that are based on different detection criteria and different model assumptions. We perform a detailed comparison with PHM13 in §2.5.

The total occurrence rate we calculate here is defined to be the average number of planets per star (Youdin 2011; Fressin et al. 2013; Petigura et al. 2013). Such a definition ignores the complication that many of the Kepler systems are multiple systems (e.g. ?). A quantity perhaps more relevant for studies of planet formation is the occurrence rate of planetary systems, or the average number of planetary systems a star has. However, this requires knowledge of the system architecture, a task not yet attempted.

Lastly, if we include small planets inward of 20 days, the total occurrence rate is raised to  $\sim 66\%$ . It will rise by another  $\sim 15\%$  if we include planets upward of  $4R_\oplus$ .

## Eta-Earth

We estimate  $\eta_\oplus$ , the occurrence of Earth-like planets in the “habitable zone” of solar-type stars. By Earth-like, we are referring to planets between  $1 - 2R_\oplus$ . We adopt the inner and outer boundaries of the habitable zone to be those calculated by the 1-D, cloud-free, climate models (Kasting et al. 1993; Kopparapu et al. 2013). For a

Table 2.1: Planet Occurrence for  $20 < P < 200$  days,  $1 < R_p < 4R_\oplus$ .

Technique	Planet Occurrence (%)
MCMC	$43 \pm 3$
IS	$46 \pm 3$
No Error	$56 \pm 10$
25% Larger Stars	$46 \pm 3$

sun-like star, these boundaries lie at 0.99 and 1.70 AU respectively (or orbital periods of 350 and 810 days); for other stellar spectral types, the boundaries are as tabulated in Kopparapu et al. (2013).

Such a habitable zone, however, lies outside the 200 day limit of our study. At these very long periods, the low detection efficiency of *Kepler* engenders inaccuracies in estimating  $\eta_\oplus$ . So instead, we have opted to calculate  $\eta_\oplus$  by extrapolation, according to:

$$\eta_\oplus = \frac{f}{N_*} \sum_{i=1}^{N_*} h_i \quad (2.13)$$

where  $N_*$  (=76,711) is the number of stars in the Solar76k sample and  $h_i$  is the relative occurrence of planets (per star) within the habitable zone to some reference zone having absolute occurrence  $f$ . We choose this reference zone to be our standard  $20 < P < 200$ d,  $1 < R_p < 4R_\oplus$  bound, with  $f = 0.46 \pm 0.03$  (IS value). We calculate  $h_i$  for each star by adopting the IS radius distribution (Figure 2.4) and integrating the MCMC best-fit power-law (Eq. 2.2 with  $\alpha = -0.04$ ) over each star's habitable limits (Kopparapu et al. 2013). Finally, we obtain

$$\eta_\oplus = 6.4^{+3.4}_{-1.1}\% \quad (2.14)$$

The error is calculated from error propagation of the IS radius distribution, occurrence of our reference zone, habitable zone limits (based on  $R_*$ ,  $M_*$ , and  $T_*$ ) and  $\alpha$ . This value is consistent within errors with the analysis done by PHM13 for the same

Kopparapu et al. (2013) limits, 8.6%. The reader is reminded that our calculation of  $\eta_{\oplus}$  is an extrapolation, and depends crucially on the assumptions made.

## 2.5 Comparison with PHM13

We now make a comparison to PHM13, an analysis which is similar to ours in terms of scope, but which obtains their results of the *Kepler* data using the TERRA pipeline (Petigura et al. 2013) - an analysis tool independent of the *Kepler* project pipeline and its products on which our work relies.

We first compare our estimates of detection completeness  $C$  with that of PHM13. For this comparison, we re-compute  $C$  using the Best42k stars from PHM13 and compare these results to the values in Figure S11 from PHM13. We calculate the fractional difference  $(2(T - P)/(T + P))$ , where  $T$ =This Work and  $P$ =PHM13) and display as percentages in Figure 2.6. With the exception of a single cell all values

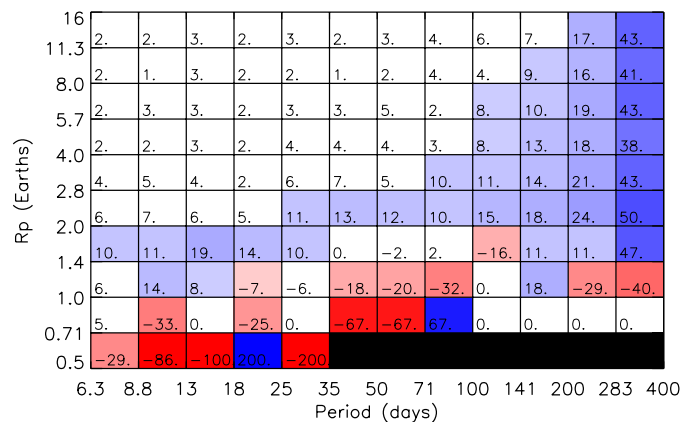


Figure 2.6: Comparison of completeness values computed with our methods to those reported by PHM13 in Figure S11, expressed as a fractional difference. Our values are generated using the “Best42k” catalog from PHM13 and our detection criteria. Bins where both our completeness and those of PHM13 are zero have been blacked out.



of  $C$  in the range  $P = 20 - 200$  days, and  $R_p = 1 - 4R_\oplus$  are within 20% of PHM13 values. This shows that even a comparatively simple description of *Kepler* planet detection can account for most of the statistics. The single exception is for the  $1-1.4R_\oplus$  and 71-100 d bin where our estimate of  $C$  is 32% lower than that of PHM13. This bin includes the 90 d roll-period of *Kepler*. Large systematics appear in raw *Kepler* lightcurves at this period because the stars change positions on the detector array. It might be expected that the planets with  $P$  near 90 days would be more difficult to detect than our naive criteria and that actual completeness would be lower. If the PHM13 values are more realistic, then the opposite appears to be the case. Elsewhere in  $P$ - $R_p$  space our completeness values are slightly and systematically higher than those of PHM13, and the discrepancy increases with increasing  $P$  and decreasing  $R_p$ . This is to be expected because PHM13 determine detection efficiency using actual lightcurves rather than representations of noise a la CDPP values. At  $P > 200$  d our values of  $C$  become significantly higher than PHM13 for nearly all values of  $R_p$ . This discrepancy motivates our restriction to  $P < 200$  days. One possible explanation for this difference is that detection of signals by phase-folding in the *Kepler* detection pipeline becomes inefficient at long periods.

We next compute the impact of these differences in completeness on occurrence over  $P = 5 - 100$  d, shown in Figure 2.7. We first calculated occurrence using the “603PHM” dataset (§2.3.1), Eqn. 2.11 along with our own detection criteria (§2.3.2) and completeness values (calculated from the Best42k sample), shown as the solid black curve in Figure 2.7. We then re-calculated planet occurrence using the 603PHM dataset, Eqn. 2.11 along with our own detection criteria but substituting in the completeness values from Figure S11 of PHM13 for ours, shown as the dashed green line in Fig. 2.7. The differences between the solid black and dashed green lines in Figure 2.7 are small and, within errors, agree with each other. The residual differences in completeness seen in Fig. 2.6 do not appear to play a significant role in the comparative occurrence

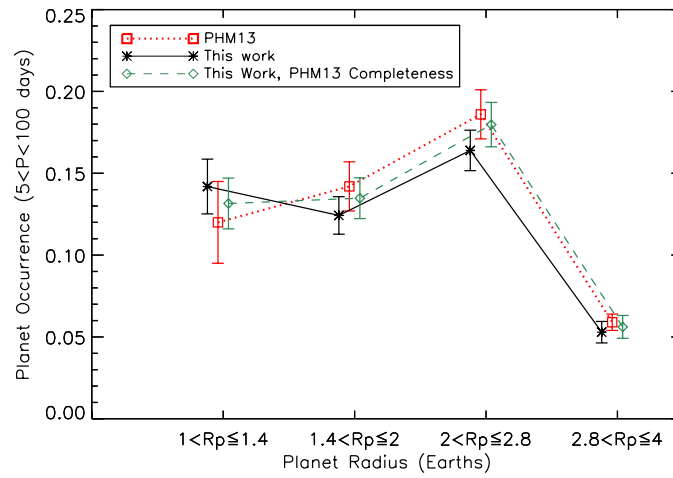


Figure 2.7: A summary of our comparison to PHM13. All curves are constructed using the “603PHM” dataset and “Best42k” sample. The results of PHM13 are plotted as the dotted curve in red with squares, “This work” using Equation 2.11 is the black solid curve in black with stars, “This work, PHM13 Completeness” using PHM13’s Figure S11 completeness values and Equation 2.11 is the green dashed curve with diamonds, and “This work, PHM13 Method” using PHM13’s method of calculating occurrence (i.e. Equation 2.12) is the blue dashed-dotted curve with triangles. Slight horizontal offsets have been applied to each curve for clarity.

of our work and that of PHM13 but could be responsible for some of the minor (and statistically insignificant) differences that we find. *We conclude that simple detection criteria and noise model can achieve accurate results.*

A second difference between our work and PHM13 is *which* completeness values are used to compute occurrence. PHM13 calculates occurrence using Eqn. 2.12, i.e. *based on the detection completeness of those systems which have detected planets*. As discussed in §3.2, if all else is equal, planets are more likely to be detected around those stars which are more amenable, i.e. smaller, brighter, and less “noisy”. Values of  $C$  for these stars will be higher than the overall target catalog, and thus  $f$  will be underestimated. In this work we instead calculate occurrence using the completeness of the entire target catalog for planets of a given  $P$  and  $R_p$  according to Eqn. 2.11.

This detection bias depends on how completeness varies from star to star. *Kepler* can detect planets larger than Neptune around essentially all solar-type target stars (Fig. 2.2) and hence we expect little to no detection bias in occurrence for this radius range. In contrast, *Kepler*’s detection of Earth-size planets is SNR limited and thus varies strongly between stars even within our target catalog. Figure 2.8 illustrates this concept, plotting a histogram of completeness values, calculated on a star-by-star basis for 20,000 Solar76k stars. We display two curves, a solid black line representing the distribution of  $P=30$ d Earth-sized ( $R_p = 1.25R_\oplus$ ) planets and a dashed red line for  $P=30$ d Neptune-sized ( $R_p = 3.75R_\oplus$ ) planets. For reference, the average completeness of a  $P = 30$ d Earth sized planet in the Solar76k sample is 21% while for Neptune it is 97%. Although both curves show some degree of completeness variation, we see significantly more variance among the Earth-sized planets and in particular a large number of Earth-sized planets above the average. If one calculates completeness based on detected systems alone, detection bias can become a dominant source of error in occurrence calculations. In general, as  $P$  decreases the variance in completeness for Earth-sized planets becomes even greater relative to Neptune-sized.

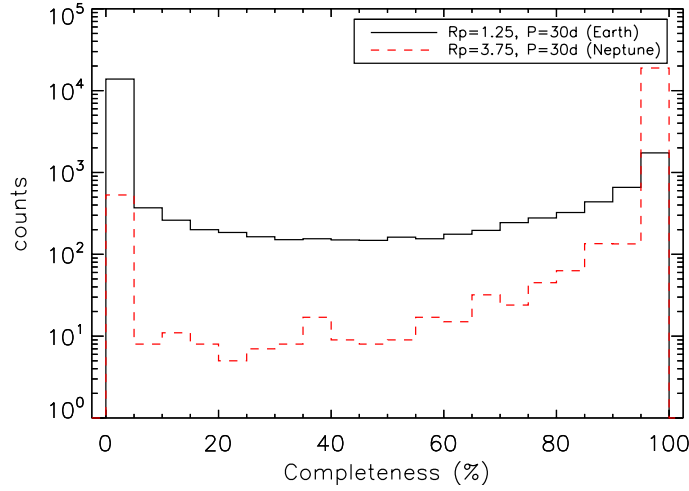


Figure 2.8: Distribution of completeness values for Earth-sized ( $R_p = 1.25R_\oplus$ , solid, black) and Neptune-sized ( $R_p = 3.75R_\oplus$ , dashed, red) planets among a collection of 20,000 stars from the Solar76k sample, calculated on a star-by-star basis. For these calculations, all planets have been assigned a period of 30 days. As is clearly seen, the completeness variation is much larger among the Earths vs. Neptunes, illustrating how one can introduce significant detection bias into the occurrence calculations of small planets if an average over all stars is not taken.

Thus we expect PHM13’s estimate of  $f$  for the smallest ( $1\text{--}1.4R_\oplus$ ) planets to be biased downwards. We quantify this bias by comparing the dotted-dashed blue curve in Figure 2.7 to the solid black curve. Both curves are constructed using our analysis procedures, detection criteria, the 603PHM dataset, and the the Best42k catalog of stars. The dotted-dashed blue curve labelled “This Work, PHM13 Method” uses Eqn 2.12 (and hence the completeness for stars with detected planets) to calculate  $f$  while the solid black curve labelled “This work” uses Eqn. 2.11 (and hence the overall completeness) to calculate occurrence. As expected, a downward bias in occurrence appears at  $R_p < 2R_\oplus$  where *Kepler* observations are not complete. The bias increases with decreasing  $R_p$ , reaching a factor of two for the smallest bin.

Referring to Figure 2.7, the dashed-dotted blue curve labelled “This Work, PHM13 Method” represents our best attempt to replicate the results of PHM13 according

to the methods they describe. However, this curve underestimates occurrence for  $1-2.8R_{\oplus}$  compared to PHM13 (dotted, red). One explanation for this discrepancy is that the equation actually used by PHM13 is not the one given in the paper. For example, Howard et al. (2012) use an equation that is a better approximation for  $f$  because the numerator contains only the number of stars around which a planet could be detected, not all stars in the target catalog. If PHM13 instead used their Figure S11 for calculating planet occurrence (i.e. Eq. 2.11 instead of Eq. 2.12), then our most direct comparison to PHM13’s results (dotted, red) in Figure 2.7 is the solid black curve labelled “This Work”, in which case there is good agreement within error.

To summarize our comparison with PHM13 using Fig. 2.7, we have shown that (1) substituting the survey completeness values of PHM13 (Fig. S11 of Petigura et al. (2013)) for our values have a negligible effect on the results (green vs. black curve); (2) that emulation PHM13’s method to calculate occurrence produces significantly lower values of occurrence for the smallest planets because the completeness of systems with detected planets is biased upwards with respect to the overall survey; and finally (3) it appears that the approximate agreement between our results in §2.4.3 and those of PHM13 is coincidence brought about by the cancellation of two systematic effects – detection bias and radius errors – which act in roughly equal and opposite ways on estimates of the occurrence of the smallest planets.

## 2.6 Discussion

### 2.6.1 Sensitivities and Systematics

To investigate sensitivities to some of the assumptions and parameters in our analysis, we repeated our IS simulations, varying  $\sigma_e$  for the Rayleigh distribution of orbital eccentricities between 0.1 and 0.3, and the value of  $\alpha$  between -0.15 and 0.15. We found no significant difference in the radius distributions. We also investigate our

separability assumption (Eqn. 2.1) by performing a series of IS calculations where we first scramble the period values in our dataset and then extract the resulting radius distribution. We find no significant deviation between these results and our main IS result, implying that there is no significant correlation between planet radius and period in our sample, and that Eqn. 2.1 is a reasonable assumption.

In this analysis, we address the fact that many *Kepler* planets have large errors in radius, driven primarily by uncertainties in the radii of their host stars. But we have not addressed the issue of systematic errors in stellar radii. For example, stellar effective temperatures based on photometry from KIC (Brown et al. 2011) are systematically  $\sim 200$  K hotter than more reliable estimates based on the infrared flux method (Pinsonneault et al. 2012) or spectroscopy (Gaidos 2013). The combination of uncertainties in stellar parameters and Malmquist bias in the magnitude-limited *Kepler* target catalog means that the sample is biased towards the most luminous, hottest, and largest stars (Gaidos & Mann 2013). There is increasing evidence that many *Kepler* target stars, including planet hosts, are subgiants (e.g., Verner et al. 2011; Everett et al. 2013; Bastien et al. 2014). For fixed values of  $R_p/R_*$ , systematically larger stellar radii means the planets are also systematically larger and that the geometric transit probability is higher than presumed (transit probability depends inversely on stellar density and hotter, more evolved stars are less dense). The detection completeness of small planets is also smaller than presumed and thus, for fixed number of detections, the occurrence is higher.

We have explored the possible impact of these effects by assuming that all stellar radii in our Solar76k catalog, as well as all the planet radii in the corresponding 450KOI catalog, are 25% larger than their nominal values (dashed-dotted blue curve, Fig.2.4). The distribution differs markedly from our IS and MCMC distributions. The peak in the distribution at  $2.28R_\oplus$  has shifted towards larger radii. Surprisingly, the occurrence of planets with  $R_p = 1 - 1.4R_\oplus$  has not changed. This is understood. As

stellar radii increase, completeness of small planets decrease leading to an increase in planet occurrence. However, the number of  $1-1.4R_{\oplus}$  planets in our sample also decreases (from 25 to 8 after a 25% radius increase), reducing the raw planet occurrence in this radius bin. It appears that these two competing effects roughly cancel, resulting in no significant change in planet occurrence of the smallest radius bin.

## 2.6.2 Astrophysical and Astrobiological Implications

The period distribution of *Kepler* small planets contains two distinct parts. The first is a rise from a few stellar radii out to  $\sim 10$  days (e.g. Youdin 2011; Howard et al. 2012), the second is a logarithmically flat distribution extending from  $\sim 10$  days to as far as observations are sensitive to (Fig. 2.3 here, Petigura et al. 2013; Fressin et al. 2013). The origin of both features are unclear.

We speculate on one origin for the logarithmically flat feature. Imagine a set of planetary systems comprised of closely-packed, equal-mass planets. Dynamical stability requires that neighbouring planets be spaced apart by more than a few Hill radii (Chambers et al. 1996; Smith & Lissauer 2009). Since the Hill radius scales linearly with orbital semi-major axis, this means the separation between neighbouring planets grows linearly with their orbital span. This would then translate into a period distribution that is flat in logarithmic period. In other words, it is possible that most or all of our planets are actually in multiple systems, and that the flat feature is a result of the stability requirement.

Alternatively, the flat feature can arise from the primordial mass distribution in the disk. Assuming that all planets have comparable masses, are in multiple systems, and are formed where they are found today, a logarithmically flat spacing would suggest that the disk surface density  $\Sigma$  scales with the orbital separation  $a$  as,

$$\Sigma \propto a^{-2}. \quad (2.15)$$

This is not vastly different from the theoretical MMSN profile:  $\Sigma \propto a^{-3/2}$  (Hayashi 1981; Weidenschilling 1977a), a useful benchmark to study proto-planetary disks.

The radius distribution is equally intriguing. The radius of a planet mostly reflects the expanse of its hydrogen envelope. By focussing on planets outward of 20 days, we discard candidates that may have had their atmospheres eroded by stellar irradiation. The distribution shown in Fig.2.4 is therefore likely “primordial”. Compared to planets inward of 10 days that have radii  $\leq 1.5R_{\oplus}$ , this “primordial” population appears to prefer a size of  $\sim 2.5R_{\oplus}$ . Such a size corresponds to a fractional mass in the hydrogen envelope of  $\sim 1\%$  (see, e.g. Wu & Lithwick 2013). What is the reason behind this preference for 1%? A planet embedded in a proto-planetary disk can accrete a hydro-static atmosphere. Rafikov (2006) calculated that this atmosphere has a mass of a few  $M_{\oplus}$  for a  $10M_{\oplus}$  planet at 0.1 AU in a MMSN disk. This lies much above the 1% value but it depends on disk parameters and its evolution history. In future works, the observed radius distribution should be used to decipher formation history.

Moreover, the gradual decline toward smaller sizes in logarithmic space has implication for the formation of bare-core planets, the norm in the inner Solar system. Our terrestrial planets are thought to have formed in a gas-free environment by conglomeration of solid materials. The relative shortage of bare-core planets may suggest that the observed *Kepler* planets may have followed different formation path than that of the terrestrial planets.

Lastly, we turn to the issue of  $\eta_{\oplus}$ . We calculate  $\eta_{\oplus}$  more out of respect for tradition than with any conviction that there is additional accuracy to be assigned to our calculation. The limits of the habitable zone depend on important assumptions regarding the climate state of Earth-like planets (Kopparapu et al. 2013), mass (Kopparapu et al. 2014), and the composition of the atmosphere (Pierrehumbert & Gaidos 2011). Nevertheless, the search for life elsewhere can take heart in the fact that multiple



investigations point to an occurrence of Earth-size planets in habitable zones of  $\mathcal{O}(0.1)$  or more. Indeed, studies of M dwarfs suggest that  $\eta_{\oplus} \sim 0.5$  (Bonfils et al. 2013; Kopparapu 2013; Gaidos 2013). M dwarfs comprise about 70% of all stars and hence weigh heavily in the census for Earth-like planets.

### 2.6.3 Improvements in Occurrence will Happen

The errors associated with most *Kepler* planets are dominated by the uncertainty in the parameters of their host stars. Thus, in order to improve planet occurrence calculations for the future we must first understand *Kepler* stars better. The *Gaia* (Global Astrometric Interferometer for Astrophysics) mission, launched in December 2013, will measure the parallaxes of 1 billion stars in the local group with accuracies approaching  $10 \mu\text{as}$ , as well as obtain multi-band photometry measurements (de Bruijne 2012). Liu et al. (2012) estimate that for stars in the KIC, *Gaia* will be able to estimate  $T_{\text{eff}}$  to 1%,  $\log g$  to within 0.1-0.2 dex, and  $[\text{Fe}/\text{H}]$  to within 0.1-0.2 dex. The combinations of these data should dramatically improve our knowledge of the properties of *Kepler* target stars and hence reconstructions of the *Kepler* planet population.

Other advances include improved maps of interstellar reddening in the *Kepler* field based on the colors of oscillating red giants with established properties, as well as WISE infrared photometry (Huber et al. 2014). The advent of multiplexed, multi-object spectrographs capable of simultaneously measuring thousands of stars (Hill et al. 2010) should, combined with *Gaia* parallaxes, allow stellar parameter estimation with unprecedented scale and precision. In addition, measurement of photometric noise due to stellar granulation (“flicker”) is a promising technique for estimating the  $\log g$  and hence radius of bright *Kepler* stars to within 0.1-0.2 dex (Bastien et al. 2014), although its calibration and applicability to fainter *Kepler* stars – the majority of targets, with lower photometric precision – remains to be seen.

## 2.7 Conclusions

In this work we have developed a population simulator designed to extract the underlying period and radius distributions of Earth to Neptune sized planets detected by *Kepler*. We focus on a “primordial” population of planets outside 20 days to exclude the impact of, e.g. photoevaporation. We find that the adoption of a simple model of photometric noise and transit signal detection allow us to accurately estimate the survey completeness of *Kepler*. We have accounted for radius errors in our analysis, and have found that doing so is important for reconstructing the intrinsic radius distribution. We apply the iterative simulation technique to reconstruct the planet distribution with radius. This does not require binning and allows radius errors to be readily accounted for. Lastly, we are the first to use the updated Huber et al. 2014 parameters along with all 17 quarters of *Kepler* data, representing the most up to date analysis. The main results are as follows:

1. The period distribution for  $20 < P < 200$  planets is roughly flat in logarithmic space ( $\alpha = -0.04 \pm 0.09$ ).
2. The (likely primordial) radius distribution for *Kepler* planets with  $20 < P < 200$ d peaks in the radius bin  $2 - 2.8R_{\oplus}$ . The frequency of Earth-sized planets are  $\sim$  twice lower than for these larger planets.
3. The overall occurrence of planets within  $20 < P < 200$  days and  $1 < R_p < 4R_{\oplus}$  is  $46\% \pm 3\%$ . This represents the average number of planets per star in the *Kepler* field.
4. Extrapolating our radius and period distributions out to the habitable zone for solar-type stars, we find  $\eta_{\oplus} = 6.4^{+3.4}_{-1.1}\%$ .

5. While our above results confirm those from earlier studies, our adoption of different statistical methods and our careful treatment of radius errors lend much weight to these conclusions. In a detailed comparison of our work with PHM13, we show that, while the two studies obtain similar size distribution, they come to it for different reasons. In particular, both the incorporation of radius errors and our improved completeness calculation have opposing effects on the distribution of small planets and to first order, cancel out.
6. Large radius errors are present in the Kepler data, and failing to account for these properly can lead to a different radius distribution. Specifically, this tends to result in a large excess of earth-sized planets. We also find that boosting stellar/planetary radii over values reported in the *Kepler* catalog increases the frequency of large planets. Many stellar radii in the *Kepler* catalog are suspected to be underestimated. GAIA will improve these stellar radius errors and resolve this issue.

## 2.8 Summary

My Summary.

## Chapter 3

# Tides Alone Cannot Explain Kepler Planets Close to 2:1 MMR

### 3.1 Chapter Overview

A number of *Kepler* planet pairs lie just wide of first-order mean motion resonances (MMRs). Tides have been frequently proposed to explain these pileups, but it is still an ongoing discussion. We contribute to this discussion by calculating an optimistic theoretical estimate on the minimum initial eccentricity required by *Kepler* planets to explain the current observed spacing, and compliment these calculations with N-body simulations. In particular, we investigate 27 *Kepler* systems having planets within 6% of the 2:1 MMR, and find that the initial eccentricities required to explain the observed spacings are unreasonable from simple dynamical arguments. Furthermore, our numerical simulations reveal *resonant tugging*, an effect which conspires against the migration of resonant planets away from the 2:1 MMR, requiring even higher initial eccentricities in order to explain the current *Kepler* distribution. Overall, we find that tides alone cannot explain planets close to 2:1 MMR, and additional mechanisms are required to explain these systems.

## 3.2 Introduction

The NASA *Kepler* mission has been immensely successful for detecting planets outside of our solar system. To date, it has discovered over 4,500 exoplanet candidates along with 466 multi-planet systems (Akeson et al. 2013; Rowe et al. 2014). A number of these systems are just wide of a mean motion resonance (MMR), which occurs when the period of one planet is an integer ratio of another. In particular, statistical excesses in the period distribution of *Kepler* planets have been detected just wide of the 3:2 and 2:1 MMR (Lissauer et al. 2011; Fabrycky et al. 2014; Steffen & Hwang 2015). It is believed that in the past these planetary systems migrated into resonance via convergent migration (Lee & Peale 2002), and a number of dissipative mechanisms have been proposed to slowly bring these planets out of MMR. The most popular dissipative mechanisms to explain the observed near-resonant systems are tidal (Lithwick & Wu 2012; Batygin & Morbidelli 2013; Delisle et al. 2014), protoplanetary (Rein 2012; Baruteau et al. 2013; Goldreich & Schlichting 2014), and planetesimal (Moore et al. 2013; Chatterjee & Ford 2015).

In this work we focus exclusively on tidal dissipation, for which there is no clear consensus on whether this mechanism alone can successfully explain the excess of near-resonant pairs near first order MMRs. Several authors (Lithwick & Wu 2012; Batygin & Morbidelli 2013) have argued for (Delisle et al. 2014) tidal dissipation, whereas others (Lee et al. 2013) have argued against it. In particular, Lithwick & Wu (2012) first introduced the mechanism of *resonant repulsion*, and showed that in the limit of low eccentricities for near-resonant planets, the space between planets grows as  $t^{1/3}$ . Batygin & Morbidelli (2013) confirmed this result. Lee et al. (2013) then used this relationship to show that most near-resonant planet pairs cannot be explained via this mechanism, the few exceptions being small rocky planets for which tidal dissipation is particularly effective. Delisle et al. (2014) then suggested a high eccentricity mechanism by which planets may still be able to evolve to their current

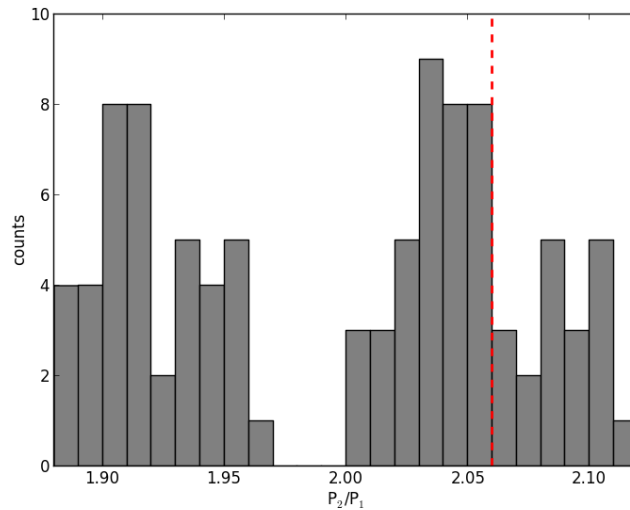


Figure 3.1: *Kepler* systems close to 2:1 MMR. A statistical excess is present just wide of the 2:1 MMR, and appears to decline beyond 6% of the resonance, as marked by a red dotted line.

positions via tides alone.

We contribute to this debate by developing optimistic theoretical estimates for the evolution of planets away from resonance, and compare these estimates to N-body simulations. We then make a statement about the likelihood of tides to explain near-resonant pairs. We focus on *Kepler* systems within 6% of the 2:1 MMR, which appears to be the natural cutoff for this statistical excess, as shown by a dotted line in Figure 3.1. Using this sample we will calculate the minimum required initial eccentricity to explain their current positions, given that they started in MMR and evolved under the influence of tides alone. In addition, we present numerical findings of *resonant tugging*, an effect which prevents the evolution of planets away from MMR when eccentricity is high, making it significantly more difficult to achieve the observed spacings seen today. Resonant tugging does not appear to have been extensively studied/accounted for in this field due to the fact that most analysis of planets in resonance have worked in the  $e \ll 1$  limit, and we find that resonant tugging exclusively affects planets in MMR with moderate to high  $e$ .

Our paper is organized as follows – in Section 3.3 we outline our theoretical and numerical framework, in Section 3.4 we present the main findings of this paper, in Section 3.5 we present a discussion and conclude in Section 4.6.

## 3.3 Methods

### 3.3.1 Theory

The equations widely used to describe the evolution of planets under the influence of tides are (e.g. Barnes et al. 2008; Lithwick & Wu 2012; Lee et al. 2013):

$$\dot{e} = -\frac{9}{2}\pi \frac{k}{Q} \frac{1}{m_p} \sqrt{\frac{GM^3}{a^3}} \left(\frac{r_p}{a}\right)^5 e \quad (3.1)$$

$$\dot{a} = -9\pi \frac{k}{Q} \frac{1}{m_p} \sqrt{\frac{GM^3}{a^3}} \left(\frac{r_p}{a}\right)^5 e^2 a, \quad (3.2)$$

where  $a$  is the semi-major axis,  $e$  is the eccentricity,  $k$  is the planet's Love number,  $Q$  is the planet's *tidal quality factor* (Goldreich & Soter 1966),  $m_p$  and  $r_p$  are the planet's mass and radius, respectively,  $M$  is the stellar mass, and  $G$  is the gravitational constant. From Eqs. 3.1 and 3.2 it follows that  $\dot{e}$  and  $\dot{a}$  are related by:

$$\frac{\dot{a}}{a} = 2e\dot{e} \quad (3.3)$$

Which arises from conservation of orbital angular momentum. We are interested in finding a relationship between the total migration of the system and its state variables (such as  $a$  and  $e$ ), which can be obtained by integrating Eq. 3.3:

$$\int_{a_f}^{a_i} \frac{da}{a} = 2 \int_{e_f}^{e_i} e de$$

$$a_f = a_i \exp(-e_i^2 + e_f^2), \quad (3.4)$$

where subscripts  $i$  and  $f$  refer to the initial and final states, respectively.

Eq. 3.4 is surprisingly simple – if we know the initial states  $e_i$  and  $a_i$  of a planetary body, as well as the final eccentricity  $e_f$ , we can predict its final position. Eq. 3.4 is

independent of tidal response parameters ( $k, Q$ ), the length of time considered, the mass and radii of the star/planet, etc. These additional factors affect the timescale by which the body arrives at its final position,  $a_f$ , but not the final position of the body itself.

Let us measure the spacing of a planet pair close to a  $j : j + 1$  MMR by defining

$$\Delta \equiv \frac{P_{out}}{P_{in}} - \frac{j+1}{j}, \quad (3.5)$$

where  $P$  is the orbital period, and the subscripts *in* and *out* refer to the inner and outer planet, respectively. For the 2:1 MMR,  $j = 1$ . This definition of  $\Delta$  is the same as Lee et al. (2013), and twice the value used by Lithwick & Wu (2012).

Using the fact that  $P \propto a^{3/2}$ , and substituting Eq. 3.4 into Eq. 3.5, we recast  $\Delta$  in terms of  $a_i$  and  $e_i$  for the near resonant pair (setting  $j = 1$ ):

$$\Delta = \left( \frac{a_{out,f}}{a_{in,f}} \right)^{3/2} - 2 \quad (3.6)$$

$$\Delta = \left( \frac{a_{out,i} \exp(-e_{out,i}^2 + e_{out,f}^2)}{a_{in,i} \exp(-e_{in,i}^2 + e_{in,f}^2)} \right)^{3/2} - 2$$

We make the assumption that  $e_{out,i} \approx e_{out,f}$  (see Section 3.5 for a discussion). After simplifying, we get:

$$\Delta = \left( \frac{a_{out,i} \exp(e_{in,i}^2 - e_{in,f}^2)}{a_{in,i}} \right)^{3/2} - 2. \quad (3.7)$$

Thus, Eq. 3.7 relates the final spacing of the system,  $\Delta$ , to the initial conditions of the system ( $a_i$  and  $e_i$ ) and the final eccentricity of the inner planet,  $e_{in,f}$ . Eq. 3.7 assumes that the angular momentum of each individual planet is conserved, which in general is not true for multi-planet systems (only total angular momentum is). Other works (Lithwick & Wu 2012; Batygin & Morbidelli 2013) have accounted for this fact, resulting in more accurate equations for the evolution of a planet pair. We now aim to compare Eq. 3.7 to numerical simulations, and estimate its accuracy for *Kepler* systems with  $\Delta < 0.06$  of the 2:1 MMR. We first outline our experimental setup.



### 3.3.2 Experimental Setup

Numerical simulations are carried out using the Wisdom & Holman integration scheme (Wisdom & Holman 1991), implemented via REBOUND (Rein & Liu 2012). Our sample consists of *Kepler* systems near the 2:1 MMR with  $\Delta < 0.06$ , which we call *near-resonant pairs*. Our choice of  $\Delta < 0.06$  stems from a natural cutoff where the excess of near-MMR ends, as shown in Figure 3.1. We exclude near-resonant pairs interior to the 2:1 MMR, since tidal forces appear only to increase planet separation with time (e.g. Lithwick & Wu 2012). In addition, we also exclude near-resonant pairs that are *complex*. By complex, we mean dynamically involved in an additional (near) resonance (e.g. Laplace resonance), and/or containing an additional planet orbiting between the near-resonant pair. Our exclusion of complex resonant systems decreases the number of *Kepler* systems by 6. Lastly, we also remove the Kepler-11 system, which does not contain a complex resonance, but does go unstable on short ( $\sim$ Myr) timescales when placed into resonance. This leaves us with 27 *Kepler* systems, and their properties are displayed in Table ???. We remind the reader that for each *Kepler* system we simulate the entire system, not just the near-resonant planets.

Many *Kepler* planets do not currently have measured mass values, so we assign planet masses using Eq. 3 from Weiss & Marcy (2014) for planets  $r_p < 4r_\oplus$ :  $(m_p/m_\oplus) = 2.69(r_p/r_\oplus)^{0.93}$ , and assume a density of Jupiter for planets  $r_p > 4r_\oplus$ . In addition, we also input mass values from the transit-timing variation study of Hadden & Lithwick (2014) where applicable. For stars without measured stellar masses, we assume  $M/M_\odot = (R/R_\odot)^{1.25}$ , derived from Demircan & Kahraman (1991). For simplicity, we also assume that the inclination of our *Kepler* planets is zero.

We assign  $k/Q$  values following a similar prescription as Lee et al. (2013) by assigning the most generous values possible. For Earth-like rocky planets,  $k/Q(r_p/r_\oplus < 2) = 1/40$ , for planets smaller than Jupiter,  $k/Q(2 < r_p/r_\oplus < 10) = 1/22000$ , and for Jupiter-sized giant gaseous planets,  $k/Q(r_p/r_\oplus > 10) = 1/54000$ .

To speed up simulation time, we increase  $k/Q$  by a factor of  $A_{k/Q}$  (or alternatively this could also be interpreted as increasing tidal strength). This tactic has been used by other scientists (e.g. Delisle et al. 2014), and is valid as long as  $\tau_e$  is much longer than the planet’s eccentricity libration time. We simulate our *Kepler* sample for 50 Myr, and use  $A_{k/Q} = 200$ , giving a total simulation time of  $T = 10$  Gyr.

To begin our simulations, we place each planet at a distance of  $1.15a_{obs}$ , where  $a_{obs}$  is the observed semi-major axis value from the *Kepler* catalog, and assign  $e_i = 0.01$ . We then migrate each planet (in a type-I fashion) back to its original starting position  $a_{obs}$  except for of the outer near-resonant planet, which instead migrates a distance of  $a_{obs} + \Delta$ , forcing the near-resonant pair into a 2:1 MMR.

Each planet migrates for time  $t_{mig}$  at rate  $\dot{a} = an\mu^{4/3}/C$ , where  $n$  is the mean motion of the inner planet,  $\mu$  is the planet/star mass ratio, and  $C$  is a constant. Lower values of  $C$  cause the outer planet to encounter the MMR sooner, allowing time for both planets to migrate together in resonance, which increases eccentricity to a desired value (Lee & Peale 2002). For the restricted 3-body problem Goldreich & Schlichting (2014) guarantee capture into resonance if  $C_{out} > 3.75$ ,  $e_{in} < (\mu_{out}/j)^{1/3}$  but we use a more conservative value of  $C_{out} = 6$  as well as perform numerical tests to ensure that overstabilities do not occur on Myr timescales.

Defining  $K \equiv \frac{\dot{e}_i/e_i}{\dot{a}_i/a_i}$ , we use a default  $K = 100$  when migrating planets into resonance but also experiment with  $K = 10$ .  $K$  (along with  $m_p/M$ ) affects the resulting equilibrium eccentricity, but does not affect tidal evolution, and thus does not affect our main conclusions. At this point, initial eccentricities of our simulated *Kepler* systems range from  $0.05 < e_i < 0.25$ , depending on the value of  $C$ ,  $K$ , etc.

After time  $t_{mig}$ , migration is quenched over a timescale of  $t_{mig}/3$  by letting  $\tau_a \rightarrow \infty$  and  $\tau_e \rightarrow \infty$ , where  $\tau_a \equiv -a/\dot{a}$  and  $\tau_e \equiv -e/\dot{e}$ . It is at this point that tides are turned on, and the system evolves under the influence of Eq. 3.1 and 3.2 for the remainder of the simulation.

## 3.4 Results

### 3.4.1 Theory vs. Numerics

We compare our theoretical predictions of tidal evolution,  $\Delta_{th}$  (Eq. 3.7), to our numerical simulations,  $\Delta_{num}$  (Eq. 3.6). The difference,  $\Delta_{num} - \Delta_{th}$ , is displayed as a solid line in Figure 3.2, and expressed as a cumulative distribution (CDF). For all but 2 systems we see that  $\Delta_{num} - \Delta_{th} < 0$ , indicating that our theoretical predictions  $\Delta_{th}$  consistently over-predict our numerical results,  $\Delta_{num}$ . These 2 exceptions, Kepler-32 and Kepler-221, are expected due to the fact that  $T/\tau_e \sim 1000$ , which allows extensive  $\Delta \propto t^{1/3}$  resonant repulsion growth (Lithwick & Wu 2012) in time  $T$  which is not accounted for in Eq. 3.7. Otherwise, we find that Eq. 3.7 consistently overestimates the true evolution of the system.

The reason for this  $\Delta_{num} - \Delta_{th} < 0$  trend is due to *resonant tugging*, an effect present in the numerics but not captured by our theoretical predictions. Resonant tugging acts to keep planets closer together than theory would predict. We explore resonant tugging in the next section.

For the same simulations we also plot  $\Delta_{num} - \Delta_{obs}$  as a dashed line in Figure 3.2, which is the difference between our numerical results,  $\Delta_{num}$ , and the observed spacing of *Kepler* planets seen today,  $\Delta_{obs}$  (Eq. 3.5). As is clearly shown,  $\Delta_{num} - \Delta_{obs} < 0$  for all but two systems, suggesting that tides alone cannot explain the observed spacing of *Kepler* planets. These two exceptions are again, Kepler-32 and Kepler-221, and are exceptions for the same reason as above. Since  $\Delta_{obs} = 0.038$  and  $0.035$  for Kepler-32 and Kepler-221, respectively, using a lower  $\Delta$  cutoff for our *Kepler* sample (e.g.  $\Delta_{obs} < 0.03$ ) would not have changed our result that tides cannot explain near-resonant pairs.

Although highly suggestive, this result does not conclusively disprove tides as the primary evolving mechanism, since higher  $e_i$  could cause more migration in time  $T$

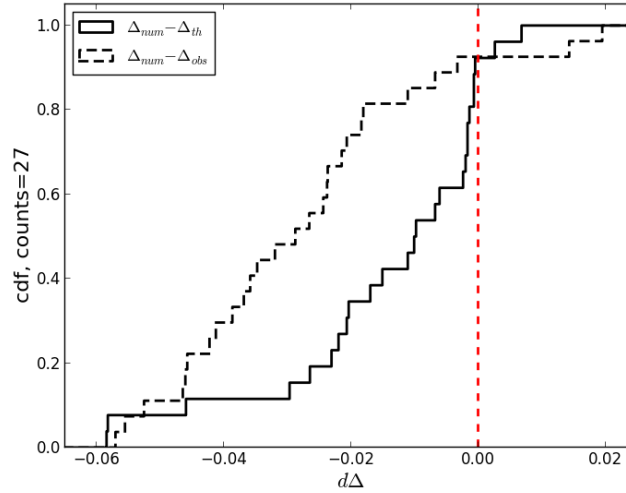


Figure 3.2: Cumulative distribution function (CDF) of our results. The solid line shows  $\Delta_{num} - \Delta_{th}$ , the difference between the theoretical and simulated planet separations after  $T = 10$  Gyr. The dashed line shows  $\Delta_{num} - \Delta_{obs}$ , the difference between our numerical simulations and the observed *Kepler* spacing.

(see Eq. 3.4), and the median eccentricity for our simulations is  $e_{in,i} = 0.14$ . Higher values of  $e_{in,i}$  are possible. Instead of numerically exploring every possible  $e_{in,i}$  value, however, we instead reverse the argument in Section 3.4.3 and calculate the minimum  $e_{in,i}$  required to explain  $\Delta_{obs}$ . First, however, we explore resonant tugging.

### 3.4.2 Resonant Tugging

*Resonant tugging* affects planets in MMR subjected to energy dissipation (e.g. tidal), with moderate to high eccentricity. When these conditions are met and the inner planet migrates inwards (trying to leave the resonance) it tugs the outer planet inwards along with it, transferring dissipative forces from the inner to the outer planet. The result is that the inner planet migrates less than expected, the outer planet migrates more than expected, and the planets are closer together than theory would have predicted.

Figure 3.3 illustrates resonant tugging for a pair of  $m = 10^{-4}M$  planets in MMR. For the black curve  $e_{in,i} = 0.125$ , for the grey curve  $e_{in,i} = 0.018$ , and otherwise the

initial conditions of each test case are the same. In both cases we allow *only the inner planet* to evolve under the influence of tides. The top and bottom panels show the period evolution of the outer and inner planets, respectively, and the dotted curve in the bottom panel shows evolution of the inner planet in the absence of the outer planet (also  $e_{in,i} = 0.125$ ).

Resonant tugging is exhibited in the first 0.5 Gyr of evolution for the black curve, showing how tidal forces affecting the inner planet also affect the outer planet by dragging it inwards too. Comparing the solid and dotted black curves in the bottom panel of Figure 3.3, we see that in the presence of the outer planet, the inner planet migrates much less than expected due to resonant tugging. Since the outer planet has also migrated inwards more than expected, the result is that  $\Delta_{black}$  has grown very little over the first 0.5 Gyr of evolution ( $\Delta_{black} = 0.004$  after 0.5 Gyr).

Within the framework of resonant tugging, the outer planet can be thought of as a massive anchor – as  $m_{out}/m_{in} \rightarrow \infty$  the inner planet has an increasingly difficult time migrating both bodies inwards, leading to a pair of (relatively) stationary planets. Conversely, as  $m_{out}/m_{in} \rightarrow 0$  the inner planet has an easier time migrating both bodies inwards, and the trajectory of the inner planet will approach its single-planet trajectory (i.e. the dotted black line in Figure 3.3).

We now briefly contrast resonant tugging from resonant repulsion (first described by Lithwick & Wu 2012). Qualitatively, the two main differences between resonant tugging and resonant repulsion are:

1. Resonant tugging exclusively affects planets in resonance (resonant angle(s) librating) with moderate to high eccentricity, while resonant repulsion affects planets both in and close to resonance, and is most noticeable in the  $e \ll 1$  limit.
2. Resonant tugging decreases  $a_{in}$  and decreases  $a_{out}$ , while resonant repulsion decreases  $a_{in}$  and increases  $a_{out}$ .

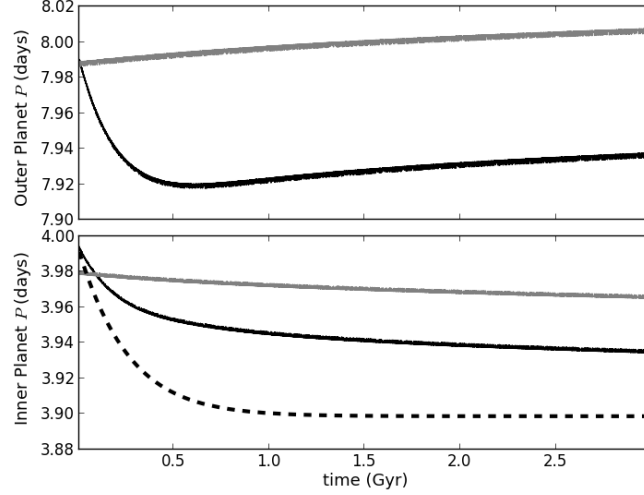


Figure 3.3: Two test cases illustrating resonant tugging and repulsion. The top and bottom panel shows the period evolution of the inner and outer planet, respectively. For the black curve  $e_{in,i} = 0.125$ , while for the grey curve  $e_{in,i} = 0.018$ . The dotted black curve shows the numerical trajectory of the inner planet ( $e_{in,i} = 0.125$ ) in the absence of the outer planet.

These two differences are illustrated in Figure 3.3. The grey curve, which has low initial eccentricity ( $e_{in,i} = 0.018$ ) exhibits pure resonant repulsion – a decrease in  $a_{in}$  and an increase in  $a_{out}$ , while the black curve first exhibits a shorter period of resonant tugging followed by resonant repulsion. The transition from resonant tugging to resonant repulsion for the black curve occurs after 0.5 Gyr, when the eccentricity of the inner planet has dropped to a low ( $e_{in} = 0.035$ ) value.

In Figure 3.3, after  $\sim 1$  Gyr,  $\Delta_{black} < \Delta_{grey}$ , but  $\dot{\Delta}_{grey} = \dot{\Delta}_{black}$ , showing how resonant tugging can permanently stunt the growth of  $\Delta$ . We also see for the black curve that  $a_{out,f} < a_{out,i}$ , and it is only after many  $\tau_e$  timescales that the outer planet can recover (or exceed) its initial position via resonant repulsion. Furthermore, since to first order (when  $T/\tau_e \ll 1000$ )  $\dot{\Delta} \propto \tau_{a,in} \propto e_{in,i}^2$  one would naively expect the black curve to experience  $e^2$  more  $\Delta$  growth in time  $T$ , yet we actually find  $\Delta_{black} < \Delta_{grey}$ , illustrating just how significant resonant tugging can be. This means that the high eccentricity tidal mechanism suggested by Delisle et al. (2014) does not work for

planets in resonance, since (contrary to expectation) high eccentricity actually stunts the growth of  $\Delta$ , not accelerates it.

The results shown in Fig. 3.2 are due to resonant tugging, and is supported by the fact that for every simulated *Kepler* system we find  $a_{out,f}/a_{out,i} < 1$ . Since resonant repulsion can only increase  $a_{out}$  (as shown in Fig. 3.3),  $a_{out,f}/a_{out,i} < 1$  can only be due to resonant tugging since inward tidal migration is a negligible contribution for the outer planet. The analytic aspects of resonant tugging will be studied in more depth in future works.

### 3.4.3 Minimum Eccentricity to Explain $\Delta_{obs}$

Since we found in Section 3.4.1 that  $\Delta_{th}$  consistently over-predicts the amount of tidal migration (due to resonant tugging), we can use it as an upper limit predictor of tidal evolution, assuming that near-resonant pairs started in 2:1 MMR and evolved to their present locations. Starting from Eq. 3.3, and using the same logic as Section 3.4.1 we calculate the minimum eccentricity required by the inner planet to achieve the observed spacing seen today,  $\Delta_{obs}$ , after  $T$  years (see Appendix ?? for detailed calculations):

$$e_{in,i} = \sqrt{\frac{\ln[(\frac{a_i}{a_f})_{out}(\frac{\Delta_{obs}+2}{2})^{2/3}]}{1 - \exp(-2T/\tau_{e,in})}} \quad (3.8)$$

Thus, for a pair of planets starting in 2:1 MMR, if we know the observed spacing today,  $\Delta_{obs}$ , the number of  $\tau_{e,in}$  damping timescales in time  $T$ , and estimate the amount of migration done by the outer planet in time  $T$ ,  $(a_i/a_f)_{out}$ , we can calculate the *minimum* initial eccentricity that the inner planet must have in order to arrive at the current spacing,  $e_{in,i}$ . Since we assume a starting position of exact 2:1 commensurability, Equation 3.8 is only tailored for  $\Delta_{obs} > 0$ . Tides cannot decrease planet spacing over time.

Figure 3.4 shows CDFs of Eq. 3.8 applied to our *Kepler* sample for  $T = 1$  (solid), 5 (dashed), and 10 (dotted) Gyr with the outer planet remaining stationary, i.e.

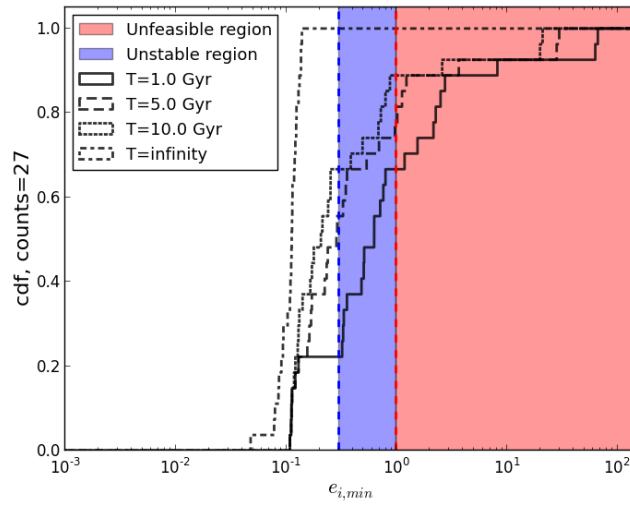


Figure 3.4: Three CDFs showing the theoretical minimum eccentricity required by the inner planet in order to achieve the observed  $\Delta$  spacing seen by *Kepler* planets today. The solid, dashed, dotted lines represent  $T = 1, 5, 10$  Gyr tracks, respectively, while the dash-dotted line represents  $T \rightarrow \infty$ . In all calculations we assume the outer planet remains stationary, i.e.  $(a_i/a_f)_{out} = 1$ . The red shaded region marks the unphysical region where the eccentricity is larger than unity. The blue region marks the region where most systems undergo a dynamical instability.



$(a_i/a_f)_{out} = 1$  (see Section 3.5 for a discussion). In addition we plot a  $T \rightarrow \infty$  curve as a dash-dotted line, which the other curves converge to. The shaded red region marks where  $e_{in,i} \geq 1.0$ , while the blue marks an unstable region where eccentricities are unlikely to exist. We construct the blue region by numerically finding the maximum eccentricity allowed before  $> 50\%$  of our *Kepler* systems go unstable within 2 Myr (see Appendix ?? for details). We find this maximum eccentricity to be  $\approx 0.3$  (the left boundary of the blue shaded region in Figure 3.4).

The three  $T < \infty$  curves in Figure 3.4 lie largely in the red and blue shaded regions, indicating that the required eccentricities to explain  $\Delta_{obs}$  are unreasonable. We thus conclude that most *Kepler* systems cannot be explained by tides alone. Even for the  $T = 10$  Gyr curve, an optimistic estimate for the age of many *Kepler* systems, about 35% of systems still cannot be explained due to tides alone. Clearly, another mechanism is needed to explain the near-resonant 2:1 MMR pairs.

### 3.5 Discussion

A number of assumptions have been made in constructing Figure 3.4 which only strengthen our conclusion that planets close to the 2:1 MMR cannot be explained due to tides alone.

First and foremost, from Sections 3.4.1 and 3.4.2 we have shown that resonant tugging causes our theoretical predictions of  $\Delta$  to be overestimates, and thus Eq. 3.8 underestimates the minimum  $e_{in,i}$  required to explain the current observed spacing. This discrepancy becomes most pronounced when  $m_{out}/m_{in} > 1$ , which is the case for many *Kepler* systems in our sample. In particular we showed that resonant tugging can stunt the evolution of planets away from MMR by roughly  $e^2$  (see Sec 3.4.2), and this stunted evolution is not accounted for in Figure 3.4.

Second, we have assumed optimistic  $k/Q$  values which allow for more migration in time  $T$ . Although *some* planets could have such generous values, it is unlikely that

all of them do. Since  $\dot{a} \propto (k/Q)e^2$ , as  $k/Q$  decreases  $e_{in,i}$  must increase in order for the planets to achieve the same observed  $\Delta$  in time  $T$ .

Third, our estimate of  $e_{max} = 0.3$  (blue-shaded region in Figure 3.4) is very likely an overestimate. For example, Pu & Wu (2015) found that the mean eccentricity of high-multiple Kepler planets must not exceed  $e_{mean} = 0.02$  to guarantee long-term dynamical stability. Also, from simple orbit crossing arguments when  $e > 0.23$  the perihelion of the outer planet crosses the aphelion of the inner planet for a 2:1 MMR, and long-term stability can no longer be guaranteed. Even if it were possible for *Kepler* systems to remain stable with high ( $> 0.3$ ) eccentricities, it is unclear what kind of mechanism could consistently generate them for our *Kepler* sample.

There are other assumptions we made throughout this paper which we now justify. For the results presented in Fig. 3.4 we assumed that the outer planet remains stationary, i.e.  $(a_i/a_f)_{out} = 1.00$ . This is a reasonable assumption since, referring to our  $T = 10$  Gyr numerical simulations as a benchmark, the median value of  $(a_i/a_f)_{out} = 1.001 \approx 1$ . Increasing the value of  $(a_i/a_f)_{out}$  shifts our CDFs in Fig. 3.4 further into the blue/red instability region.

In Eq. 3.7 we assumed that  $e_{out,i} \approx e_{out,f}$  which essentially states that the initial and final positions of the outer planet are the same. As stated in the previous paragraph, since we found numerically from our simulations that the median  $(a_i/a_f)_{out} \approx 1$ , this assumption is reasonable.

In constructing Fig. 3.4 we have used Eq. 3.8, which is Eq. 89 from Delisle et al. (2014), who argued that for moderate to high eccentricities ( $e_{in,i} \geq 0.15$ ), many of the near-resonant pairs could in fact be explained by tides. There are a number of differences between our analysis and theirs however. First (and most importantly), their estimates are based on theoretical predictions (i.e. resonant tugging unaccounted for), and we have shown in Section 3.4.2 that the growth of  $\Delta$  is significantly stunted when resonant tugging is accounted for, especially when  $m_{out}/m_{in} > 1$ . Second, their

analysis assumes that  $T \rightarrow \infty$ , while we restrict to  $T = 1, 5$  and 10 Gyr. Looking at Fig 3.4, we see that the  $T \rightarrow \infty$  curve tells a very different story than the  $T = 1, 5$  and 10 Gyr curves, and the conclusion of whether or not tides can explain  $\Delta_{obs}$  is certainly time dependent. Lastly, Delisle et al. assumes  $\Delta = 0.03$  for all systems, while we use the system specific  $\Delta$  values.

As a consistency check for our results, we perform the same set of experiments (including our tests of resonant tugging) using a different version of tides, implementing them in terms of forces (as opposed to orbital elements like in Eq. 3.1 and 3.2) according to Papaloizou & Larwood (2000):

$$\vec{a}_{damp} = -2 \frac{(\vec{v} \cdot \vec{r})\vec{r}}{r^2 \tau_e} \quad (3.9)$$

where  $\vec{a}_{damp}$  is the damping acceleration,  $\vec{v}$  is the velocity,  $\vec{r}$  is the position,  $r$  is the scalar position and  $\tau_e \equiv -e/\dot{e}$  as before. Whenever a planet receives a “kick” in the WH integration scheme, an additional kick of  $a_{damp}$  is supplied to account for tides. We find our overall conclusions unaffected using this implementation of tides.

We have omitted complex resonances from our analysis because their behaviour is much more unpredictable. For simple resonances we found that  $\Delta_{th} > \Delta_{num}$ , but some complex resonances violated this relationship. The reasons are currently unknown, but will be more thoroughly investigated in future works.

Lastly, it should be mentioned that spin tides were omitted from this analysis, which arise when the spin rate of the host star  $\Omega_*$  is different than the mean motion  $n$  of the orbiting planet (responsible for the Moon’s recession from Earth over time). Spin rates of *Kepler* stars are largely unknown, as well as the evolution of these spin rates,  $d\Omega_*/dt$ . Depending on the sign of  $(\Omega_* - n)$ , spin tides can induce inward or outward migration. It is thus a non-trivial process to determine what the affect of spin tides might be on the evolution of a system. The equation governing spin tide

migration is (Murray & Dermott 1999):

$$\dot{a}_p = \text{sign}(\Omega_* - n_p) \frac{3k_*}{Q_*} \frac{m_p}{M} \left( \frac{R}{a_p} \right)^5 n_p a_p \quad (3.10)$$

where the subscripts  $p$  and  $*$  refer to the planet and star, respectively. We can estimate the relative strength of eccentricity tides (Eq. 3.2) to spin tides (Eq. 3.10):

$$\frac{\dot{a}_{ecc}}{\dot{a}_{spin}} = \frac{9\pi \frac{k_p}{Q_p} \sqrt{\frac{GM^3}{a_p^3}} \frac{e_p^2 a_p}{m_p}}{3 \frac{k_*}{Q_*} \frac{m_p}{M} \left( \frac{R}{a_p} \right)^5 n_p a_p} = 3\pi \frac{k_p}{k_*} \frac{Q_*}{Q_p} \left( \frac{M}{m_p} \right)^2 \left( \frac{r_p}{R} \right)^5 e^2$$

Interestingly enough, the relative strength of spin vs. eccentricity tides is independent of the semi-major axis. Assigning typical values from Wu & Murray (2003) for  $\Omega_*$ ,  $(k/Q)_*$ ,  $M$  and  $R$ , and assuming a typical  $\sim 4m_\oplus$  planet we get:

$$\frac{\dot{a}_{ecc}}{\dot{a}_{spin}} \sim 30 \quad (3.11)$$

Combining this with the fact that  $\Omega_*$  and  $d\Omega_*/dt$  are largely unknown for *Kepler* stars, we felt justified omitting spin tides from our analysis.

## 3.6 Conclusion

In conclusion, we have investigated 27 *Kepler* systems containing 2:1 near-resonant pairs, and find that tides alone cannot explain their current observed spacing,  $\Delta_{obs}$ . In Figure 3.4 we calculated the minimum theoretical eccentricity required by the inner planet to explain  $\Delta_{obs}$  and found that for a large number of systems  $e_{in,i} > 0.3$ , which from simple dynamical arguments is not a reasonable eccentricity for *Kepler* planets to have. Furthermore, our numerical study of resonant tugging reveals that our theoretical predictions of  $e_{in,i}$  are optimistic estimates, and in cases where  $m_{out}/m_{in} > 1$ , significantly so. A number of other assumptions made throughout the paper contribute to these optimistic estimates.

As a numerical compliment to our theoretical investigation, we simulated our *Kepler* sample for 10 Gyr with a median eccentricity of  $e_{in,i} = 0.14$ , and found only two systems, Kepler-32 and Kepler-221, that migrated to  $\Delta_{obs}$  (dotted line in Figure 3.2). Clearly, another mechanism is required to explain the excess of *Kepler* systems exterior to the 2:1 MMR.

### 3.7 Summary

My Summary.

# Chapter 4

## HERMES: a hybrid integrator for simulating close encounters and planetesimal migration

### 4.1 Chapter Overview

We present HERMES, a new hybrid integration scheme for long-term simulations of planetary systems undergoing close encounters or planetesimal-driven migration. Particles are integrated using WHFAST, a fast and accurate symplectic integrator, unless a close encounter occurs. During a close encounter, a subset of particles is integrated with the high-order integrator IAS15, while the rest of the particles continue to be integrated with WHFAST. We created an adaptive routine for optimizing the close encounter boundary to help maintain accuracy whilst close encounters are occurring.

AS[Like most hybrid integrators, ] the switching between integrators leads to AS[an additional,] finite energy error AS[above the standard oscillatory energy error arising from symplectic integration] . HERMES takes a more direct approach when switching between integrators than previous schemes in the literature, allowing us to analytically estimate the numerical error of our algorithm. Since WHFAST is

symplectic, IAS15 is accurate to machine precision and both of them are unbiased, the energy error grows sub-linearly with time under the assumption that either impact parameters are randomly distributed or close encounters are rare.

We find that HERMES provides a good balance between speed and accuracy, neither achieved by the individual symplectic or non-symplectic integrators alone. In this paper, we describe the details of implementation, accuracy and performance, as well as its incorporation within the larger framework of the  $N$ -body package REBOUND.

## 4.2 Introduction

Over the last 25 years scientists have made considerable progress integrating  $N$  gravitationally interacting particles (an  $N$ -body system) using computational techniques. The most widely used integrator today for solving Solar System type problems is the Wisdom-Holman integrator (Wisdom & Holman 1991, hereafter WH), which decomposes the system's Hamiltonian,  $H$ , into a Keplerian and an interaction component,  $H_K$  and  $H_I$ . Symplectic integrators which split the Hamiltonian in this way are known as mixed-variable symplectic integrators (Wisdom & Holman 1991; Saha & Tremaine 1992). The system is then evolved in a second-order leapfrog manner, taking the form of  $K(dt/2)I(dt)K(dt/2)$ , where  $K$  represents evolution under  $H_K$ ,  $I$  represents evolution under  $H_I$ , and  $dt$  is the timestep. Although higher-order algorithms are possible (e.g. Yoshida 1990), the second-order WH method is **AS[an ideal balance of speed and accuracy]** since the **AS[marginal]** increase in accuracy of higher-order methods comes at the cost of **AS[significant]** additional calculation. The evolution under the interaction Hamiltonian is trivial to solve exactly in Cartesian coordinates, whereas the evolution under the Keplerian Hamiltonian is easy to solve exactly using orbital elements. This algorithm therefore converts between the two coordinate systems each timestep.

Since the WH scheme breaks the evolution into operators that both derive from Hamiltonians, the algorithm is symplectic (for a review on symplectic algorithms see Yoshida (1993)). This implies that the numerical solution conserves quantities closely related to the integrals of motion, such as the total energy. **AS[In practice these integrals of motion are not constant, but oscillate in a bounded manner.]** The relative energy error scales as  $O(\epsilon dt^2)$  if the magnitude of  $H_I$  remains  $O(\epsilon)$  smaller than  $H_K$ , where  $\epsilon \ll 1$  (Saha & Tremaine 1994). For distant particles in non-overlapping orbits  $\epsilon$  is typically much less than unity. This is one motivation for splitting  $H$  into  $H_K$  and  $H_I$ , as it allows for longer timesteps (and thus shorter integration times) than conventional integration schemes. However, during close encounters,  $H_I$  becomes comparable to or larger than  $H_K$  causing  $\epsilon$ , and thus the energy error, to grow substantially. Therefore, despite their brief duration, close encounters typically dictate an unacceptably short timestep for the entire simulation. Note that it is not possible to dynamically change the timestep in the standard WH integrator as it would break time symmetry and symplecticity<sup>1</sup>.

For very high accuracy integrations (with relative errors of order the machine precision), non-symplectic integrators are as good and as fast as or faster than symplectic integrators (Rein & Spiegel 2015). But in most integrations, medium to low accuracy is enough to capture the qualitative evolution of a system. In such a case a symplectic integrator provides an advantage as the timestep can be large while keeping the numerical errors bounded. This advantage of symplectic integrators, together with the common need to accurately resolve close encounters motivates the development of hybrid integrators that can make use of both symplectic and non-symplectic integrators.

Several hybrid integrators that make use of a (modified) WH integrator have

---

<sup>1</sup>If one can make the timestep choice independent of the current state, for example by using a predefined sequence of timesteps, then the integrator remains symplectic.



been developed. The two most popular ones are SyMBA (Duncan et al. 1998) and the hybrid integrator from the Mercury package (Chambers 1999, hereafter referred to as Mercury).

SyMBA decomposes the interaction potential into a series of shells around each body and uses progressively smaller timesteps for each shell to increase time resolution. If the particles are well separated, there is only one contributing shell to the interaction term and the integrator is effectively WH. During a close encounter the inner shells contribute to the integration using smaller timesteps to resolve the encounter.

Mercury handles close encounters by using a smooth changeover function to transfer large terms from  $H_I$  to  $H_K$ . When particles are distant, interactive forces between particles are small and evaluated during  $H_I$ . When particles are close, interactive forces become large and are transferred to  $H_K$ , thus keeping  $H_I$  small. This makes  $H_K$  a three body problem (central body plus two particles undergoing a close encounter) which cannot be solved analytically but is straightforward to integrate numerically to high precision using a Bulirsch-Stoer routine (Press et al. 1988).

In this paper we present a new integration method, HERMES, which borrows ideas from the integrators mentioned above, but takes a more direct approach to handling close encounters. It combines two existing integrators, WHFAST (Rein & Tamayo 2015) which is a fast and unbiased implementation of the WH method, and the high-order IAS15 integrator (Rein & Spiegel 2015). HERMES has been seamlessly incorporated into REBOUND (Rein & Liu 2012), adding further flexibility to the modular  $N$ -body package.

The outline for the paper is as follows: Section 4.3 describes the algorithm for HERMES, Section 4.4 characterizes error, Section 4.5 shows standard tests of HERMES as well as a comparison to SyMBA and Mercury, and we conclude in Section 4.6.

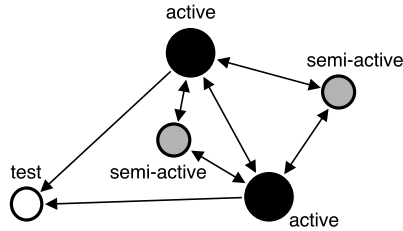


Figure 4.1: A diagram illustrating how different particle types (active, semi-active, test) affect each other. Arrows indicate directions of gravitational influence.

## 4.3 Methods

### 4.3.1 Particle Classification

First we define the three different types of particles handled by HERMES: active particles, semi-active particles and test particles. Active particles can gravitationally affect all other types of particles, and are typically stars or planets. Semi-active particles can affect active particles only (not other semi-active particles), and are typically asteroids, planetesimals, and other smaller objects. Test particles are only affected by active particles and cannot affect any other particle, and are typically dust grains, rocks, small asteroids or spacecrafts. Figure 4.1 summarizes these interactions, where arrows represent directions of gravitational influence.

### 4.3.2 Heliocentric version of WHFAST

The original WHFAST algorithm described in Rein & Tamayo (2015) was implemented in Jacobi coordinates. Jacobi coordinates lead to a better precision compared to heliocentric coordinates if orbits are well separated and do not cross each other. If close encounter occur, then heliocentric coordinates can help improve the integrator’s accuracy. For that reason we implemented a heliocentric version of WHFAST in REBOUND. We call it WHFastHelio. We use it as the symplectic integrator in HERMES but note that WHFastHelio can also be used by itself. We choose the specific splitting of the

Hamiltonian by Duncan et al. (1998) and Chambers (1999). For a discussion on the different splittings, their advantages and disadvantages, see Wisdom (2006). For the remainder of this paper we will refer to WHFastHelio simply as WHFAST as both integrators use the same Kepler solver.

### 4.3.3 Algorithm

The HERMES integrator is composed of two parts, a *global* simulation which contains all particles, and a *mini* simulation which contains all active particles plus any semi-active or test particles involved in a close encounter. The global simulation is integrated using WHFAST, while the mini simulation is integrated using IAS15. We first outline the overall algorithm for one timestep<sup>2</sup> of length  $dt$  and then describe the individual steps in more detail.

To evolve the system for a single timestep HERMES performs the following steps:

1. **Check for close encounters.** If any particle (active, semi-active, or test) has a close encounter with an active particle, then copy the particles involved in the close encounter plus all active particles to the mini simulation.
2. **Integrate the global simulation** using the WHFAST integrator for one timestep,  $dt$ .
3. **Integrate the mini simulation** using the IAS15 integrator if a close encounter AS[was identified in step 1.]
4. **Update the particles in the global simulation** AS[using the mini simulation] if the mini simulation was active this timestep.

Although the algorithm is simple to write down in the above form, there are several caveats to point out. For all particles excluding the central body, we define

---

<sup>2</sup>We refer to the timestep that WHFAST takes as  $dt$ . The IAS15 integrator chooses its own timestep which is typically smaller than  $dt$ .

the parameter  $f_H$ , which we dub the Hill Switch Factor. A spherical shell is of radius  $f_H r_H$  is constructed around each body, **AS[ where  $r_H$  is the Hill radius and defines the region surrounding each body where its local gravity dominates that of central body. If the shells of any two particles overlap it is deemed a close encounter.]** Since all semi-active and test particles are invisible to each other they cannot be involved in close encounters with one another. Only particles that gravitationally interact with each other can participate in close encounters (see Fig. 4.1). Whenever there is at least one close-encounter the mini simulation is integrated, if no close-encounters occur, the mini simulation is not active and the integrator defaults to WHFAST. Since the central object has no Hill sphere this motivates us to define the Solar Switch Factor,  $f_\odot$ , which only applies to the central body. Like  $f_H$  it also defines a spherical shell except is in units of the central object's physical radius instead of Hill radii. **AS[Therefore, when a body passes within  $f_\odot r_\odot$  of the central object it is deemed a close encounter, where  $r_\odot$  is the radius of the central object.]**

During a close encounter, WHFAST still integrates all particles (including those involved in the close encounter) leading to momentarily large errors for the particles involved in the close encounter. One might expect that this poses a real problem for the accuracy, but that is not the case, since all particles involved in the close encounter plus all active particles are overwritten at the end of the timestep using the accurate results from the mini simulation.

Unlike the global simulation, the mini simulation may take many timesteps to get from  $t$  to  $t + dt$ . The length of the timestep in the mini simulation is automatically determined by the IAS15 integrator. During each sub-timestep the mini simulation also checks for physical collisions between overlapping particles.

As an example of how the mini and global simulations integrate through time, consider a 2 planet, 2 planetesimal system. The planets are active particles and the planetesimals are semi-active particles. Figure 4.2 shows the distance of the

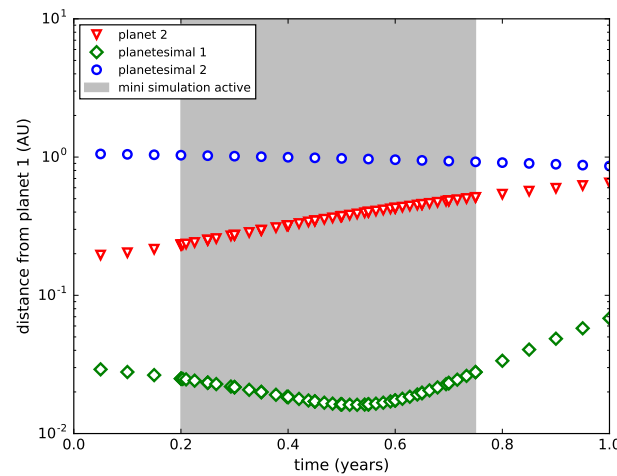


Figure 4.2: A short simulation displaying the HERMES integrator for a 2 planet, 2 planetesimal system orbiting a central star. When active, the mini simulation takes many sub-timesteps for each  $dt$  and integrates planets 1, 2 and planetesimal 1 during the close encounter between planet 1 and planetesimal 1.

planetesimals and planet 2 from planet 1 as a function of time. A point is plotted after every timestep in both the global and mini simulation. After 0.2 years, planetesimal 1 (a semi-active body) has a close encounter with planet 1 (an active body). At that time, the mini simulation is turned on and planetesimal 1, planet 1 the central star (not shown) and planet 2 are added to the mini simulation and integrated until 0.75 years, at which point the close encounter between planetesimal 1 and planet 1 is complete. Planetesimal 2 on the other hand continues to be solely integrated by the global simulation (using WHFAST) throughout the close encounter. By comparing the outputs of planetesimal 2 and the other particles in Fig. 4.2, one can see that the mini simulation takes numerous sub-timesteps compared to the global simulation. Since IAS15 is an adaptive method, it automatically chooses the appropriate timestep to resolve the close encounter with machine precision accuracy.

**AS[We briefly discuss the speed of the algorithm.]** If no particles are integrated with IAS15, then the speed is effectively that of WHFAST with a small overhead due to

collision checks. If all particles are integrated with IAS15, then the speed is that of a simulation running only IAS15, again with a small and in general negligible overhead due to collision checks. Consider a typical simulation of multiple active particles undergoing planetesimal migration from a large number of semi-active particles with a reasonable  $f_H$  value. As the number of semi-active particles is increased, the ratio of the number of particles in the mini simulation,  $N_{\text{mini}}$ , to the number of particles in the global simulation,  $N_{\text{global}}$ , approaches a constant. In this limit the elapsed simulation time is linearly proportional to the number of semi-active particles in the simulation.

#### 4.3.4 Perturbative Forces in the Mini Simulation

One must carefully treat the forces perturbing the motions of active particles in the mini simulation. In the global simulation, active particles receive perturbative kicks from all semi-active particles, and it is important to reproduce these forces in the mini simulation, which only evolve a subset of particles. To further complicate this issue, the mini simulation takes numerous sub-timesteps for each global timestep. In HERMES, we linearly interpolate the forces of all semi-active particles absent from the mini simulation using the initial and final values from the global simulation. We find that interpolating the forces (rather than positions) leads to a significant speed gain without compromising noticeable accuracy.

One could argue that this process should be iterated – the active particles will arrive at slightly different (and more accurate) final positions when integrated with the mini simulation, and thus the perturbative forces they would have induced on the semi-active particles in the global simulation would be slightly different too. Thus if one wanted to improve the accuracy of the algorithm an iterative process could be constructed where the global and mini simulations take turns integrating for a timestep  $dt$  making use of the updated positions from the previous iteration.

However, as long as the semi-active particles have a much smaller mass than the

active particles, we have found that this iterative process is unnecessary, allowing us to reduce both the computation time and algorithmic complexity. We note that in our current non-iterative scheme, interpolating the forces between pairs of *active* particles introduces non-negligible numerical errors. For that reason, all active particles are automatically added to the mini simulation during any close encounter, even if they are not involved in the close encounter themselves.

### 4.3.5 Adaptive $f_H$ Algorithm

$f_H$  and  $dt$  are the most important parameters to consider when simulating a system with HERMES. For a system free of close encounters,  $dt$  alone determines the precision of the algorithm. However during close encounters  $f_H$  and  $dt$  together determine the algorithm's precision (see Section 4.4). Specifically, if a particle moves a distance  $\sim f_H r_H$  per timestep  $dt$  the algorithm could miss a close encounter, introducing large errors into the simulation. In addition, an initial choice of  $f_H$  and  $dt$  can become non-optimal if a system evolves significantly from its initial state.

To aid the user in making the correct parameter choices, we have developed a simple algorithm that, given a timestep  $dt$ , conservatively estimates the smallest value of  $f_H$  under the condition that no close encounter is missed. Although  $f_H$  and  $dt$  both determine the precision of HERMES during a close encounter, we only optimize  $f_H$  since constantly changing  $dt$  would result in non-negligible numerical errors for a symplectic integrator like WHFAST. We calculate the optimal  $f_H$  each iteration, ensuring that  $f_H$  adapts to an evolving system and guarantees that close encounters are continuously resolved. The user is therefore only required to set the timestep  $dt$  for a standard integration ( $f_\odot$  is set to a default value serving most purposes). The full algorithm works as follows.

For each body, we ignore the inclination, and marginalize over the phase and longitude of periapsis from 0 to  $2\pi$ . As illustrated in Figure 4.3, this smears out the

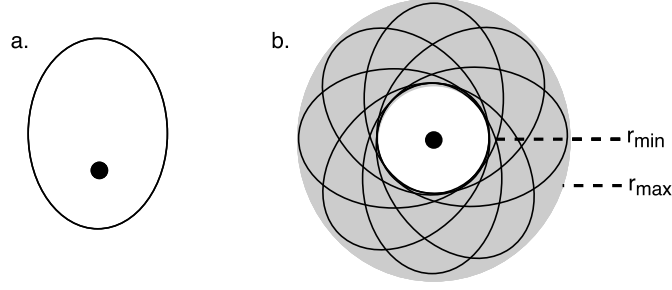


Figure 4.3: Panel a. shows a regular orbit in 2D, while panel b. shows the construction of a ring by rotating the orbit's pericenter by  $2\pi$ .

orbit into a ring in the reference plane. Each ring has a maximum and minimum distance from the central object,  $r_{\min}$  and  $r_{\max}$ . We then check if any two interacting particles can possibly have a close encounter by comparing their  $r_{\min}$  and  $r_{\max}$  values. If an intersection of two rings occurs, say for particles  $i$  and  $j$ , we calculate their maximum relative velocity  $\Delta v_{ij,\max}$  in the overlapping interval between the two particles. We calculate  $\Delta v_{ij,\max}$  as a simple overestimate rather than the true maximum in order to speed up the calculation. As a result of ignoring the inclination and marginalizing over the phase and longitude of periastron,  $\Delta v_{\max}$  can be calculated from just the semi-major axis and the eccentricity. We note that we do not need to solve Kepler's equation in estimating  $\Delta v_{\max}$ .

We can then calculate  $f_H$  by taking the maximum over all interacting particle pairs (see Fig 4.1),

$$f_H = 4 \max_{i,j} \frac{\Delta v_{ij,\max} dt}{r_{H,i} + r_{H,j}}.$$

The numerical constant 4 ensures that two particles move at most one quarter of  $f_H(r_{H,i} + r_{H,j})$  in one timestep and therefore no close encounters are missed.

In practice, we also round up  $f_H$  to the nearest  $1.25^x$  where  $x$  is an integer to avoid continuous fluctuations in  $f_H$ . By default, our adaptive  $f_H$  algorithm is enabled in HERMES. Since the algorithm assumes particles move on approximately coplanar orbits, it may therefore fail at very high mutual inclinations. We note that the above



algorithm chooses the smallest value of  $f_H$  that captures all close encounters; however, small values of  $f_H$  introduce numerical errors when switching between integrators (see Section 4.4). Therefore, to avoid large errors we set a default lower limit of  $f_H = 3$ , which is close to the default close encounter boundary for Mercury and SyMBA. The user can specify their own lower limit for  $f_H$  by setting `ri_hermes.hill_switch_factor` at runtime.

The adaptive  $f_H$  algorithm can be switched off by setting the variable `ri_hermes.adaptive_hill_` to zero. If the adaptive  $f_H$  algorithm is switched off, setting `ri_hermes.hill_switch_factor` simply defines a constant value of  $f_H$  for the duration of the simulation (analogous to Mercury and SyMBA).

We decided against devising a similar algorithm for  $f_\odot$  due to the additional difficulties that can arise. For example, an object in a circular orbit around a planet would be confused as a heliocentric orbit with a very high eccentricity, leading to large relative velocities and an excessive  $f_\odot$  value.

## 4.4 Error

Several terms contribute to the relative energy error of an integrator (e.g. Rein & Spiegel 2015):

$$E = E_{\text{floor}} + E_{\text{round}} + E_{\text{bias}} + E_{\text{scheme}}. \quad (4.1)$$

$E_{\text{floor}}$  is a constant due to the inability to represent numbers with arbitrary precision on a computer. Here we work exclusively in IEEE754 double floating point precision and thus have  $E_{\text{floor}} \sim 10^{-16}$ .

$E_{\text{round}}$  arises when a computation is performed on two floating point numbers. Almost all operations (addition, multiplication, square roots) lead to a roundoff error at the level of the machine precision. The IEEE754 standard guarantees that the round-off error in consecutive floating point operations is random, thus leading to a  $\propto t^{1/2}$  growth of  $E_{\text{round}}$  with time.

$E_{\text{bias}}$  is the error from any biased operations and grows at least as  $\propto t$ . Biased operations can originate from poor implementations<sup>3</sup> or from library functions that the IEEE754 standard does not guarantee will return unbiased results<sup>4</sup>.

$E_{\text{scheme}}$ , the final term in Eq. 4.1, is the error introduced by the algorithm itself. Typically, this quantity is bound for symplectic integrators but grows linearly with time for non-symplectic integrators.

The important question is which error term dominates, and the answer will depend on the problem at hand. For example, if a three-body system (star and two planets) is integrated with IAS15,  $E_{\text{scheme}}^{\text{ias}} \approx 10^{-28}$  and the dominant error term will be  $E_{\text{round}}$ , starting at  $10^{-16}$  and growing as  $t^{1/2}$  (see Rein & Spiegel 2015). If we instead integrate the system with WHFAST, the dominant error term will be  $E_{\text{scheme}}$ , which is determined both by the mass ratio in the system and the timestep. For typical parameters  $E_{\text{scheme}}^{\text{WH}} \sim 10^{-9}$ , and only for very long simulation times ( $\sim 10^{14}$  timesteps) will the growth of  $E_{\text{round}}$  dominate over  $E_{\text{scheme}}^{\text{WH}}$ . For biased implementations,  $E_{\text{bias}}$  will dominate the error budget at earlier times.

For typical simulations integrated with HERMES,  $E_{\text{scheme}}$  will dominate. The WH algorithm integrates a slightly different Hamiltonian from the true Hamiltonian described by the system, leading to an error that **AS[oscillates in a bounded manner]** as long as the integrated Hamiltonian remains constant. However each time a particle is transferred to or from the global simulation (see Section 4.3.3), the WH-integrated Hamiltonian changes, and thus the error will change too. For a typical WH integration, working in democratic heliocentric coordinates,  $E_{\text{scheme}}$  is (e.g. Saha & Tremaine 1994; Wisdom 2006):

$$E_{\text{scheme}}^{\text{WH}} = \frac{dt^2}{12} \{ \{ H_K, H_\beta \}, 0.5H_K + H_\beta \} + O(dt^4) \quad (4.2)$$

<sup>3</sup>For example, the expression  $x*(2./3.)$  multiplies  $x$  by a number that is consistently slightly too big or too small when represented in binary. By contrast, the expression  $2.*(x/3.)$  multiplies and divides  $x$  by numbers that are exactly representable in binary and is unbiased.

<sup>4</sup>For example, the standard library function `sqrt()` returns an unbiased result whereas `sin()` returns a biased result.

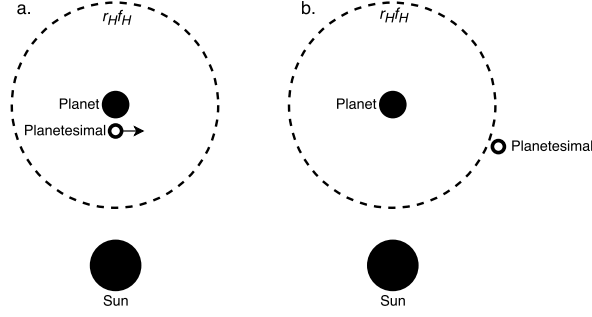


Figure 4.4: Three body problem, in the reference frame of the planet. In a. the initial setup is shown, where the planetesimal starts near the planet, inside a sphere of radius  $r_H f_H$  and the entire system is integrated purely by IAS15. Here the arrow indicates the initial direction of the planetesimal. In b. the planetesimal exits the sphere with radius  $r_H f_H$  and the system is integrated purely via WHFAST, introducing a numerical error of  $E_{\text{scheme}}^{\text{WH}}$ .

Here  $H_K$  is the Keplerian Hamiltonian,  $H_\beta = H_C + H_I$  is the summed momentum cross-term and interaction Hamiltonians, respectively, and  $\{\}$  are Poisson brackets (the quantities are explicitly defined for a test case with three particles below). For large  $N$ -body systems, Eq. 4.2 quickly becomes very difficult to evaluate analytically. However, we can gain some insight by applying Eq. 4.2 to a simple system.

We turn to a three body problem consisting of a star (active body), planet (active body) and planetesimal (semi-active body), shown in Figure 4.4. The planetesimal is initially placed inside  $f_H$  with sufficient velocity such that the distance between the planet and planetesimal grows over time. While the planetesimal is inside  $f_H$  (panel a. in Fig. 4.4) the system is integrated to machine precision by IAS15. However once the planetesimal leaves  $f_H$  (panel b. in Fig. 4.4) the system switches to being integrated by WHFAST, and an error of size  $E_{\text{scheme}}^{\text{WH}}$  is introduced.

To estimate  $E_{\text{scheme}}^{\text{WH}}$ , we start from the general Hamiltonian for an  $N$ -body system in Democratic Heliocentric coordinates:

$$H = H_0 + H_K + H_C + H_I$$

where  $H_0$  is a constant describing the motion of the centre of mass along a straight

line, and disappears when we evaluate Eq 4.2. The remaining terms in Eq. 4.4 take the form (Duncan et al. 1998):

$$H_K = \sum_{i=1}^{N-1} \frac{\mathbf{P}_i^2}{2m_i} - \sum_{i=1}^{N-1} \frac{Gm_0m_i}{|\mathbf{Q}_i|} \quad (4.3)$$

$$H_C = \frac{1}{2m_0} \left| \sum_{i=1}^N \mathbf{P}_i \right|^2 \quad (4.4)$$

$$H_I = - \sum_{i=1}^{N-1} \sum_{j=i+1}^N \frac{Gm_im_j}{|\mathbf{Q}_i - \mathbf{Q}_j|} \quad (4.5)$$

where the canonical coordinates  $\mathbf{Q}$  and  $\mathbf{P}$  are:

$$\mathbf{Q}_i = \begin{cases} \mathbf{r}_i - \mathbf{r}_0 & \text{if } i \neq 0 \\ \frac{1}{m_{\text{tot}}} \sum_{j=0}^N m_j \mathbf{r}_j & \text{if } i = 0 \end{cases} \quad (4.6)$$

$$\mathbf{P}_i = \begin{cases} \mathbf{p}_i - \frac{m_i}{m_{\text{tot}}} \sum_{j=0}^N m_j \mathbf{p}_j & \text{if } i \neq 0 \\ \sum_{j=0}^N m_j \mathbf{p}_j & \text{if } i = 0 \end{cases} \quad (4.7)$$

Here  $\mathbf{p}$ ,  $\mathbf{r}$ ,  $m$  are a particle's momentum, position and mass in any inertial frame respectively, while  $G$  is the gravitational constant and  $m_{\text{tot}} = \sum_{j=0}^N m_j$  is the total mass of the system.  $\mathbf{Q}_i$  are therefore heliocentric positions (with  $\mathbf{Q}_0$  the centre of mass), while  $\mathbf{P}_i$  are barycentric momenta (with  $\mathbf{P}_0$  the momentum of the centre of mass).

We also further simplify the system to two dimensions by considering motion in a plane. One can then straightforwardly, albeit tediously, evaluate the Poisson bracket in Eq. 4.2 by plugging in Eqs. 4.3–4.5 and taking derivatives with respect to all three particles. We make the further simplifying assumptions that  $m_0 \gg m_2 \gg m_1$  and that  $v_1 \approx v_2 \approx \sqrt{Gm_0/a}$ , where  $v$  denotes particle velocities and  $a_2$  is the semi-major axis of the planet. In addition, after solving Eq. 4.2 we set the distance of the planetesimal from the planet to  $r_H f_H$ , where  $r_H$  is the Hill radius of the planet. This is true at the moment the integration method is switched. We are then left with a single dominating term,

$$E_{\text{scheme}}^{\text{HERMES}} \approx \frac{dt^2}{12} \frac{G^2 m_0 m_1 m_2}{a_2 (r_H f_H)^3}, \quad (4.8)$$

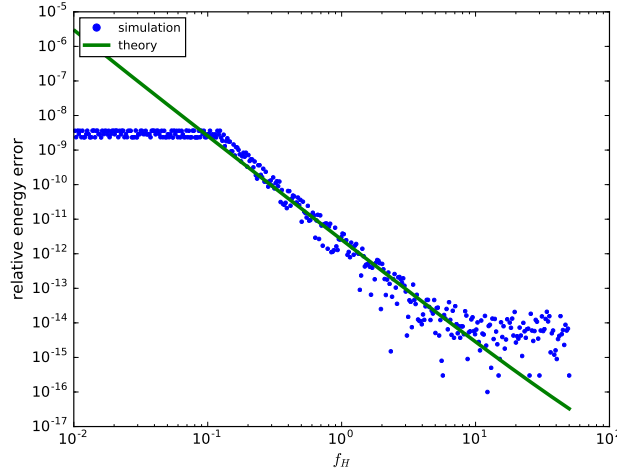


Figure 4.5: Final relative energy error as a function of  $f_H$  for a star-planet-planetesimal system. Blue dots are numerical simulations, the green curve is the theoretical prediction of Eq. 4.8.

where we have ignored numerical constants of order unity. An IPython notebook with a computer derivation is available at [https://github.com/silburt/hermes\\_ipython](https://github.com/silburt/hermes_ipython).

We compare our theoretical predictions in Eq. 4.8 to numerical tests in Figures 4.5 and 4.6. Our numerical setup consists of a star with mass  $1M_\odot$ , a Neptune mass planet on a circular orbit at 1 AU, and a planetesimal with mass  $10^{-8}M_\odot$  placed at 0.001 AU from the planet. To marginalize over the phase of the encounter when sampling the energy error, the initial position of the planetesimal is randomized for each realization. In addition, the planetesimal is given a small kick equal to the escape velocity of the planet to ensure that the planetesimal-planet distance increases with time. Each realization is simulated for 7 years. When varying the timestep in Fig. 4.6 we use a constant  $f_H = 6$ , and when varying  $f_H$  in Fig. 4.5 we use a constant timestep of  $dt = 0.058$  days.

In Figure 4.5 one can see that the numerical tests agree with the theoretical predictions of Eq. 4.8. In addition, one can see the two extreme regimes on each end of the figure. For particles starting outside the  $r_H f_H$  boundary the integrator always uses WHFAST (like panel b. of Fig. 4.4), while for particles inside the  $r_H f_H$

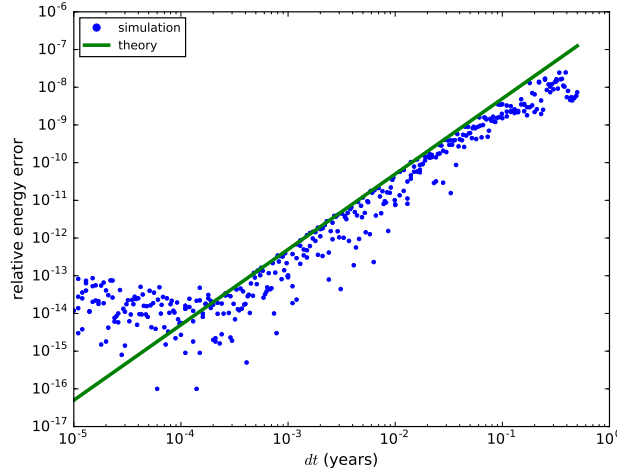


Figure 4.6: Final energy error as a function of  $dt$  for a star-planet-planetesimal system. Blue dots are numerical simulations, the green curve is the theoretical prediction of Eq. 4.8.

boundary the simulation uses IAS15 (like panel a. of Fig. 4.4). In Figure 4.6 one can see that the relative energy error is proportional to  $dt^2$ , again matching the predictions of Eq. 4.8. For both Fig. 4.5 and Fig. 4.6, we have not performed any kind of fit, we simply over-plotted Eq. 4.8 with the data from our numerical experiments. We have performed other suites of simulations testing how the energy error scales with all other relevant quantities (semi-major axis, planetesimal mass, planet mass, stellar mass) and find Eq. 4.8 in good agreement. An IPython notebook for these experiments (including tests of the other relevant quantities) is available at [https://github.com/silburt/hermes\\_ipython](https://github.com/silburt/hermes_ipython).

We now extend the characterization of the error to a more realistic case with  $N$  particles. We refer to the total relative energy error for an integration as  $E_{\text{scheme,tot}}^{\text{HERMES}}$ . Since an error of size  $E_{\text{scheme}}^{\text{HERMES}}$  is introduced each time a particle leaves/enters the global simulation, the total errors should be related to the number of close encounters,  $N_{\text{CE}}$ . In the ideal case where the integrator is unbiased, the error  $E_{\text{scheme}}^{\text{HERMES}}$  introduced by each close encounter is random, and  $E_{\text{scheme,tot}}^{\text{HERMES}}$  will grow as a  $N_{\text{CE}}^{1/2}$  random walk. However, if HERMES is biased (i.e.  $E_{\text{scheme}}^{\text{HERMES}}$  is not random), then  $E_{\text{scheme,tot}}^{\text{HERMES}}$  will grow

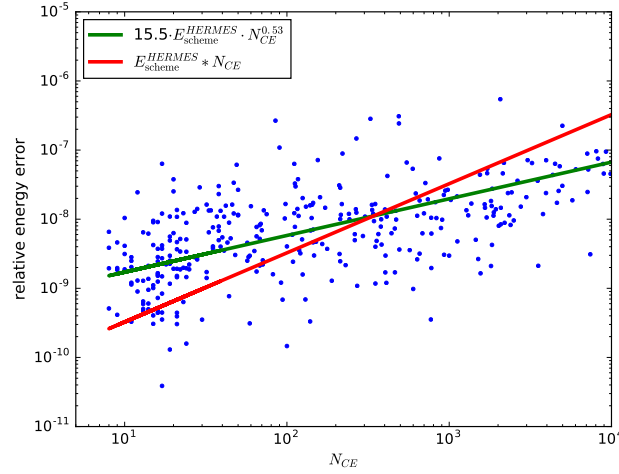


Figure 4.7: Final relative energy error as a function of the number of close encounters, for a system composed of a star, planet and 200 planetesimals. Blue dots are numerical simulations, the green line is our unbiased theoretical prediction of Eq. 4.9 with  $K = 15$ , while the red line is the biased theoretical prediction.

faster than  $N_{\text{CE}}^{1/2}$ .

Assuming the unbiased case,  $E_{\text{scheme,tot}}^{\text{HERMES}}$  is equal to:

$$E_{\text{scheme,tot}}^{\text{HERMES}} = K \cdot E_{\text{scheme}}^{\text{HERMES}} \cdot \sqrt{N_{\text{CE}}} \quad (4.9)$$

where  $K$  is a constant of proportionality. We test Eq. 4.9 against numerical tests for a Solar mass star, a Neptune mass planet on a circular orbit at 1 AU, and a disk of 200 planetesimals located between 0.98 – 1.02 AU. The initial inclinations and eccentricities of the planetesimals in the disk are set to 0, while the argument of perihelion and true anomaly are drawn from a uniform distribution. In addition, for these simulations we set  $f_{\text{H}} = 6$  and  $dt = 0.015$  years. We performed numerous integrations, integrating each realization for a randomly chosen number of orbital periods between 10-1000, yielding different numbers of close encounters.

The results are shown in Figure 4.7, the x-axis showing the number of close encounters during a simulation and the y-axis showing the final relative energy error for each simulation. We fit a power-law distribution to the data using Python's

Scipy Optimize Curve Fit package (Peterson 2009), displayed as a green line in Fig. 4.7. The resulting fit is  $E_{\text{scheme,tot}}^{\text{HERMES}} = 15.5 \cdot E_{\text{scheme}}^{\text{HERMES}} \cdot N_{\text{CE}}^{0.53}$ , so the energy growth is well approximated by Eq. 4.9. For reference, we plot the biased prediction of  $E_{\text{scheme,tot}}^{\text{HERMES}} \propto N_{\text{CE}}$  as a red line. We conclude that HERMES is unbiased for this setup. Thus, Eq. 4.9 provides an intuitive way of understanding how the error of HERMES grows without having to analytically solve Eq. 4.2 in three dimensions for  $N$  particles.

The results from Fig. 4.7 did not allow for physical collisions between particles. When physical collision are enabled a systematic bias can be introduced.

To see why, note that for each close encounter two contributions to the energy error arise according to Eq. 4.8; one when the particles are transferred from the global to the mini simulation (i.e. the ingress of the close encounter) and one when the particles are transferred back from the mini to the global simulation (i.e. the egress of the close encounter). The precise energy change depends on the specific properties of the system (phases of the orbits, angles of approach, etc.), and typically the energy changes associated with the ingress and egress of the close encounter are anticorrelated. As a result, no appreciable energy error is introduced by close encounters, and the energy over the course of a simulation grows as expected according to Eq. 4.9.

However, when a physical collision occurs in HERMES, the close encounter only has an ingress, resulting in a biased growth in the energy error. In practice this energy bias is orders of magnitude smaller than the physical energy lost during a collision, and therefore should not interfere with the longterm evolution of a system. We plan to study this issue in more detail in the future.

## 4.5 Examples

**AS[HERMES is well suited for a number of astrophysical problems. For example, planets embedded in planetesimal disks are ideal for HERMES, and was the primary motivation for building this integrator. Planet-planet scattering can also**



be easily simulated with HERMES, especially since our adaptive  $f_H$  algorithm (Section 4.3.5) protects close encounters from being missed. High eccentricity cometary clouds (e.g. the Oort cloud) are also efficiently integrated with HERMES since (by enlarging  $f_\odot$ ) pericenter passages can be resolved in the mini simulation while the remainder of the orbit is integrated in the global simulation using a large timestep. Other examples include star clusters orbiting about a central potential, tidal migration and longterm stability of planetary systems, etc. Many example problems can be found at [https://github.com/hannorein/rebound/tree/master/ipython\\_examples](https://github.com/hannorein/rebound/tree/master/ipython_examples).] Below, we highlight just a few example problems that can be simulated with HERMES.

### 4.5.1 Massive Outer Solar System

Both Duncan et al. (1998) and Chambers (1999) simulated the outer Solar System, but increased the masses of all planets by a factor of 50 to trigger close encounters between planets. Analogous to Chambers (1999) and Duncan et al. (1998) we use  $f_H = 3$ ,  $dt = 0.03$  yrs, and integrate the system for 1000 years.

We perform a number of simulations of the massive outer Solar System, and find that the relative energy error stays bounded at  $\sim 10^{-7}$  for all simulations, matching the results of Chambers (1999) and Duncan et al. (1998).

### 4.5.2 Migration of a Planet in Planetesimal Disk (Kirsh et al. 2009)

Here we reproduce the results of Kirsh et al. (2009) for the migration of a single planet embedded in a planetesimal disk. In this study a  $2.3M_\oplus$  planet orbits a Solar mass star at 25 AU, embedded in a disk of  $\sim 6 \cdot 10^4$  planetesimals. The planetesimal disk extends 10.5 AU on each side of the planet, each planetesimal has a mass 1/600th of the planet, and an overall surface density profile proportional to  $a^{-1}$  is used. The radii of all orbiting particles were determined assuming a constant

density of  $2 \text{ g/cm}^3$ . The eccentricities and inclinations were drawn from a Rayleigh distribution, which is parameterized by the scale parameter  $\sigma$ . For this experiment we use  $\sigma_e = 0.01$ , and  $\sigma_i = 0.005$ , where inclination is in radians. The argument of periaapse, true anomaly, and longitude of ascending node were all randomly drawn from uniform distributions over  $[0, 2\pi]$ . Adopting the default settings of Kirsh et al. (2009), we set HERMES to merge particles inelastically, set  $dt = 2$  years,  $f_H = 5$ ,  $f_\odot = 15$ , and track the energy lost due to collisions or ejections. We also set `r->ri_hermes.adaptive_hill_switch_factor = 1`, activating the adaptive Hill switch routine (Section 4.3.5). An IPython notebook containing the code to run this example can be found at [https://github.com/silburt/hermes\\_ipython](https://github.com/silburt/hermes_ipython).

We run 6 separate simulations, each for 70,000 years, and plot the results in Fig. 4.8. The relevant comparison plot in Kirsh et al. (2009) is the lower right panel in Figure 3. For all runs in both Kirsh et al. (2009) and our work the final position of the planet is between  $18.5 < a < 20 \text{ AU}$ , and show similar evolution tracks throughout the simulation. The relative energy error over the course of all our simulations do not exceed  $2 \cdot 10^{-7}$  after accounting for the energy lost in inelastic collisions.

### 4.5.3 Comparison to Mercury and SyMBA– Long Simulations

Here we perform a set of long simulations and compare our results to Mercury and SyMBA. These integrators are also capable of integrating complex  $N$ -body systems with close encounters, and also make use of semi-active particles. The simulations for these tests contain a Solar-mass star, a Neptune-mass planet at  $a = 1 \text{ AU}$  and a disk of 100 semi-active planetesimals distributed according to a powerlaw between  $0.8 - 1.2 \text{ AU}$ . The mass of each planetesimal is a third of a lunar mass, the eccentricities and inclinations are set to 0, and the argument of periaapse, true anomaly, and longitude of ascending node were all randomly drawn from uniform distributions over  $[0, 2\pi]$ . We set  $dt = 0.01$ ,  $f_H = 3$ , merge particles inelastically, and use our adaptive  $f_H$  routine

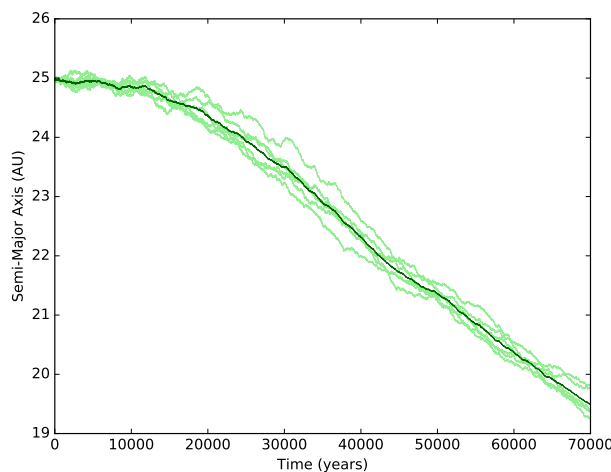


Figure 4.8: Planet’s semimajor axis vs. time, analogous to the numerical experiment in the lower right panel of Figure 3 from Kirsh et al. (2009). Light green lines represent individual runs, while the dark thicker green line represents the average of the individual runs.

(Section 4.3.5). In addition, for all three integrators we track the energy lost due to inelastic collisions and ejections so that we can isolate the numerical energy error. We accomplish this by using the `eoffset` variable in SyMBA and `EN(3)` variable in Mercury, and calculate the relative energy error according to  $(E_i + E_{\text{off}} - E_0)/E_0$ , where  $E_i$  is the total energy at iteration  $i$ ,  $E_0$  is the initial total energy and  $E_{\text{off}}$  is the energy lost due to collisions and ejections, i.e. `eoffset` in SyMBA and `EN(3)` in Mercury.

We feed identical initial conditions to SyMBA, Mercury and HERMES, and evolve all simulations for 50 Myr. We run 6 simulations per integrator that differ only by the seed of the random number generator. We average the relative energy error for these simulations to smooth out variations between individual runs. The results are presented in Figure 4.9. The top panel displays the relative energy error with each integrator, while the bottom panel shows the elapsed time for each individual run.

Looking at the top panel, SyMBA incurs significant energy jumps early in the simulation. We suspect these energy jumps are due to inadequately resolved close encounters, since the energy jumps are uncorrelated with particle collisions. We simulated runs

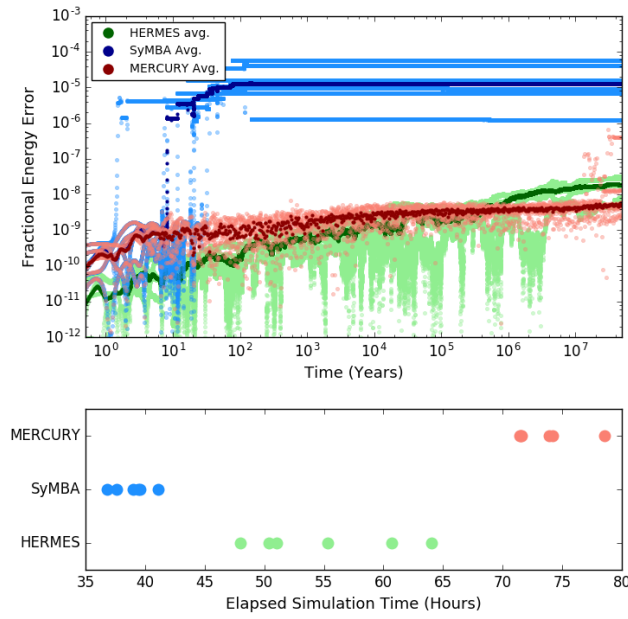


Figure 4.9: A test of HERMES, Mercury and SyMBA for collections of 50Myr, 50 planetesimal runs. Top panel shows the relative energy error over time, with individual runs in lighter shades and averaged values in dark shades. Bottom panel shows the elapsed simulation times of individual runs, using the same colour scheme as the top panel.

using different combinations of RHSCALE and RSHELL, i.e. the parameters which define close encounter regions, but were unable to resolve these energy jumps. By the end of the simulation, SyMBA is orders of magnitude less accurate than Mercury and HERMES.

We see that HERMES initially has the lowest energy error, but grows faster than Mercury. The final energy error for an integration therefore depends on the particular problem (length of simulation, timestep, number and severity of close encounters etc.). Furthermore, we find that some Mercury simulations undergo significant energy jumps, probably also due to very close encounters that are not properly resolved. Our adaptive  $f_H$  algorithm (Section 4.3.5) protects against these situations from occurring, and for a properly chosen  $f_H$  and  $dt$  combination we find the energy growth of HERMES to be well behaved.

The bottom panel shows that for these simulations HERMES is slower than SyMBA but faster than Mercury. We see that HERMES exhibits a larger variance in elapsed simulation times than Mercury and SyMBA. This is because when the adaptive  $f_H$  routine is engaged,  $f_H$  can be enlarged considerably during severe encounters, slowing down the integrator. In summary, these simulations show that HERMES provides a good balance between speed and accuracy.

## 4.6 Conclusion

In this paper we have presented HERMES, a hybrid integrator capable of integrating close encounters and collisions. HERMES integrator is composed of two parts, a global simulation which contains all particles and a mini simulation which contains all active particles (e.g. stars and planets) plus any semi-active/test particles (e.g., planetesimals) involved in a close encounter. The global simulation is integrated with WHFAST while the mini simulation is integrated with IAS15. Comparing HERMES to the openly available Mercury and SyMBA we find that HERMES provides a good balance between accuracy and speed.

HERMES takes a more direct approach when integrating close encounters over other methods. However this has enabled us to characterize the error of HERMES, and we find that the switching error from a single close encounter is well described by Eq. 4.8, which we calculate from first principles. The total energy error of HERMES for an  $N$ -body simulation is well described by a random walk, (see Eq. 4.9) with the step size being the switching error.

We have also developed an adaptive algorithm that chooses the optimal Hill switch factor,  $f_H$ , which governs the size of the close encounter region surrounding each particle. This frees the user from optimizing integrator parameters for typical cases. Finally, we have introduced a number of new features in REBOUND, including a new heliocentric version of WHFAST, semi-active particles (see Fig. 4.1) and inelastic collisions.

We have showcased a number of problems well-suited for HERMES, and compared our integrator's performance to similar integrators in the literature. In particular, we integrated the outer Solar System with planetary masses increased by a factor of 50, and we simulated a planet migrating through a disk of planetesimals, both in the limit of many planetesimals ( $\sim 10^5$ ) and short times ( $\sim 10^3$  orbits), and few planetesimals (100) and long times ( $\sim 10^8$  orbits). Many more types of problems are possible with HERMES, and additional examples can be found at <https://github.com/hannorein/rebound>.

## 4.7 Summary

My Summary.

# Chapter 5

## A Machine Learns to Predict the Stability of Tightly Packed Planetary Systems

### 5.1 Chapter Overview

The requirement that planetary systems be dynamically stable is often used to vet new discoveries or set limits on unconstrained masses or orbital elements. This is typically carried out via computationally expensive N-body simulations. We show that characterizing the complicated and multi-dimensional stability boundary of tightly packed systems is amenable to machine learning methods. We find that training a state-of-the-art machine learning algorithm on physically motivated features yields an accurate classifier of stability in packed systems. On the stability timescale investigated ( $10^7$  orbits), it is 3 orders of magnitude faster than direct N-body simulations. Optimized machine learning classifiers for dynamical stability may thus prove useful across the discipline, e.g., to characterize the exoplanet sample discovered by the upcoming Transiting Exoplanet Survey Satellite (TESS).

## 5.2 Introduction

AS[These citations are doubles of others. Need to go through this and replace them.] In order to characterize planetary systems, it is common practice to assume long-term stability in order to set upper limits on planetary masses and orbital eccentricities (e.g. Lissauer et al. 2011; Steffen et al. 2013; Tamayo 2014; Tamayo et al. 2015). This involves running grids of direct N-body integrations over the large multi-dimensional parameter space of initial conditions that are consistent with observational error. In practice, however, one can often explore only a minute fraction of the phase space; in the case of many systems discovered by the Kepler mission, each integration requires several weeks of computation to simulate timescales comparable to the star’s age ( $\gtrsim 10^{11}$  planetary orbits) with current hardware. An efficient classifier of dynamical stability would thus be invaluable.

In this investigation, we specialize to the case of tightly packed systems, where the interplanetary separations are less than 10 mutual Hill radii ( $R_H$ ), where

$$R_H \equiv \left( \frac{M_1 + M_2}{3M_\star} \right)^{1/3} a_1, \quad (5.1)$$

$M_1, M_2$  and  $M_\star$  are the masses of a pair of planets and the central star, and  $a_1$  is the semimajor axis of the inner planet. This regime has long been recognized as important in the early stages of planetary systems when bodies are still merging, and has received much attention.

For the special case of two-planet systems, one can prove that there exists a bifurcation in the dynamics that forbids planets from undergoing close encounters for all time (Marchal & Bozis 1982; Milani & Nobili 1983). In the case of co-planar, circular orbits, the transition occurs at a planetary separation of  $3.46 R_H$  (Gladman 1993). If the planets are more widely separated than this threshold, the system is Hill stable, i.e., close encounters are forbidden for all time. While there are ways for planets to escape or collide with the star without undergoing close encounters (e.g.,



Deck et al. 2012; Veras & Mustill 2013), and eccentric planets that fail this criterion can nevertheless be long-lived (e.g., Gladman 1993), the Hill criterion provides good guidance, particularly in the low-eccentricity regime (Barnes & Greenberg 2006).

In the general case with more than two planets, however, the additional degrees of freedom preclude a topological criterion for Hill stability. This has led many authors to perform suites of N-body simulations and fit empirical curves to the results. Because of the prohibitively large phase space of possible initial conditions, several authors (Chambers et al. 1996; Faber & Quillen 2007; Smith & Lissauer 2009, Obertas et al., submitted) have considered the special case of initially circular, planar orbits with all planet pairs having equal Hill separations  $\Delta$ , defined as the difference in semimajor axis divided by  $R_H$ . They find that even in cases where each pair of planets satisfies the Hill criterion, the system nevertheless destabilizes, and that the associated timescale seems to grow exponentially with Hill separation. However, the fitted coefficients vary as the number of planets and planetary masses are varied, and introducing inclinations (Marzari & Weidenschilling 2002), eccentricities (Ito & Tanikawa 1999; Chatterjee et al. 2008; Pu & Wu 2015), or unequal spacings between planets (Marzari 2014) change the instability timescales substantially. For a given planetary system, it is therefore not always clear which scaling law is appropriate to apply, and what confidence one can have in the resulting estimate.

For this investigation we take a machine learning approach. High dimensional classification tasks are ubiquitous across industry and data science, and sophisticated machine learning algorithms have been developed to tackle these problems. Such techniques have been highly successful in an astronomical context for several image classification tasks, e.g., assigning morphological types to galaxies (Collister & Lahav 2004); however, they have seen little use in dynamical classification to date (see Petrovich 2015, for a recent counterexample).

## 5.3 Methods

We choose to frame the problem as a binary classification task, i.e., predicting whether or not a given planetary system is stable (over a given timescale). Each “example” (planetary system) is described by a set of “features” that the algorithm uses to predict stability, in the form of a probability between 0 and 1. In supervised machine learning, an algorithm is first trained on examples where it is told the correct answer (stable or not stable). The trained algorithm can then be used to predict on new examples.

### 5.3.1 Dataset

In order to train our algorithms, we generated a dataset of 5000 N-body integrations of 3-planet systems over  $10^7$  orbits of the innermost body. We focus on 3-planet systems since there exists an analytic criterion for the case of two planets, and systems with more planets exhibit qualitatively similar behavior. The number of simulations and length of integration were chosen to generate a dataset at limited computational cost, and assess the value of investing significant computing time to train classifiers on astrophysically relevant timescales of  $\sim 10^9$  orbits. Because we expect that instability timescales of  $10^7$  and  $10^9$  orbits are both physically driven by Chirikov diffusion due to the overlap of mean-motion resonances (see Fig. 2 in Obertas et al., submitted), we expect the performance of models trained on this dataset to be comparable to that of similar algorithms trained on longer datasets.

With a view toward applying these models to Kepler discoveries, we adopted a solar-mass star,  $5 M_{\oplus}$  (Earth-mass) planets, and drew the innermost planet’s semimajor axis randomly between 0.04 and 0.06 AU. We note, however, that our results are strictly scale-free, and can be applied to comparable systems with masses, orbital periods and semimajor axes expressed in terms of the star’s mass, innermost planet’s orbital period and semimajor axis, respectively. The second planet’s semimajor axis was separated from the first by a number of mutual Hill radii drawn from a uniform

distribution in the range  $[5, 9]$ . The third planet’s separation was then independently drawn from the same distribution, yielding unevenly spaced planets. The particular range of Hill-radius separations was chosen to capture the regime of interest on our adopted timescale of  $10^7$  orbits and roughly generate a balanced dataset of stable and unstable systems (this yielded 1479 stable systems out of 5000). Eccentricities and inclinations were drawn independently for each planet from uniform distributions over  $[0, 0.02]$  and  $[0, 1^\circ]$ , and the remaining angles were drawn randomly over  $[0, 2\pi]$ .

All integrations were performed using the WHFAST integrator (Rein & Tamayo 2015) in the open-source REBOUND N-body package (Rein & Liu 2012), which is written in C99 and comes with an optional python interface. We adopted a timestep of 1% of the innermost planet’s orbital period, and classified systems as unstable if any pair of planets came within 1 Hill radius of each other during the simulation.

### 5.3.2 Metrics

Binary classifiers are often evaluated on their *precision* (here the fraction of systems that are actually stable when the model predicts stability) and *recall* (the fraction of systems the model predicts are stable out of the truly stable cases). For typical algorithms that predict probabilities of class membership, one can trade off between precision and recall by varying the threshold probability for classification. For example, a conservative model that only classifies systems as stable if it predicts a probability of stability greater than 0.99 will be right most of the times that it predicts stability (high precision), but will miss all the stable systems that were assigned slightly lower probabilities (low recall). The appropriate threshold depends on the application (e.g., if predicting DNA matches for crime cases, one might set a high threshold as above to have confidence in predicted matches).

When comparing two models, one can plot pairs of precision and recall scores for all possible thresholds to generate a precision-recall curve. A common scalar metric

for comparing classifiers is the area under this curve (AUC), which would be unity for a perfect model.

### 5.3.3 Algorithm Training

After experimenting with several machine learning algorithms (random forest and support-vector machine implementations in the Python `scikit-learn` library), we found that gradient-boosted decision trees (GBDT<sup>1</sup>) `XGBoost v0.6` (Chen & Guestrin 2016) gave the best results for our dataset.

A recurring theme in machine learning is that of “overfitting,” an algorithm’s tendency to latch onto irrelevant idiosyncrasies in the training set that cause it to predict poorly on unseen examples. Different algorithms therefore try to penalize overly complicated models in an effort to retain only the broad features that are likely to generalize well. In practice, the user navigates this balance between simplicity and complexity empirically, by tuning an algorithm’s “hyperparameters” that mediate this tradeoff, training it, and checking performance (Sec. 5.3.2) on unseen data; this process, together with trying different features to maximize performance, is known as cross-validation. In order to rule out the possibility of (sometimes subtle) mistakes in cross-validation yielding overly optimistic performance metrics, it can be good practice to assign a subset of the data to a holdout (test) set that is never seen by the algorithm during cross-validation. Evaluation of the final model on the holdout set therefore provides robust metrics of the trained algorithm’s expected performance on unseen examples; consistency between the cross-validation and test scores also suggest a robust cross-validation methodology. In our case, we randomly assigned 1500 systems to a holdout test set, and used only the remaining 3500 for cross-validation.

A typical technique to reduce statistical fluctuations when comparing the perfor-

---

<sup>1</sup>GBDT algorithms create and combine large numbers of individually weak but complementary classifiers to yield a robust estimator (Friedman et al. 2001)

mance of different sets of hyperparameters is  $k$ -fold cross validation. One begins by splitting the training examples into  $k$  evenly sized groups; then, for each group, one trains the model on the remaining  $k - 1$  chunks, and uses the remaining group to evaluate performance. The scores from the  $k$  folds are then averaged, reducing the variance in the estimate. Finally, it is generally good practice to use stratified cross-validation, whereby one ensures that each of the  $k$  folds is assigned an approximately equal number of samples from each class (stable and unstable).

XGBoost has several hyperparameters, so we sequentially performed grid searches through 2-dimensional cuts through the parameter space, evaluating performance through the precision-recall AUC (Sec. 5.3.2) using stratified, 5-fold cross-validation on the training set of 3500 examples. Values of the final adopted hyperparameters for the algorithm are discussed in Sec. 5.4.1 and 5.4.2 can be found in Table 5.1.

## 5.4 Results

### 5.4.1 Model 1: Learning from Initial conditions

We begin by considering as features the initial orbital elements and orbital period of each planet, and the interplanetary separations between adjacent planets in units of mutual Hill radii. We then trained an XGBoost classifier on these features (Section 5.3.3), allowing us to predict the stability of each system in the test set in the form of an estimated probability.

As discussed in Section ??, a threshold probability is required for classifying a system as stable/unstable, and is a subjective choice that depends on the desired qualities of the classifier. For our purposes we argue it is logical to adopt a conservative threshold, in the sense that if the model predicts stability, there is a strong likelihood that the system is actually stable (high precision). This follows from the fact that it is computationally much faster to verify that a system is unstable (on short timescales)

than it is to check that it is stable (on long timescales). We choose to require a precision of 90% on our test dataset, which corresponded to the model only classifying systems as stable if their predicted stability probability is larger than a 0.785 threshold.

Since previous works have identified the Hill separations between adjacent planets as important features (Chambers et al. 1996; Marzari 2014), we plot the performance of the model projected onto this 2D plane (Fig. 5.1).

Looking at the dashed, black line in Figure 5.1, one can see that to first order, the model's prediction boundary roughly obeys the relation  $\Delta_1 + \Delta_2 > 16.1$ . This is in fact the form of the simple criterion suggested by Lissauer et al. (2011), who quote  $\Delta_1 + \Delta_2 > 18$  for stability on timescales of  $10^9$  orbits. Because we consider stability on shorter timescales, the threshold number of Hill radii should be adjusted for a fair comparison. We term models of the form  $\Delta_1 + \Delta_2 > x$  "Lissauer-family" models, and find 16.1 is the threshold for Lissauer-family models that yields a precision of 90% on this dataset.

As stated above, a conservative probability threshold has the disadvantage that the model will misclassify many stable systems as unstable (low recall). This is easily seen by considering different Lissauer-family models (dashed black line in Fig. 5.1), i.e. imposing different threshold values than 16.1 and generating lines parallel to the one plotted. Larger threshold values ensure that a larger fraction of the systems to the right of the boundary (i.e., those predicted stable) are in fact stable (blue), leading to higher precision. However, this lowers the recall, since now fewer of the stable systems (blue) are predicted to be stable by the model (i.e., lie to the right of the line). For a fixed precision of 90%, the machine learning model has a significantly higher recall (52%) than the Lissauer-family model (30%). This is because the machine learning model can use information in the features not visible in this 2D projection to make better predictions.

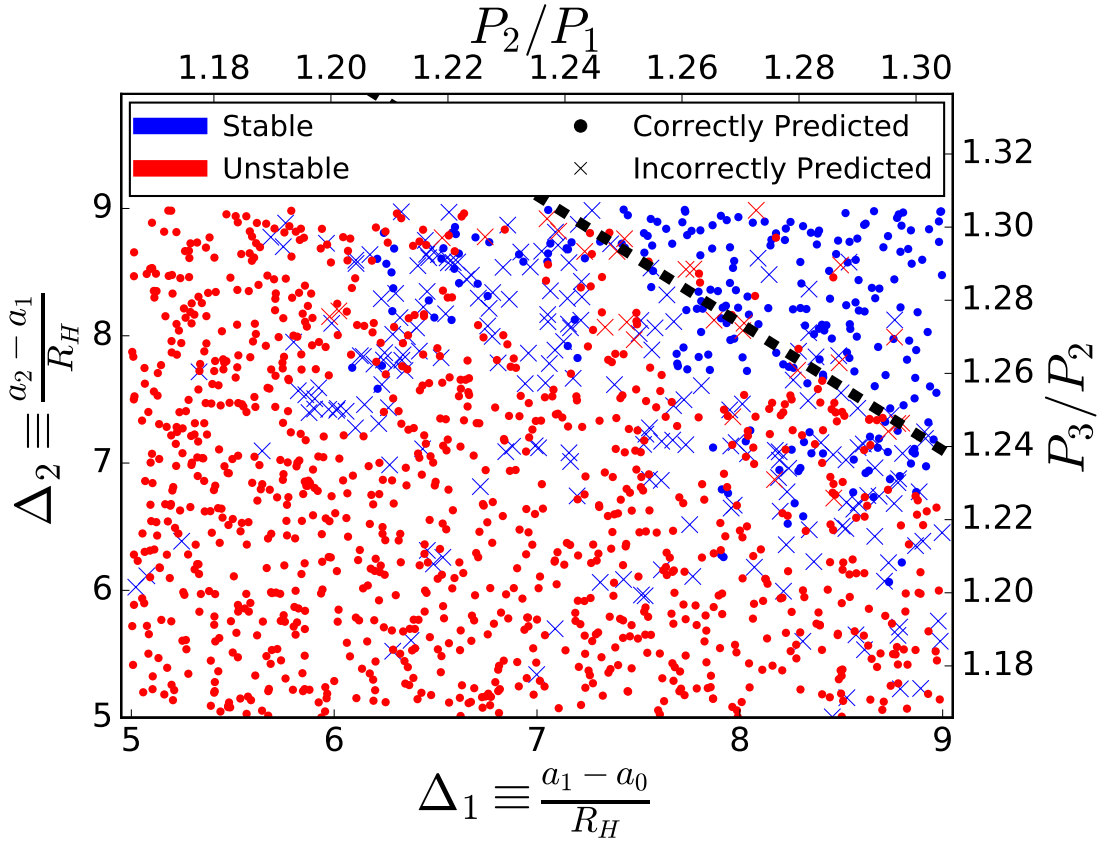


Figure 5.1: Performance on the test dataset using the machine learning model trained on system's initial conditions. Stable systems are marked blue, unstable systems are marked red. Correctly classified systems are plotted as circles, incorrect predictions are marked as crosses. The bottom and left axes show Hill-sphere separations  $\Delta$  for the inner and outer planet pairs, respectively. The top and right axes correspond to period ratios between the planet pairs. The dashed black line corresponds to the Lissauer-family model  $\Delta_1 + \Delta_2 > 16.1$ .

### 5.4.2 Model 2: Generating Features from Short Integrations

An important factor determining the performance of a machine learning algorithm is the quality of the features it is provided for each of the training examples. To this end, we improved upon the previous model (Section 5.4.1) by generating new features from short N-body integrations. To create the new features, we performed simulations over  $10^4$  orbits (0.1% of the instability timescale probed) for each of the 5000 systems in the dataset, and recorded each planet’s orbital elements and the current Lyapunov timescale every 5 orbits.

Because we suspect that the instability is driven by overlapping mean-motion resonances, we first generated features that capture the variation in semimajor axes, which would vanish if the dynamics were purely secular (Murray & Dermott 1999). In particular, we generated features for the standard deviation and maximum value of each planet’s semimajor axis over the  $10^4$  orbits, normalized to the mean value over the same period (`std_ai` and `max_ai`, where *i* denotes the planet number). In addition, we generated features for the same quantities over only the first 50 orbital periods in order to capture the variations on orbital timescales (`std_window_ai` and `max_window_ai`). Furthermore, we noticed in early attempts that some misclassified systems exhibited drifts in semimajor axis, so we generated slope features from linear fits to each of the three planets’ semimajor axes, normalized to the mean semimajor axis divided by the integration time (`slope_ai`). For the eccentricities of each planet, we generated features for the mean, standard deviation, maximum and minimum values over the full  $10^4$  orbits, and normalized them to the eccentricity that planet would require to reach its nearest neighbor’s semimajor axis (`avg_ei`, `std_ei`, `max_ei`, `min_ei`). For the Lyapunov time we generated a single feature corresponding to the value measured at the end of the integration, normalized to the innermost orbital period. Finally, we added features for the two pairs of initial Hill-radius separations, and for the minimum and maximum initial Hill-radius separations. We experimented



with adding features involving the planetary inclinations, but they did not significantly improve the models.

A summary of all the features used can be found in Table 5.2, which are ordered by their importance. We quantify the importances through the Gain value recorded by XGBoost, which corresponds to the gain in accuracy that a given feature provides when it is introduced into the underlying decision trees used by XGBoost. The units are normalized so that the gains sum to 100. We find that the variations in the middle planet’s semimajor axis are the most informative in this sense. We interpret this as suggesting that the instabilities in these closely packed systems are driven by the overlap of mean motion resonances (which change the semimajor axes), rather than secular effects (which would keep the semimajor axes constant).

Finally, we compare the performance of this ‘short-integration’ model to the previous ‘initial-condition’ model. Fig. 5.2 shows that while both models often assign unstable systems (blue bins) a low predicted probability, the ‘initial-condition’ model assigns stable systems (green bins) a wide range of predicted probabilities, translating to a lower recall. In contrast, the ‘short-integration’ model more confidently assigns high predicted probabilities to stable systems, better separating the two classes. Again setting the predicted probability threshold so as to obtain 90% precision, the recall improves to 68%.

## 5.5 Discussion & Conclusion

In this investigation, we numerically integrated a dataset of 5000 three-planet systems over  $10^7$  orbits. We then trained machine learning algorithms to classify systems’ orbital stability on this timescale. In particular, we trained two models using the gradient-boosted decision trees algorithm XGBoost, an ‘initial-conditions’ model (Sec. 5.4.1) that learned only from the system’s initial orbital elements, and a ‘short-integration’ model (Sec. 5.4.2) that generated features from short N-body integrations.

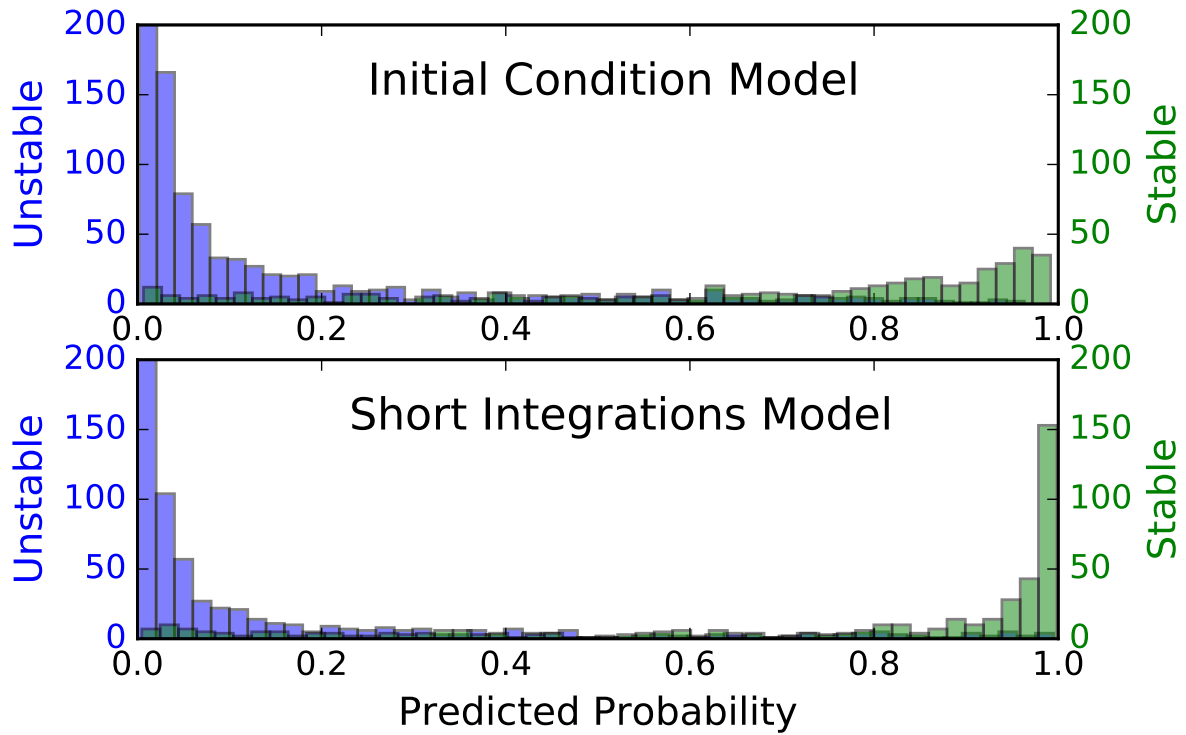


Figure 5.2: Comparison of predictions of the initial-condition and short-integration models on the test set. Stable systems are shown in green, unstable systems are shown in blue, and the model-predicted probability of stability for each system is shown along the x-axis. The leftmost blue bin is cut off to render smaller bins visible—in the top panel it reaches 395, and in the bottom panel 640.

We then compared their performance to ‘Lissauer-family models’ that require the sum of the interplanetary separations (expressed in mutual Hill radii) to be greater than a particular threshold.

We summarize the investigated models’ performances in Fig. 5.3, which plot values for the respective classifier’s precision and recall for all possible values of the probability threshold above which the model labels a system as stable. As discussed above, the appropriate choice of this threshold depends on the desired qualities of the classifier. Above we advocated for conservative models that are correct 90% of the time when a system is predicted stable (90% precision), but different applications might consider different criteria.

By generating dynamically relevant features from short integrations, our best machine-learning model:

- Dominates other models at all threshold values.
- Recovers 2.25 as many of the truly stable systems (has 2.25 times higher recall) as a Lissauer-family model at a fixed precision of 90%.
- Is three orders of magnitude faster than direct N-body integration. Performing the short integration, generating the features and evaluating the model for a given system takes  $\sim 1$  second with current technology.

An important limitation of this work are the fixed masses (5 Earth masses around a solar-mass star) and the comparatively short integration timescales ( $10^7$  orbits). Our results strongly motivate investing computational time to generate datasets over longer timescales with a range in masses. Running these integrations in a reproducible and openly accessible manner (Rein & Tamayo, in prep.) would allow this dataset to be used as a standard on which current and future models could be evaluated and compared, and as a database of integrations to test theoretical investigations.

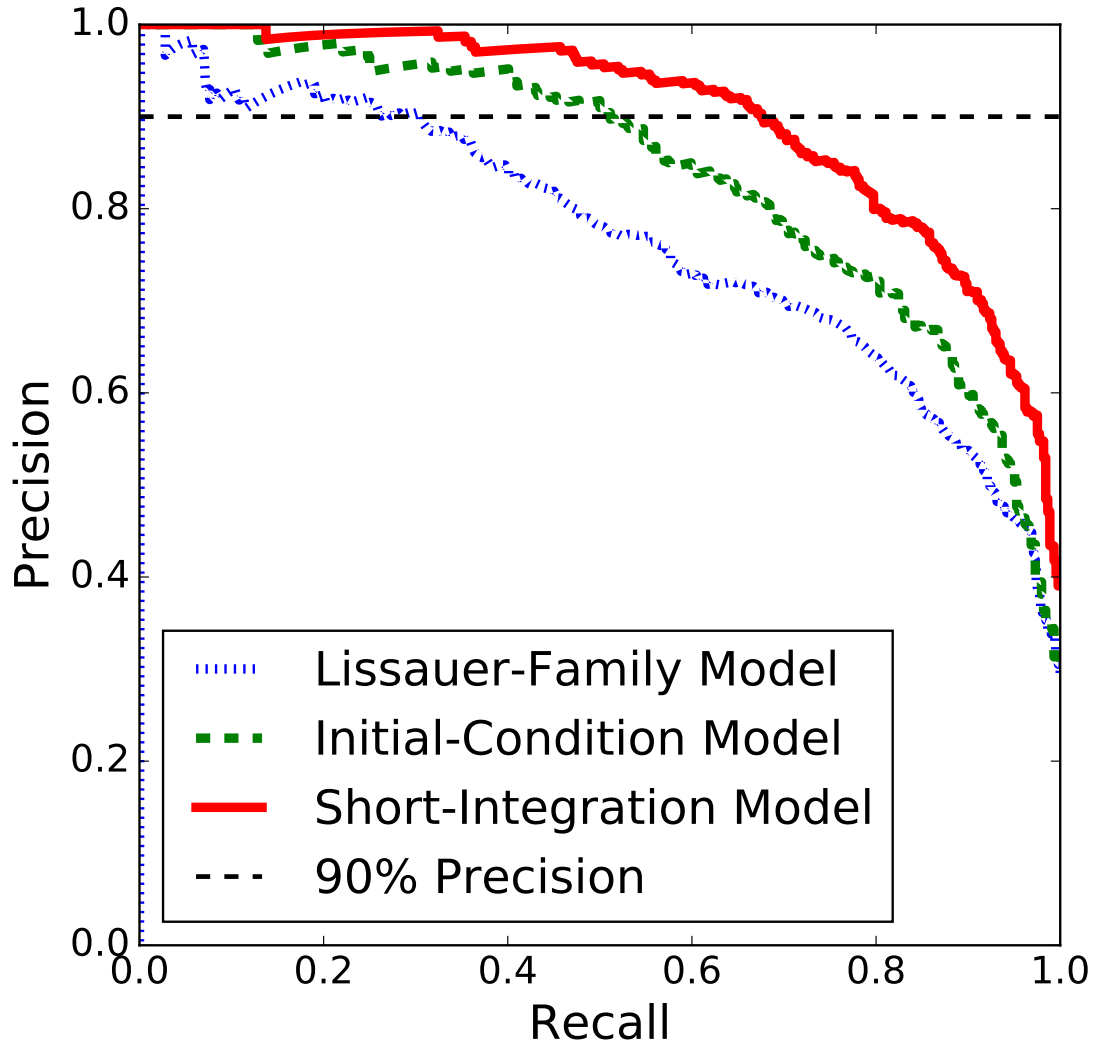


Figure 5.3: Precision-recall curves for each model in this paper, generated from all possible values of the model's threshold classification probability. The Lissauer-family models predict stability if the sum of the Hill-sphere separations is greater than a particular threshold, and the corresponding curve was generated by considering all possible threshold values. The horizontal black-dashed line is the 90% precision requirement we imposed on all models in this paper.

Such classifiers could be used in many of the ways that direct N-body integrations currently are employed, but these models' dramatically improved efficiency would allow much faster and complete explorations of parameter space, e.g.:

- Mapping out the stability boundary in mass-eccentricity space for observed transiting systems.
- Mapping out the parameter space that unseen planets could stably inhabit in a given system to guide observational follow-up strategies or theoretical considerations.
- Vetting low signal-to-noise detections through stability constraints.
- Generating stable or unstable systems for theoretical population studies.
- As a stopping condition for simulations once they achieve a dynamically long-lived configuration.

Such tools may be of particular interest for the upcoming Transiting Exoplanet Survey Satellite (TESS). While transit-timing variations (TTVs) have been powerful tools for constraining the masses and eccentricities of near-resonant Kepler systems (e.g., Ford et al. 2012; Steffen et al. 2013; Deck & Agol 2015), TESS' shorter time baselines and planets' smaller semimajor axes will render such analyses difficult or impossible. It is therefore likely that in many systems, stability considerations will provide the strongest constraints on planetary masses and eccentricities, and this will be important for guiding the substantial radial-velocity follow-up efforts from the ground.

More broadly, we have shown that machine learning can be a powerful tool for high-dimensional classification problems in dynamics and other fields. But in addition to their predictive power, our models also revealed new insights into the underlying dynamics. In particular, the most informative features in our model based on short

integrations were the variations in the middle planet's semimajor axis. This suggests that the orbital instabilities are driven by the overlap of mean motion resonances (which vary the semimajor axes) rather than the secular chaos at work in our own solar system (Lithwick & Wu 2011; Batygin et al. 2015), which proceeds with constant semimajor axes.

## 5.6 Summary

My Summary.

Table 5.1: Hyperparameters used for the initial-conditions (IC) model (Sec. 5.4.1) and short-integrations (SI) model (Sec. 5.4.2), and their associated performance.

	IC Model	SI Model
base_score	0.5	0.5
colsample_bylevel	1	1
colsample_bytree	1	1
gamma	0	0
learning_rate	0.001	0.00359
max_delta_step	0	0
max_depth	6	8
min_child_weight	1.0	1.2
missing	None	None
n_estimators	5000	5000
objective	binary:logistic	binary:logistic
reg_alpha	0	0
reg_lambda	1	1
scale_pos_weight	1	1
seed	27	27
subsample	0.4	0.5
AUC (Cross-Validation)	$0.842 \pm 0.012$	$0.911 \pm 0.012$
AUC(Test Dataset)	0.843	0.898
Recall (At 90% Precision)	0.52	0.68

Table 5.2: ‘Short-Integration’ Model Feature Importances. See text for a description of the gain and of the features.

Feature	Gain
max_a2	20.3
std_a2	8.3
mindaOverRH	2.6
maxdaOverRH	2.6
std_a3	2.3
max_e2	2.3
26 more features...	



# Chapter 6

## Resonant structure, formation and stability of the planetary system HD155358

### 6.1 Chapter Overview

Two Jovian-sized planets are orbiting the star HD155358 near exact mean motion resonance (MMR) commensurability. In this work we re-analyze the radial velocity (RV) data previously collected by Robertson et al. (2012). Using a Bayesian framework we construct two models – one that includes and one that excludes gravitational planet-planet interactions (PPI). We find that the orbital parameters from our PPI and noPPI models differ by up to  $2\sigma$ , with our noPPI model being statistically consistent with previous results. In addition, our new PPI model strongly favours the planets being in MMR while our noPPI model strongly disfavours MMR. We conduct a stability analysis by drawing samples from our PPI model’s posterior distribution and simulating them for  $10^9$  years, finding that our best-fit values land firmly in a stable region of parameter space.

We explore a series of formation models that migrate the planets into their observed MMR. We then use our formation models to directly fit to the observed RV data, where each model is uniquely parameterized by only three constants describing its migration history. Using a Bayesian framework we find that a number of formation models fit the RV data surprisingly well, with some migration parameters being ruled out.

Our analysis shows that planet-planet interactions are important to take into account when modelling observations of multi-planetary systems. The additional information that one can gain from interacting models can help constrain planet formation parameters.

## 6.2 Introduction

The past decade has marked an explosion in the number of discovered multi-planet systems, with almost 600 known to date (NASA Exoplanet Archive 2017). Jovian planets have been detected in these exoplanetary systems, and the range of conditions under which they can form is uncertain. For example, many Jovian planets are observed inside the snowline of their host star (e.g. Hayashi 1981), and it is unclear whether they formed in-situ (Boley et al. 2016; Huang et al. 2016; Batygin et al. 2016) or beyond the snowline and migrated in afterwards (Mayor & Queloz 1995; Lin et al. 1996; Pollack et al. 1996). For systems near mean motion resonance (MMR), planetary migration offers a natural formation mechanism (e.g. Lee & Peale 2002; Rein & Papaloizou 2009). Since roughly 30% of Jovian-sized planets with a detected planet companion are near a first-order MMR (NASA Exoplanet Archive 2017), at least a substantial fraction of planetary systems are likely to have formed via migration.

The star HD155358 hosts two observed Jovian-sized planets orbiting inside the snowline near a MMR. The star has a mass of  $0.92 M_{\odot}$ , and the planets have orbital periods  $P_1 = 194$  and  $P_2 = 392$  days, respectively, about 2% away from the exact 2:1

commensurability (Robertson et al. 2012, hereafter R2012). In addition, HD155358 is also among the lowest metallicity stars known to host Jovian-sized planets (Cochran et al. 2007). Since the presence of MMR can provide additional constraints on formation and evolution, HD155358 provides an opportunity to better understand the formation of Jovian planets in exoplanetary systems.

The HD155358 system has been previously studied by many scientists (Cochran et al. 2007; Fuhrmann & Bernkopf 2008; Robertson et al. 2012; André & Papaloizou 2016). Of particular interest is the work by R2012, who updated the orbital parameters initially reported by Cochran et al. (2007) after collecting additional radial velocity (RV) observations. In R2012 the orbital properties were derived from GAUSSFIT (Jefferys et al. 1988) and SYSTEMIC (Meschiari et al. 2009), and planet-planet interactions were not included in their analysis (Robertson 2016, private communication). For well-separated orbits this assumption is valid and simplifies the analysis. However, near a MMR this approximation can lead to different orbital solutions and therefore different formation constraints and evolutionary predictions. In particular, without planet-planet interactions one cannot draw any conclusion as to whether the system is in resonance or not.

In this work we re-analyze HD155358 using the RV observations collected by R2012. In Sect. 6.3, we derive new orbital parameters using a Bayesian framework coupled to direct N-body integrations and assess the probability that the system is in resonance. In Sect. 6.4, we perform simulations constraining the formation history, and in Sect. 6.5 conduct a stability analysis. We conclude with a discussion in Sect. 6.6.

## 6.3 Best-Fit Parameters and Resonance Analysis

### 6.3.1 Methods

The RV data used for this analysis comes from Table 2 of R2012. We model this system using REBOUND (Rein & Liu 2012), an open-source N-body code for simulating problems in planetary dynamics. Using REBOUND we can extract the motion of the central star over the course of our simulation, comparing it directly to the RV data.

In this work we explore two different models – one that includes the planet-planet gravitational interactions, abbreviated as PPI model, and one that excludes planet-planet gravitational interactions, abbreviated as noPPI model. This is achieved in REBOUND by initializing each planet as either a massive body (PPI model) or a semi-active particle (noPPI model). Semi-active particles can gravitationally interact with massive bodies (e.g. the central star), but cannot interact with other semi-active particles. For reference, R2012 does not include the gravitational interactions between the planets, and is analogous to our noPPI model.

We construct our models using a Bayesian framework, where the quantity of interest is the posterior probability density function. Benefits of conducting an analysis within a Bayesian framework include marginalization over nuisance parameters, preservation of correlations between parameters, and a natural Occam’s razor when comparing models (see e.g. Gregory 2005, for a full discussion). Using Bayes’ theorem we calculate the (unnormalized) posterior probability according to:

$$p(\theta|D) \propto p(D|\theta)p(\theta),$$

where  $\theta$  are the parameters in our model,  $D$  is our data,  $p(\theta)$  is our prior probability on  $\theta$ ,  $p(D|\theta)$  is the probability of  $D$  given  $\theta$  (i.e. the likelihood function), and  $p(\theta|D)$  is our posterior probability. As with most models that employ Bayes’ theorem, the posterior probability cannot be analytically computed, requiring the use of numerical

methods for approximating it. We use EMCEE, an open-source affine-invariant Markov chain Monte Carlo (MCMC) routine (Foreman-Mackey et al. 2013).

For our models we assume that the system is co-planar, and use the known value of stellar mass,  $m_* = 0.92M_\odot$ . For each planet we have the following parameters: the reduced mass,  $m \sin(i)$ , the semi-major axis,  $a$ , the eccentricity,  $e$ , the argument of periapsis,  $\omega$ , and the mean anomaly  $M$ . To avoid singularities for  $\omega$  (which is ill-defined when  $e \sim 0$ ), we fit  $h = e \sin(\omega)$  and  $k = e \cos(\omega)$  instead of  $e$  and  $\omega$ . We also add an offset parameter  $\gamma$  to account for any stellar drift along the line of sight, a jitter parameter  $J$  to account for any stellar noise and unreported instrument variability, and a viewing angle parameter  $\sin(i)$ . This yields a total of 13 parameters to be sampled by the MCMC.

We initialize our MCMC chain with values similar to the best fit values of R2012 to speed up convergence, and use the following priors on our parameters:  $0.4M_J < m_1 \sin(i) < 2M_J$ ,  $0.4M_J < m_2 \sin(i) < 2M_J$ ,  $0.2\text{AU} < a_1 < 0.8\text{AU}$ ,  $0.8\text{AU} < a_2 < 1.4\text{AU}$ ,  $1 < h_1, h_2, k_1, k_2 < -1$ ,  $0 < \omega_1, \omega_2, M_1, M_2 < 2\pi$ ,  $-40\text{m/s} < \gamma < 40\text{m/s}$ , and  $0\text{m/s} < J^2 < 50\text{m/s}$ . Our MCMC chain consists of an initial burnin phase of 1000 steps with 400 walkers, after which the MCMC walkers are resampled near the best solution and run for 5000 steps. In REBOUND we use the WHFAST integrator (Rein & Tamayo 2015) with a timestep of  $P_1/200$ , leading to a bounded relative energy error of  $< 10^{-7}$ .

### 6.3.2 Best Fit Parameters

Our maximum a-posteriori (MAP) values for each parameter are displayed in Table 6.1. For ease of comparison between our results and R2012, we convert back into  $e$  and  $\omega$  variables from  $h$  and  $k$  variables. Since we find  $\sin(i)$  unconstrained in our MCMC analysis (see Figure 6.4) it is not listed in Table 6.1. Parameters with subscript 1 relate to the inner planet, while parameters with subscript 2 relate to the outer planet. A

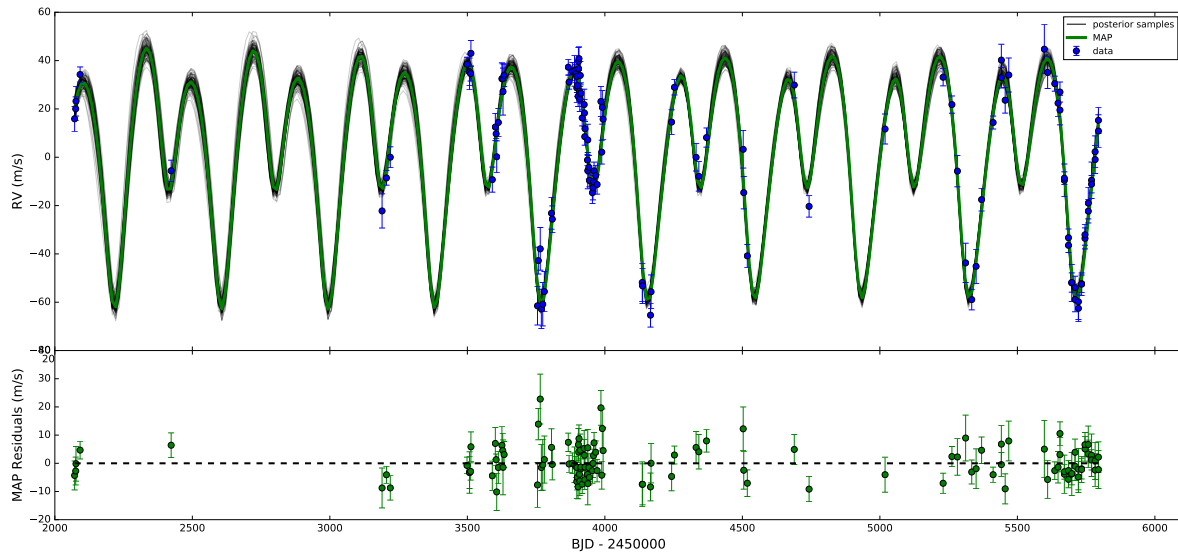


Figure 6.1: RV data and PPI model fit. Top panel shows the RV data points, MCMC MAP value (green), and 100 randomly plotted samples from the posterior (black). Bottom panel shows the residuals for the MAP fit to the RV data.

random sample of 2000 draws from our PPI model’s posterior distribution is shown in Figure 6.4.

From Table 6.1 there are a few statistically significant differences between our PPI and noPPI models. In particular,  $e_2$  is inconsistent at the  $1\text{-}\sigma$  level, while  $m_1 \sin(i)$ ,  $\omega_1$  and  $M_1$  are inconsistent at the  $2\text{-}\sigma$  level. Furthermore, every parameter in our noPPI model is statistically consistent with R2012.

In the top panel of Figure 6.1 we plot the MAP estimate for our PPI model, along with 100 randomly drawn samples from our posterior distribution. In the lower panel the residuals between our MAP estimate and the RV data are shown. As can be seen, our PPI model represents a good fit to the data.

We also try adding two additional parameters to our PPI model to account for mutual inclination between the planets. For this inclination model we add  $i_{x,2} = 2\sin(i_2/2)\cos(\Omega_2)$  and  $i_{y,2} = 2\sin(i_2/2)\sin(\Omega_2)$ , where  $i_2$  is the inclination of the

Parameter	PPI model	noPPI model	R2012
$m_1 \sin(i) (M_J)$	$0.92 \pm 0.04$	$0.82 \pm 0.04$	$0.85 \pm 0.05$
$m_2 \sin(i) (M_J)$	$0.85 \pm 0.03$	$0.87 \pm 0.03$	$0.82 \pm 0.07$
$a_1$ (AU)	$0.641 \pm 0.002$	$0.643 \pm 0.004$	$0.64 \pm 0.01$
$a_2$ (AU)	$1.017 \pm 0.005$	$1.015 \pm 0.007$	$1.02 \pm 0.02$
$e_1$	$0.17 \pm 0.03$	$0.18 \pm 0.03$	$0.17 \pm 0.03$
$e_2$	$0.10 \pm 0.04$	$0.20 \pm 0.05$	$0.16 \pm 0.1$
$\omega_1$	$178^{\circ+14^{\circ}}_{-17^{\circ}}$	$142^{\circ} \pm 13^{\circ}$	$143^{\circ} \pm 11^{\circ}$
$\omega_2$	$241^{\circ+72^{\circ}}_{-65^{\circ}}$	$189^{\circ+10^{\circ}}_{-16^{\circ}}$	$180^{\circ} \pm 26^{\circ}$
$M_1$	$91^{\circ+15^{\circ}}_{-18^{\circ}}$	$124^{\circ} \pm 15^{\circ}$	$129^{\circ} \pm 0.7^{\circ}$
$M_2$	$178^{\circ+73^{\circ}}_{-66^{\circ}}$	$244^{\circ+12^{\circ}}_{-17^{\circ}}$	$233^{\circ} \pm 0.9^{\circ}$
$\gamma$ (m/s)	$3.76 \pm 0.71$	$3.70 \pm 0.70$	—
$J$ (m/s)	$2.90^{+0.78}_{-0.64}$	$2.92^{+0.78}_{-0.62}$	2.49

Table 6.1: Best-fit model parameters from our MCMC samples. Our PPI model includes planet-planet interactions, while our noPPI model excludes planet-planet interactions. The derived parameters from R2012 are also listed for ease of comparison.

outer planet (with respect to the inner planet and star) and  $\Omega_2$  is the longitude of ascending node of the outer planet (Pál 2009). Comparing this inclination model to our original PPI model using a posterior odds ratio (see Section 6.4.2) yields a value of 0.4, indicating a slight preference over the inclination model. In addition, since our original PPI model is simpler and the model parameters between models are similar, we choose to stick with our PPI model for the remainder of our analysis.

### 6.3.3 Resonance Analysis

Using our posterior samples found in Section 6.3.2, we can assess the likelihood that the planets orbiting HD155358 are in 2:1 MMR. More specifically, we can draw samples from the posterior distribution and calculate what fraction of these systems have librating resonant angles. The resonant angles are calculated according to:

$$\phi_1 = (j - 1)\lambda_1 - j\lambda_2 + \omega_1$$

$$\phi_2 = (j - 1)\lambda_1 - j\lambda_2 + \omega_2$$

where  $\lambda$  is the mean longitude,  $\omega$  is the argument of periapsis, and  $j$  is the order of the resonance ( $j = 2$  for this work). Our aim is to use the fraction of systems with librating resonant angles as a measure of how likely the system is to be in MMR.

For each set of parameters drawn from our posterior we simulate the corresponding system for 4000 years with a timestep equal to  $P_1/50$ . Over the course of a given simulation we generate 1000 equally spaced outputs for each resonant angle, and classify a resonant angle to be librating if the difference between the maximum and minimum is less than a threshold value  $\kappa$ . We set  $\kappa = 7\pi/4$  since this allows for large resonant libration amplitudes while also ensuring that misclassification of librating/non-librating systems is low. Our results are insensitive to nearby values of  $\kappa$  (e.g.  $5\pi/3$ ,  $9\pi/5$ , etc.). We check for librations around both 0 and  $\pi$ .

Our results are presented in Table 6.2 for our PPI and noPPI models, for 300 samples randomly drawn from each posterior distribution. The error bars are calculated



		PPI	noPPI
		model	model
$\phi_1$	librat-	$98\% \pm 6\%$	$1\% \pm 6\%$
	ing		
$\phi_2$	librat-	$5\% \pm 6\%$	$1\% \pm 6\%$
	ing		

Table 6.2: The percent of randomly drawn samples with  $\phi_1$  and  $\phi_2$  librating, for our PPI and noPPI models. Error bars calculated from simple Poisson statistics.

from simple poisson statistics. For our PPI model, almost every drawn sample has  $\phi_1$  librating, strongly suggesting that the system is in MMR. In contrast, our noPPI model shows no evidence of librating resonant angles.

Given our analysis, there is a high likelihood that the HD155358 system is in MMR, and is therefore likely to have formed via planet migration, as we show in the next section.

## 6.4 Formation

### 6.4.1 Methods

We now use the results found in the previous section to explore the formation of HD155358. We use a simple model by which the outer planet is migrated into 2:1 MMR using a parametric model, mimicking the presence of a protoplanetary disk. Specifically, we introduce semi-major axis and eccentricity damping rates,  $\tau_a = a/\dot{a}$  and  $\tau_e = e/\dot{e}$ , respectively, where the two are related by a constant  $K = \tau_a/\tau_e$ . We refer to this class of convergent-migration models as “CM models”.

We follow the implementation by Papaloizou & Larwood (2000) and add an

additional acceleration on each planet according to:

$$\mathbf{a}_{\text{mig}} = -\frac{\mathbf{v}}{\tau_a}$$

$$\mathbf{a}_{\text{damp}} = -2\frac{(\mathbf{v} \cdot \mathbf{r})\mathbf{r}}{r^2\tau_e},$$

where  $\mathbf{v}$  is the velocity and  $\mathbf{r}$  is the position of the planet relative to the star. The migration prescriptions of Papaloizou & Larwood (2000) were designed with Type-I migration in mind, yet our planets likely lie in the Type-II migration regime. However, since we are interested primarily in seeing whether a simple migration model can reproduce the data, this model choice will suffice. More accurate, 3-D hydrodynamical simulations of Type-II planetary migration are significantly more complex and beyond the scope of this paper.

For each simulation three parameters are independently varied – the eccentricity damping rate of the inner planet  $\tau_{e1}$ , the eccentricity damping rate of the outer planet,  $\tau_{e2}$ , and the migration rate of the outer planet,  $\tau_{a2}$ . The inner planet does not undergo migration by itself, i.e.  $\tau_{a1} = 0$ . Initial values for  $\tau_{a2}$  are drawn from a uniform distribution in log-space between  $10^{2.5}$  and  $10^7$  years, while initial values for  $K_1$  and  $K_2$  are drawn between  $10^{-1}$  and  $10^3$ . Planet masses are drawn from our posterior distribution (Section 6.3.2), all eccentricity and inclination values are initialized to zero, and the remaining orbital parameters are randomly drawn from uniform distributions.

When planets migrate into MMR in the presence of a protoplanetary disk an equilibrium eccentricity  $e_{eq}$  is reached, representing a stable balance between migration excitation and protoplanetary disk damping (e.g. Goldreich & Schlichting 2014). For each simulation we migrate the outer planet inwards for a time of  $T_{\text{mig}} = 5\tau_a$  years, after which  $e_{eq}$  has reached a stable value. In cases where  $T_{\text{mig}} < 5000$  years we extend the simulation time to  $T_{\text{mig}} = 5000$  to ensure a stable solution. The migration parameters  $\tau_{a1}$ ,  $\tau_{e1}$  and  $\tau_{e2}$  are then logarithmically increased to  $10^7$  years over the same amount of time ( $T_{\text{mig}}$ ), mimicking the dispersal of the protoplanetary disk. Simulations are independently checked to ensure that a) an equilibrium eccentricity is

reached over  $T_{\text{mig}}$ , and b) the disk dispersal is done adiabatically, ensuring that the resonance is not abruptly changed during the increase of  $\tau_{a_1}$ ,  $\tau_{e_1}$  and  $\tau_{e_2}$ . Simulations that do not fulfill this criteria are discarded.

Once migration is turned off, a RV curve is generated from the simulation and fit to the original RV data using EMCEE as before, but now with only five free parameters:  $t_s$ , a parameter allowing the rescaling of the orbital periods,  $t_t$ , a parameter accounting for an offset in time,  $y_s$ , a RV-stretch parameter to account for amplitude offsets (effectively rescaling the masses of both the planets and the star, while keeping the mass ratios and periods constant). As in the original analysis, we also include  $\gamma$ , an offset parameter to account for any stellar drift along the line of sight, and  $J$ , a jitter parameter to account for underestimated measurement noise and intrinsic stellar noise in the RV data. Each EMCEE fit is run for an initial burnin phase of 200 steps with 100 walkers, after which the walkers are resampled near the best solution and run for 2000 steps.

### 6.4.2 Model Comparison

In a Bayesian sense, each simulation represents a different model  $M$  characterized by  $\theta_{\text{model}} = \{\tau_{a_1}, K_1, K_2\}$ , with each model having a unique MAP estimate for its parameters  $\theta_{\text{fit}} = \{t_s, t_t, y_s, \gamma, J\}$ . Note that our analysis thus incorporates the fact that many different models might explain the data equally well. A single model with parameters  $\theta = \{\tau_{a_1}, K_1, K_2, t_s, t_t, y_s, \gamma, J\}$  on the other hand would make MCMC convergence more difficult.

When multiple models can explain the data, the posterior odds ratio can be used to determine if there is any preference for one model over another. The posterior odds ratio,  $P_{ij}$ , is calculated according to (Gregory 2005):

$$P_{ij} = \frac{p(M_i) p(D|M_i)}{p(M_j) p(D|M_j)}, \quad (6.1)$$

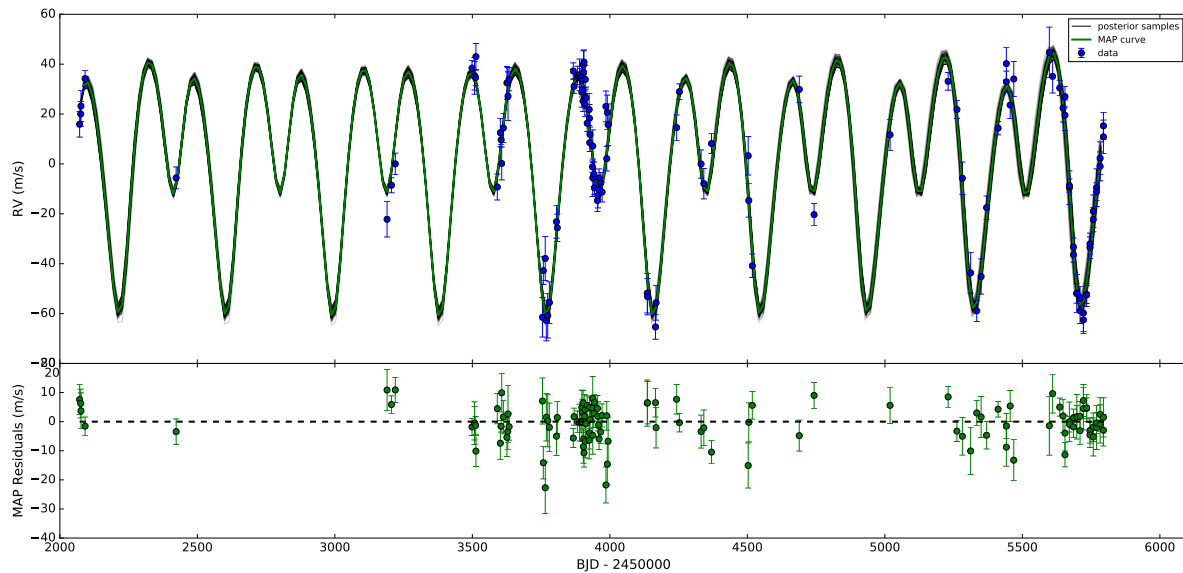


Figure 6.2: RV data and  $\theta_{\text{mig,best}}$  fit. Top panel shows the RV data points, MCMC MAP value (green), and 100 randomly plotted samples from the posterior (black). Bottom panel shows the residuals for the MAP fit to the RV data.

where  $p(M)$  is the prior odds for model  $M$ , and  $p(D|M)$  is the marginal (or global) likelihood for model  $M$ . The ratio of marginal likelihoods for two competing models is also known as Bayes' factor. In our case, the ratio of prior odds is unity since we have no prior model preference. Thus, the posterior odds ratio is equivalent to calculating Bayes' factor.

Formally, the marginal likelihood is calculated by marginalizing over the parameters  $\theta$  of a model according to (Gregory 2005):

$$p(D|M) = \int p(\theta|M)p(D|\theta, M)d\theta = \mathcal{L}(M) \quad (6.2)$$

where  $p(D|\theta, M)$  is the likelihood and  $p(\theta|M)$  is the prior. The marginal likelihood represents the probability of the data given the model.

When the marginal likelihood is normally distributed with flat priors, Eq. 6.2 can

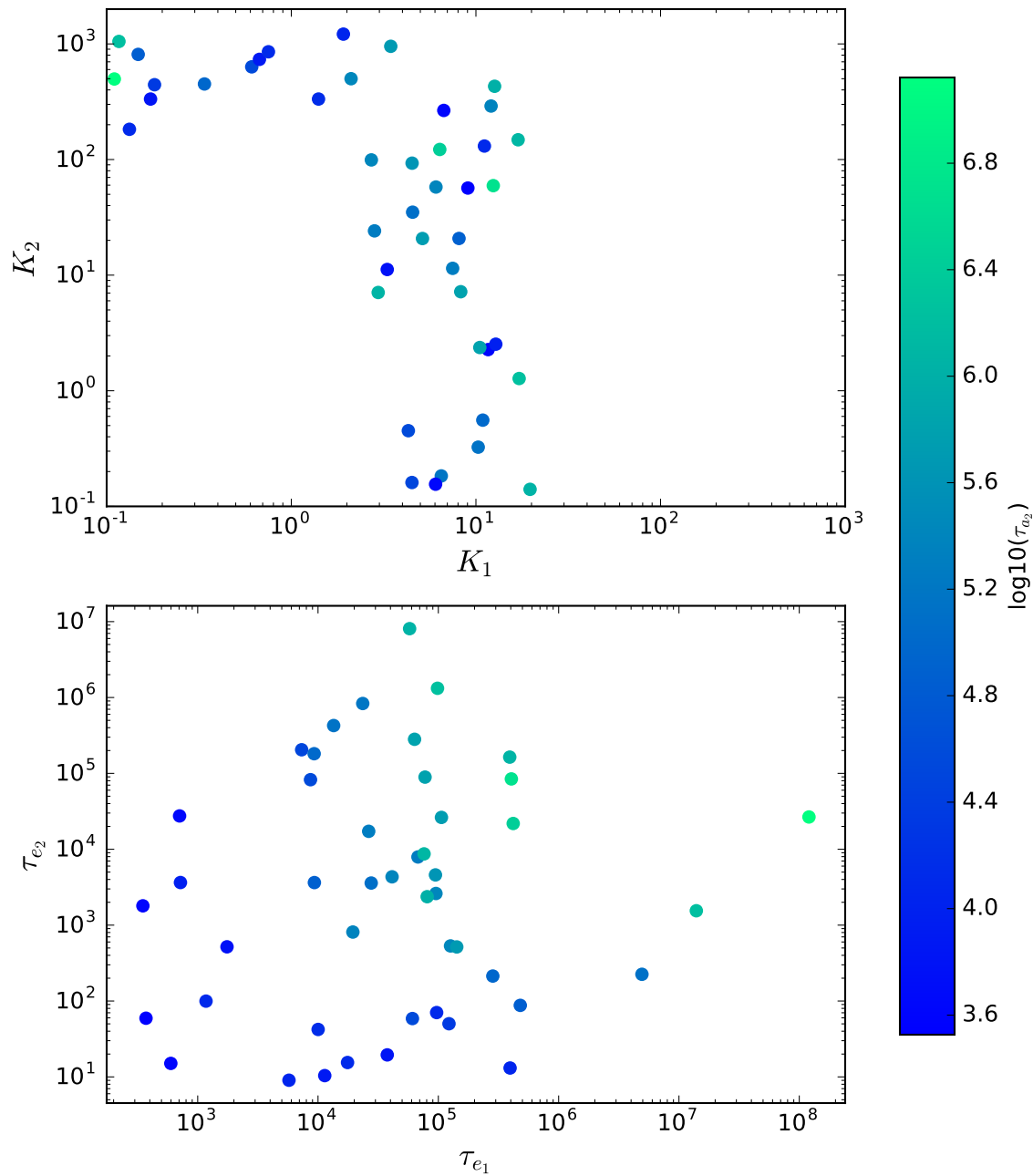


Figure 6.3: The best 45 models  $\theta_{\text{model}} = \{\tau_{a1}, K_1, K_2\}$  with Bayes' factors less than 100 when compared against the best model in our sample of 3000 simulations. Top panel presents the data in  $(K_1, K_2)$  space, and the parameters from our 3000 simulations were uniformly sampled from the region displayed. Bottom panel displays the same data in  $(\tau_{e1}, \tau_{e2})$  space. Colour indicates the log value of  $\tau_{a1}$ .

be approximated as (Kass & Raftery 1995; Gregory 2005):

$$\mathcal{L}(M) \approx \mathcal{L}(\hat{\theta})(2\pi)^{d/2}|\Sigma|^{1/2}\Delta\theta \quad (6.3)$$

where  $\mathcal{L}(\hat{\theta})$  is the the maximum likelihood,  $d$  is the number of parameters in model  $M$ ,  $\Sigma$  is the covariance matrix of the posterior distribution, and  $\Delta\theta = \prod_i^d 1/\delta\theta_i$  is the product of prior probabilities normalized by their lengths  $\delta\theta$ . Since all models have the same flat priors for each parameter, Eq. 6.1 becomes:

$$P_{ij} = \frac{\mathcal{L}_i(\hat{\theta})|\Sigma_i|^{1/2}}{\mathcal{L}_j(\hat{\theta})|\Sigma_j|^{1/2}} \quad (6.4)$$

Since EMCEE returns both the samples and log-likelihoods at each step in the MCMC chain, it is straightforward to calculate the posterior odds ratio using Eq. 6.4.

### 6.4.3 Results

Our best model from a sample of 3000 simulations is plotted in Figure 6.2, corresponding to  $\theta_{\text{model,best}} = (\tau_{a_2}, K_1, K_2) = (4000 \text{ years}, 7, 265)$ . In the top panel we plot the MAP estimate along with 100 randomly drawn samples from our posterior distribution. In the lower panel the residuals between our MAP estimate and the RV data are shown. As can be seen, our model represents a good fit to the data.

Following Kass & Raftery (1995), a posterior odds ratio lower than 100 indicates no decisive preference for one model over another, and in Figure 6.3 we plot competing models which, when compared to  $\theta_{\text{model,best}}$ , yield a posterior odds ratio of less than 100. The top panel in Figure 6.3 presents the valid models in  $(K_1, K_2, \tau_{a_2})$  space, while the bottom panel presents them in  $(\tau_{e_1}, \tau_{e_2}, \tau_{a_2})$  space. Although many different migration models are able to explain the data, regions of parameter space appear to be ruled out. In the top panel of Figure 6.3,  $(K_1 < 3, K_2 < 100)$  and  $K_1 > 20$  are two regions that appear to be ruled out by the data. In the bottom panel, positive correlation can be seen between  $\tau_{a_2}$  and  $\tau_{e_1} + \tau_{e_2}$ .

## 6.5 Stability

Following Marshall et al. (2010) and Horner et al. (2011), R2012 conducted a stability analysis by holding the inner planet constant at the best-fit values and varying the outer planet's orbital parameters randomly over a  $3\sigma$  range in  $a$ ,  $e$ ,  $\omega$  and  $M$ . However, drawing parameters in this manner does not preserve their correlations, and it is possible to draw parameter combinations that are inconsistent with the RV data. R2012 also kept the planet masses fixed at their minimum  $m \sin(i)$  values, precluding the possibility of further constraining the masses from the stability analysis.

In a Bayesian framework, we can simply draw parameters from the posterior distribution and simulate them for a desired length of time. Parameter correlations are naturally preserved in the posterior distribution, and a probability of longterm stability can be easily found.

In this study we draw 2000 random samples from our PPI model's posterior distribution and simulate the subsequent evolution for  $10^9$  years using WHFAST with a timestep of  $P_1/200$ . We also make use of the Simulation Archive (Rein & Tamayo 2017) for stopping, restarting and analyzing simulations. The relative energy error for all stable simulations remains bounded at  $< 10^{-7}$ .

The results are presented in Figure 6.4 as a histogram for each parameter. Stable and unstable systems over  $10^9$  years are marked in green and red, respectively, while our MAP values from our PPI model is shown as vertical, black, dashed lines.  $83\% \pm 2\%$  of our samples are stable over  $10^9$  years and our MAP values land in highly stable regions, indicating that our PPI model is longterm stable.

Unstable systems appear to be clustered in certain regions of parameter space. As can be seen in Figure 6.4,  $m_1 \sin(i) < 0.87$ ,  $e_2 > 0.15$ ,  $a_2 < 1.01$  AU and  $\omega_2 < 4$  are regions where there are a significant fraction of unstable systems. It is therefore unlikely that the true planet parameters lie in these regions.

These unstable regions are consistent with the results found in R2012, however,

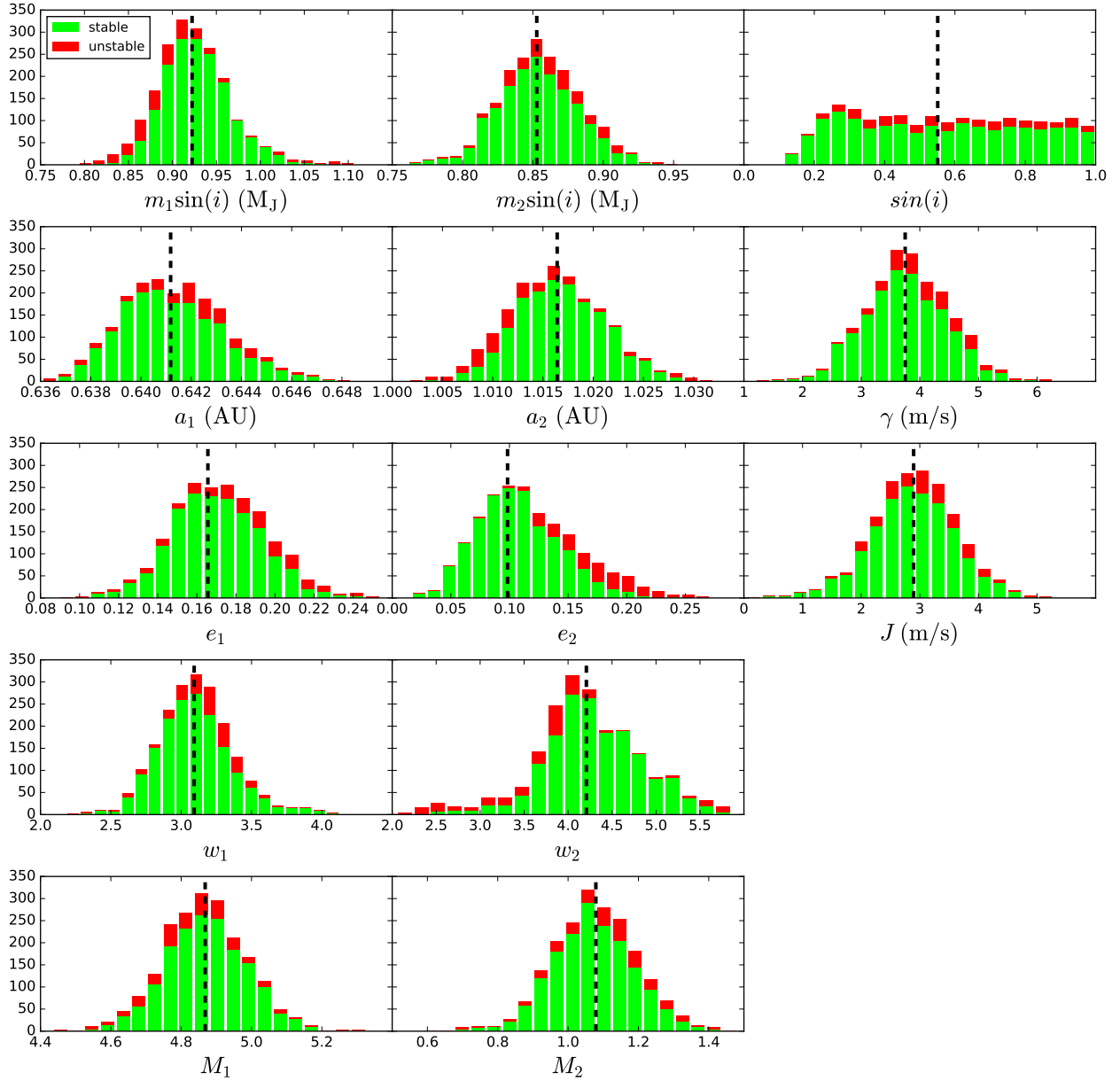


Figure 6.4: Histograms of each parameter showing the distribution of 2000 stable (green) and unstable (red) systems drawn from our PPI model’s posterior distribution and simulated for  $10^9$  years. The black vertical dashed line in each histogram represents our MAP estimate for that parameter.



unlike R2012 our best-fit values are centred in highly stable regions (see Figures 9 and 10 in R2012 for a comparison). Although not shown, we find no clustering of unstable systems in  $(m_1, m_2)$  space, and thus the planet masses cannot be further constrained via stability analysis.

## 6.6 Discussion and Conclusion

In this work we used three different model types to analyze the RV curve of HD155358 – the PPI, noPPI and CM models. Our PPI (planet-planet interactions) and noPPI (no planet-planet interactions) models fit the RV curve to a model parameterized by the orbital elements of each planet (Section 6.3), while our CM model was parameterized by formation parameters and fit the result of planet migration to the RV curve (Section 6.4). The best-fit parameters from our PPI and noPPI models are shown in Table 6.1, while Table 6.2 shows that there is a high likelihood that the planets of HD155358 are in MMR.

The noPPI model is an approximation to the PPI model, and we have shown in Section 6.3.2 that planet-planet interactions are strong enough in the HD155358 system to make this approximation inaccurate. More specifically, the orbital parameters returned by our PPI and noPPI models differ by up to  $2\sigma$ .

Our CM model has demonstrated that formation models of this style can be used to fit RV curves and constrain the initial conditions of a given system. One possibility for future work is to make the CM model more sophisticated, for example by modelling the planet-disk interactions in more realistic hydrodynamic simulations (Rein et al. 2010). With such a model, one could place even more constraints on the formation of HD155358.

From a frequentist’s point of view, the reduced  $\chi^2$  values for our PPI, noPPI and best CM model are 1.4, 1.6 and 0.7 respectively, indicating that all three models are capable of fitting the data well. However, our PPI model should be considered the

only valid model when it comes to determining the true values of the observed system. We also performed a stability analysis on our PPI model, finding that  $83\% \pm 2\%$  of samples drawn from our posterior are stable over  $10^9$  years. We find regions of stable and unstable parameter space similar to R2012, however unlike R2012 our best-fit model solution is centred in a stable region.

## 6.7 Summary

My Summary.

# **Chapter 7**

## **Conclusions & Future Work**

### **7.1 Conclusions**

My Conclusions

### **7.2 Future Work and Directions**

My Future Work and Directions.

# Bibliography

Akeson, R. L., Chen, X., Ciardi, D., & Crane, M. 2013, *PASP*, 125, 10

ALMA Partnership et al. 2015, *ApJ*, 808, L3

André, Q., & Papaloizou, J. C. B. 2016, *MNRAS*, 461, 4406

Armitage, P. J. 2007, *ArXiv Astrophysics e-prints*

—. 2010, *Astrophysics of Planet Formation*, 294

Barnes, R., & Greenberg, R. 2006, *ApJ*, 647, L163

Barnes, R., Raymond, S. N., Jackson, B., & Greenberg, R. 2008, *Astrobiology*, 8, 557

Baruteau, C., et al. 2013, *ArXiv e-prints*

Bastien, F. A., Stassun, K. G., & Pepper, J. 2014, *ArXiv e-prints*

Batalha, N. M., et al. 2013, *ApJS*, 204, 24

Batygin, K., Bodenheimer, P. H., & Laughlin, G. P. 2016, *ApJ*, 829, 114

Batygin, K., & Morbidelli, A. 2013, *AJ*, 145, 10

Batygin, K., Morbidelli, A., & Holman, M. J. 2015, *ApJ*, 799, 120

Batygin, K., Stevenson, D. J., & Bodenheimer, P. H. 2011, *ApJ*, 738, 1

- Beaugé, C., Ferraz-Mello, S., & Michtchenko, T. A. 2007, *Planetary Masses and Orbital Parameters from Radial Velocity Measurements*, 1
- Benz, W., Ida, S., Alibert, Y., Lin, D. N. C., & Mordasini, C. 2014, *ArXiv e-prints*
- Blum, J., & Wurm, G. 2008, *ARA&A*, 46, 21
- Boley, A. C., Granados Contreras, A. P., & Gladman, B. 2016, *ApJ*, 817, L17
- Boley, A. C., Morris, M. A., & Ford, E. B. 2014, *ApJ*, 792, L27
- Bonfils, X., et al. 2013, *A&A*, 549, A109
- Borucki, W. J., et al. 2010, *Science*, 327, 977
- Brown, T. M., Latham, D. W., Everett, M. E., & Esquerdo, G. A. 2011, *AJ*, 142, 112
- Catanzarite, C., & Shao, M. 2011, *ApJ*
- Chambers, J. E. 1999, *MNRAS*, 304, 793
- Chambers, J. E., Wetherill, G. W., & Boss, A. P. 1996, *Icarus*, 119, 261
- Charbonneau, D., Brown, T. M., Latham, D. W., & Mayor, M. 2000, *ApJ*, 529, L45
- Chatterjee, S., & Ford, E. B. 2015, *ApJ*, 803, 33
- Chatterjee, S., Ford, E. B., Matsumura, S., & Rasio, F. A. 2008, *ApJ*, 686, 580
- Chen, T., & Guestrin, C. 2016, *arXiv preprint arXiv:1603.02754*
- Chiang, E., & Laughlin, G. 2013, *MNRAS*, 431, 3444
- Chirikov, B. 1979, *Physics Review*, 52, 263
- Choquet, É., et al. 2016, *ApJ*, 817, L2
- Christiansen, J. L., et al. 2012, *ApJ*, 124

- Cochran, W. D., Endl, M., Wittenmyer, R. A., & Bean, J. L. 2007, *ApJ*, 665, 1407
- Collister, A. A., & Lahav, O. 2004, *Publications of the Astronomical Society of the Pacific*, 116, 345
- Colón, K. D., Ford, E. B., & Morehead, R. C. 2012, *MNRAS*, 426, 342
- de Bruijne, J. H. J. 2012, *Ap&SS*, 341, 31
- Deck, K. M., & Agol, E. 2015, *The Astrophysical Journal*, 802, 116
- Deck, K. M., Holman, M. J., Agol, E., Carter, J. A., Lissauer, J. J., Ragozzine, D., & Winn, J. N. 2012, *The Astrophysical Journal Letters*, 755, L21
- Delisle, J.-B., Laskar, J., & Correia, A. C. M. 2014, *AA*, 566, 14
- Demircan, O., & Kahraman, G. 1991, *ApSS*, 181, 9
- Dong, S., & Zhu, Z. 2013, *ApJ*, 778, 53
- Dressing, C. D., & Charbonneau, D. 2013, *ApJ*, 767, 95
- Duncan, M., Quinn, T., & Tremaine, S. 1989, *Icarus*, 82, 402
- Duncan, M. J., Levison, H. F., & Lee, M. H. 1998, *AJ*, 116, 2067
- Everett, M. E., Howell, S. B., Silva, D. R., & Szkody, P. 2013, *ApJ*, 771, 107
- Faber, P., & Quillen, A. C. 2007, *Monthly Notices of the Royal Astronomical Society*, 382, 1823
- Fabrycky, D. C., Lissauer, J. J., Ragozzine, D., Rowe, J. F., & Steffen, J. H. 2014, *ApJ*, 790, 12
- Fang, J., & Margot, J.-L. 2013, *ApJ*, 767, 115
- Fernandez, J. A., & Ip, W.-H. 1984, *Icarus*, 58, 109

- Ford, E. B., et al. 2012, *The Astrophysical Journal*, 750, 113
- Foreman-Mackey, D., Hogg, D. W., Lang, D., & Goodman, J. 2013, *PASP*, 125, 306
- Fressin, F., et al. 2013, *ApJ*, 766, 81
- Friedman, J., Hastie, T., & Tibshirani, R. 2001, *The elements of statistical learning*, Vol. 1 (Springer series in statistics Springer, Berlin)
- Fuhrmann, K., & Bernkopf, J. 2008, *MNRAS*, 384, 1563
- Fung, J., & Chiang, E. 2017, *ArXiv e-prints*
- Gaidos, E. 2013, *ApJ*, 770, 90
- Gaidos, E., & Mann, A. W. 2013, *ApJ*, 762, 41
- Gelman, A., & Rubin, D. 1992, *Statistical Science*, 7, 457, <http://www.stat.columbia.edu/~gelman/research/published/itsim.pdf>
- Gladman, B. 1993, *Icarus*, 106, 247
- Goldreich, P., & Schlichting, H. E. 2014, *AJ*, 147, 32
- Goldreich, P., & Soter, S. 1966, *Icarus*, 5, 14
- Goldreich, P., & Tremaine, S. 1979, *ApJ*, 233, 857
- . 1980, *ApJ*, 241, 425
- Goldreich, P., & Ward, W. R. 1973, *ApJ*, 183, 1051
- Gomes, R. S., Morbidelli, A., & Levison, H. F. 2004, *Icarus*, 170, 492
- Greenberg, R., Hartmann, W. K., Chapman, C. R., & Wacker, J. F. 1978, *Icarus*, 35, 1
- Gregory, P. C. 2005, *Bayesian Logical Data Analysis for the Physical Sciences: A Comparative Approach with 'Mathematica' Support* (Cambridge University Press)

- Hadden, S., & Lithwick, Y. 2014, *ApJ*, 787, 7
- Hansen, B. M. S., & Murray, N. 2013, *ApJ*, 775, 53
- Hayashi, C. 1981, *Progress of Theoretical Physics Supplement*, 70, 35
- Henry, G. W., Marcy, G., Butler, R. P., & Vogt, S. S. 1999, *IAU Circ.*, 7307
- Hernandez, D. M., & Dehnen, W. 2016, *ArXiv e-prints*
- Hill, G. J., et al. 2010, in *Society of Photo-Optical Instrumentation Engineers (SPIE) Conference Series*, Vol. 7735, *Society of Photo-Optical Instrumentation Engineers (SPIE) Conference Series*
- Horner, J., Marshall, J. P., Wittenmyer, R. A., & Tinney, C. G. 2011, *MNRAS*, 416, L11
- Howard, A. W., et al. 2012, *ApJS*, 201, 15
- Huang, C., Wu, Y., & Triaud, A. H. M. J. 2016, *ApJ*, 825, 98
- Huber, D., et al. 2014, *ApJS*, 211, 2
- Ida, S., Bryden, G., Lin, D. N. C., & Tanaka, H. 2000, *ApJ*, 534, 428
- Ito, T., & Tanikawa, K. 1999, *Icarus*, 139, 336
- Jackson, B., Barnes, R., & Greenberg, R. 2008, *MNRAS*, 391, 237
- Jefferys, W. H., Fitzpatrick, M. J., & McArthur, B. E. 1988, *Celestial Mechanics*, 41, 39
- Jontof-Hutter, D., Lissauer, J. J., Rowe, J. F., & Fabrycky, D. C. 2014, *ApJ*, 785, 15
- Kass, R. E., & Raftery, A. E. 1995, *Journal of the American Statistical Association*, 90, 773
- Kasting, J. F., Whitmire, D. P., & Reynolds, R. T. 1993, *Icarus*, 101, 108



- Kirsh, D. R., Duncan, M., Brassier, R., & Levison, H. F. 2009, *Icarus*, 199, 197
- Koch, D. G., Borucki, W. J., Basri, G., Batalha, N. M. and Brown, T. M., Caldwell, D., Christensen-Dalsgaard, J., & Cochran, W. D. and DeVore, E. 2010, *ApJ*, 713
- Kokubo, E., & Ida, S. 1998, *Icarus*, 131, 171
- Kopparapu, R. K. 2013, *ApJ*, 767, L8
- Kopparapu, R. k., Ramirez, R. M., SchottelKotte, J., Kasting, J. F., Domagal-Goldman, S., & Eymet, V. 2014, *ArXiv e-prints*
- Kopparapu, R. K., et al. 2013, *ApJ*, 765, 131
- Kreidberg, L., et al. 2014, *Nature*, 505, 69
- Laskar, J. 1994, *A&A*, 287, L9
- Laskar, J., & Gastineau, M. 2009, *Nature*, 459, 817
- Laskar, J., & Robutel, P. 1995, *Celestial Mechanics and Dynamical Astronomy*, 62, 193
- Lecar, M., Franklin, F. A., Holman, M. J., & Murray, N. J. 2001, *ARA&A*, 39, 581
- Lee, H., Fabrycky, D., & Lin, D. N. C. 2013, *ApJ*, 774, 8
- Lee, M. H., & Peale, S. J. 2002, *ApJ*, 567, 596
- Lin, D. N. C., Bodenheimer, P., & Richardson, D. C. 1996, *Nature*, 380, 606
- Lin, D. N. C., & Papaloizou, J. 1986, *ApJ*, 309, 846
- Lissauer, J. J., Ragozzine, D., Fabrycky, D. C., Steffen, J. H., & Ford, E. B. 2011, *ApJ*, 197, 26
- Lithwick, Y., & Wu, Y. 2011, *ApJ*, 739, 31

—. 2012, *ApJ*, 756, 5

Liu, C., Bailer-Jones, C. A. L., Sordo, R., Vallenari, A., Borrachero, R., Luri, X., & Sartoretti, P. 2012, *ApJ*, 426

Lopez, E. D., Fortney, J. J., & Miller, N. 2012, *ApJ*, 761, 59

Malhotra, R. 1993, *Nature*, 365, 819

—. 1995, *AJ*, 110, 420

Mann, A. W., Gaidos, E., & Ansdell, M. 2013, *ApJ*, 779, 188

Mann, A. W., Gaidos, E., Lépine, S., & Hilton, E. J. 2012, *ApJ*, 753, 90

Marchal, C., & Bozis, G. 1982, *Celestial Mechanics*, 26, 311

Marcus, R. A., Stewart, S. T., Sasselov, D., & Hernquist, L. 2009, *ApJ*, 700, L118

Marshall, J., Horner, J., & Carter, A. 2010, *International Journal of Astrobiology*, 9, 259

Marzari, F. 2014, *MNRAS*, 442, 1110

Marzari, F., & Weidenschilling, S. J. 2002, *Icarus*, 156, 570

Mayor, M., & Queloz, D. 1995, *Nature*, 378, 355

Meschiari, S., Wolf, A. S., Rivera, E., Laughlin, G., Vogt, S., & Butler, P. 2009, *PASP*, 121, 1016

Milani, A., & Nobili, A. M. 1983, *Celestial Mechanics*, 31, 213

Moore, A., Hasan, I., & Quillen, A. C. 2013, *MNRAS*, 432, 7

Moorhead, A. V., et al. 2011, *ApJS*, 197, 1

Morton, T. D., & Johnson, J. A. 2011, *ApJ*, 738, 170

Murray, C. D., & Dermott, S. F. 1999, Solar system dynamics

NASA Exoplanet Archive. 2017, Nasa Exoplanet Archive

Owen, J. E., & Wu, Y. 2013, *ApJ*, 775, 105

Pál, A. 2009, *MNRAS*, 396, 1737

Papaloizou, J. C. B., & Larwood, J. D. 2000, *MNRAS*, 315, 823

Peterson, P. 2009, *Int. J. of Computational Science and Engineering*, 4, 296

Petigura, E. A., Howard, A. W., & Marcy, G. W. 2013, *Proceedings of the National Academy of Science*, 110, 19273

Petrovich, C. 2015, *The Astrophysical Journal*, 808, 120

Pierrehumbert, R., & Gaidos, E. 2011, *ApJ*, 734, L13

Pinsonneault, M. H., An, D., Molenda-Żakowicz, J., Chaplin, W. J., Metcalfe, T. S., & Bruntt, H. 2012, *ApJS*, 199, 30

Plummer, H. C. K. 1918, *An introductory treatise on dynamical astronomy*

Pollack, J. B., Hubickyj, O., Bodenheimer, P., Lissauer, J. J., Podolak, M., & Greenzweig, Y. 1996, *Icarus*, 124, 62

Press, W., Flannery, B., Teukolsky, S., & Vetterling, W. 1988, *Numerical Recipes in C* (Cambridge University Press)

Press, W. H., Teukolsky, S. A., Vetterling, W. T., & Flannery, B. P. 2002, *Numerical recipes in C++ : the art of scientific computing*

Pu, B., & Wu, Y. 2015, *ApJ*, 807, 44

Rafikov, R. R. 2003, *AJ*, 125, 942

—. 2006, *ApJ*, 648, 666

Ramirez, S., Akeson, R. L., Ciardi, D. R., Chen, X., Christiansen, J., & Plavchan, P. 2014, *Å*

Raymond, S. N., & Cossou, C. 2014, *MNRAS*

Rein, H. 2012, *MNRAS*, 427, 5

Rein, H., & Liu, S.-F. 2012, *A&A*, 537, 10

Rein, H., & Papaloizou, J. C. B. 2009, *A&A*, 497, 595

Rein, H., Papaloizou, J. C. B., & Kley, W. 2010, *A&A*, 510, A4

Rein, H., & Spiegel, D. S. 2015, *MNRAS*, 446, 1424

Rein, H., & Tamayo, D. 2015, *MNRAS*, 452, 376

—. 2017, *MNRAS*

Robertson, P., et al. 2012, *ApJ*, 749, 39

Rowe, J. F., Bryson, S. T., Marcy, G. W., Lissauer, J. J., & Jontof-Hutter, D. 2014, *ApJ*, 784, 20

Saha, P., & Tremaine, S. 1992, *AJ*, 104, 1633

—. 1994, *AA*, 108, 1962

Santerne, A., Fressin, F., Díaz, R. F., Figueira, P., Almenara, J.-M., & Santos, N. C. 2013, *A&A*, 557, A139

Santerne, A., et al. 2012, *A&A*, 545, A76

Sasselov, D. D., & Lecar, M. 2000, *ApJ*, 528, 995

Schlichting, H. E. 2014, *ApJ*, 795, L15

Schneider, G., et al. 2014, *AJ*, 148, 59

Smith, A. W., & Lissauer, J. J. 2009, *Icarus*, 201, 381

Smith, A. W., & Lissauer, J. J. 2009, *Icarus*, 201, 381

Steffen, J. H., & Hwang, J. A. 2015, *MNRAS*, 448, 16

Steffen, J. H., et al. 2013, *MNRAS*, 428, 1077

Stevenson, K. B., Bean, J. L., Seifahrt, A., Gilbert, G. J., Line, M. R., Désert, J.-M., & Fortney, J. J. 2016, *ApJ*, 817, 141

Sussman, G. J., & Wisdom, J. 1988, *Science*, 241, 433

Tamayo, D. 2014, *MNRAS*, 438, 3577

Tamayo, D., Triaud, A. H. M. J., Menou, K., & Rein, H. 2015, *ApJ*, 805, 100

Tanaka, H., Takeuchi, T., & Ward, W. R. 2002, *ApJ*, 565, 1257

Tian, F., Toon, O. B., Pavlov, A. A., & De Sterck, H. 2005, *ApJ*, 621, 1049

Traub, W. A. 2012, *ApJ*, 745, 20

Tsiaras, A., et al. 2016, *ApJ*, 820, 99

Veras, D., & Mustill, A. J. 2013, *Monthly Notices of the Royal Astronomical Society: Letters*, slt067

Verner, G. A., et al. 2011, *ApJ*, 738, L28

Ward, W. R. 1997, *Icarus*, 126, 261

Weidenschilling, S. J. 1977a, *MNRAS*, 180, 57

—. 1977b, *Ap&SS*, 51, 153

Weiss, L. M., & Marcy, G. W. 2014, *ApJL*, 783, 7

Wetherill, G. W., & Stewart, G. R. 1989, *Icarus*, 77, 330

Winn, J. N. 2010, ArXiv e-prints

Wisdom, J. 1980, *AJ*, 85, 1122

—. 2006, *AJ*, 131, 2294

Wisdom, J., & Holman, M. 1991, *AJ*, 102, 1528

Wu, Y., & Lithwick, Y. 2013, *ApJ*, 772, 74

Wu, Y., & Murray, N. 2003, *ApJ*, 589, 605

Yoshida, H. 1990, *Science Direct*, 150, 6

—. 1993, *AA*, 56, 16

Youdin, A. N. 2011, *ApJ*, 742, 38